The Astrophysical Journal, 671:1591–1623, 2007 December 20

THE HAUNTED HALOS OF ANDROMEDA AND TRIANGULUM: A PANORAMA OF GALAXY FORMATION IN ACTION[1]

R. Ibata,[2] N. F. Martin,[3] M. Irwin,[4] S. Chapman,[4] A. M. N. Ferguson,[5]
G. F. Lewis,[6] and A. W. McConnachie[7]

Received 2007 April 10; accepted 2007 July 18

ABSTRACT

We present a deep photometric survey of the Andromeda galaxy, conducted with the wide-field cameras of CFHT and INT, that covers the inner 50 kpc of the galaxy and the southern quadrant out to ∼150 kpc and includes an extension to M33 at >200 kpc. This is the first systematic panoramic study of this very outermost region of galaxies. We detect a multitude of large-scale structures of low surface brightness, including several streams, and two new relatively luminous ($M_V \sim -9$) dwarf galaxies: And XV and And XVI. Significant variations in stellar populations due to intervening stream–like structures are detected in the inner halo, which is particularly important in shedding light on the mixed and sometimes conflicting results reported in previous studies. Underlying the many substructures lies a faint, smooth, and extremely extended halo component, reaching out to 150 kpc, whose stellar populations are predominantly metal-poor. We find that the smooth halo component in M31 has a radially decreasing profile that can be fitted with a Hernquist model of immense scale radius ∼55 kpc, almost 4 times larger than theoretical predictions. Alternatively a power law with $\Sigma_V \propto R^{-1.91\pm0.11}$ can be fitted to the projected profile, similar to the density profile in the Milky Way. If it is symmetric, the total luminosity of this structure is $\sim 10^9\, L_\odot$, again similar to the stellar halo of the Milky Way. This vast, smooth, underlying halo is reminiscent of a classical "monolithic" model and completely unexpected from modern galaxy formation models. M33 is also found to have an extended metal-poor halo component, which can be fitted with a Hernquist model also of scale radius ∼55 kpc. These extended slowly decreasing halos will provide a challenge and strong constraints for further modeling.

Subject headings: galaxies: evolution — galaxies: individual (M31, M33) — galaxies: structure — Local Group

Online material: color figures

1. INTRODUCTION

The outskirts of galaxies hold fundamental clues about their formation history. It is into these regions that new material continues to arrive as part of their ongoing assembly, and it was also into these regions that material was deposited during the violent interactions in the galaxy's distant past. Moreover, the long dynamical timescales for structures beyond the disk ensure that the debris of accreted material takes a very long time to be erased by the process of phase mixing, which in turn means that we can hope to detect many of these signatures of formation as coherent spatial structures (Johnston et al. 1996).

Much theoretical effort has been devoted in recent years to understanding the fine-scale structure of galaxies (Abadi et al. 2003, 2006; Bullock & Johnston 2005), as researchers realized that cosmological models could be tested not only with the classical large-scale probes, such as galaxy clusters, filaments, and voids, but also with observations on galactic and subgalactic scales (Freeman & Bland-Hawthorn 2002). Indeed, it is precisely in the latter regions that the best constraints on cosmology are expected to be put (Springel et al. 2006) in the coming decades. The ΛCDM cosmologies, in particular, are now sufficiently well developed theoretically (e.g., Bullock et al. 2001; Bullock & Johnston 2005) that the Local Group provides a means of directly testing and constraining these theories, by observing the profiles of density, age, and metallicity of the structure and substructure predicted to be found in the outer parts of galaxy disks and in galaxy halos.

1.1. *The Andromeda Galaxy*

Andromeda, like the Milky Way, is a canonical galaxy and a laboratory for examining in close detail many of the astrophysical processes that are investigated in the more distant field. Studying Andromeda and Triangulum in the Local Group has the advantage that it affords us a view free from the problems that plague Galactic studies due to our position within the Milky Way, yet their location within the Local Group allows us to resolve and study individual stars and deduce population properties in incomparably greater detail than is possible in distant systems.

Andromeda is the closest giant spiral galaxy to our own and the only other giant galaxy in the Local Group. In many ways Andromeda is the "sister" to the Milky Way, having very similar total masses (including the dark matter; Evans et al. 2000; Ibata et al. 2004), having shared a common origin, and probably sharing the same ultimate fate when they finally merge in the distant future. However, there are significant differences between these "twins." M31 is slightly more luminous than the Milky Way, and it has a higher rotation speed and a bulge with higher velocity dispersion. M31 possesses a globular cluster system with

[1] Based on observations obtained with MegaPrime/MegaCam, a joint project of CFHT and CEA/DAPNIA, at the Canada-France-Hawaii Telescope (CFHT), which is operated by the National Research Council (NRC) of Canada, the Institute National des Sciences de l'Univers of the Centre National de la Recherche Scientifique of France, and the University of Hawaii.

[2] Observatoire Astronomique, Université de Strasbourg, CNRS, 67000 Strasbourg, France.

[3] Max-Planck-Institut für Astronomie, D-69117 Heidelberg, Germany.

[4] Institute of Astronomy, University of Cambridge, Cambridge CB3 0HA, UK.

[5] Institute for Astronomy, University of Edinburgh, Royal Observatory, Blackford Hill, Edinburgh EH9 3HJ, UK.

[6] Institute of Astronomy, School of Physics, A29, University of Sydney, Sydney NSW 2006, Australia.

[7] Department of Physics and Astronomy, University of Victoria, Victoria, BC V8W 3P6, Canada.

$\sim$500 members, approximately 3 times more numerous than that of the Milky Way. The disk of Andromeda is also much more extensive, with a scale length of 5.9 ± 0.3 kpc (R-band value corrected for a distance of 785 kpc; Walterbos & Kennicutt 1988) compared to 2.3 ± 0.1 for the Milky Way (Ruphy et al. 1996), but is currently forming stars at a lower rate than the Galaxy (Avila-Reese et al. 2002; Walterbos & Braun 1994). There are indications that the Milky Way has undergone an exceptionally low amount of merging and has unusually low specific angular momentum, whereas M31 appears to be a much more normal galaxy in these respects (Hammer et al. 2007). Although possibly the consequence of low number statistics, it is tempting to attribute significance to the fact that Andromeda has a compact elliptical (M32) and three dwarf elliptical galaxies (NGC 205, NGC 147, NGC 185) among its entourage of satellites, as well as no star-forming dwarf irregulars (dIrrs) within 200 kpc, whereas the Milky Way has no ellipticals but two dIrrs. However, it is perhaps in their purported halo populations that the differences between the two galaxies are most curious and most interesting.

1.2. *Comparing the Halos of Andromeda and the Milky Way*

A large number of studies of the Milky Way halo (e.g., Ryan & Norris 1991; Chiba & Beers 2000 and references therein) have revealed that this structure is very metal-poor, with a median $\langle[\mathrm{Fe/H}]\rangle = -1.6$. It has a high velocity dispersion, with (U, V, W) values in the solar neighborhood of (141, 106, 94) km s^{-1}, and a small prograde rotation of 30–50 km s^{-1}. There is broad agreement that the stellar halo is flattened with $b/a \sim 0.6$ (e.g., Morrison et al. 2000; Yanny et al. 2000; Chen et al. 2001; Siegel et al. 2002), although there are indications that the distribution becomes spherical beyond 15–20 kpc (Chiba & Beers 2000).

The volume density profile and extent of this structure have been harder to pin down. This is perhaps not surprising given the patchy sky coverage of most studies, since current expectations are that the stellar halo is significantly lumpy (Bullock & Johnston 2005). The stellar volume density is generally modeled as $\rho(r) \propto r^{-\alpha}$, and recent studies (Wetterer & McGraw 1996; Morrison et al. 2000; Yanny et al. 2000; Ivezic et al. 2000; Siegel et al. 2002; Vivas & Zinn 2006) have found values of the exponent ranging from $\alpha = 3.55 \pm 0.13$ (Chiba & Beers 2000) to 2.5 ± 0.3 (Chen et al. 2001), with a general consensus of $\rho(r) \propto r^{-3}$. Note that in external systems, where we observe the projected density, $\rho(r) \propto r^{-3}$ would correspond to $\Sigma(R) \propto R^{-2}$.

Recent wide-field studies have gone a long way in improving our knowledge of the radial extent of the Milky Way halo. Using the Sloan Digital Sky Survey (SDSS) database, Yanny et al. (2000) were able to follow A-colored stars in the halo to $\sim$25 kpc and blue straggler candidates out to $\sim$50 kpc. From the same survey, Ivezic et al. (2000) followed the profile of RR Lyrae candidates and found a sharp drop in the star counts between 50 and 60 kpc, although this discontinuity in density has since been found to be due to the intervening stream of the Sgr dwarf galaxy (Ibata et al. 2001b). From VLT spectroscopy of 34 faint A stars selected from the SDSS, Clewley et al. (2005) were able to show that the stellar halo extends out to at least 100 kpc, although again a subsample of their stars appears to be associated with the stream of carbon stars emanating from the Sgr dwarf (Ibata et al. 2001c). Several other studies have found evidence for further lumpy structures in the halo (e.g., Vivas & Zinn 2006; Martin et al. 2007; Belokurov et al. 2007 and references therein).

It has been believed for many years that M31 possesses a stellar halo that is fundamentally different from that deduced from the above and earlier observations in the Milky Way. The first deep CCD studies by Mould & Kristian (1986) in a field in the inner halo of M31 found a surprisingly high mean metallicity of $\langle[\mathrm{M/H}]\rangle = -0.6$. Furthermore, the surface brightness profile measured along the minor axis from integrated light (Pritchet & van den Bergh 1994) is consistent with a de Vaucouleurs $R^{1/4}$ law out to $R = 20$ kpc, quite unlike the power-law behavior deduced for the halo of the Milky Way. Both the de Vaucouleurs profile and the high metallicity are suggestive of an active merger history at the time of halo (or bulge) formation.

The existence of the metal-rich halo population was confirmed by several subsequent studies, notably among these the wide-field (0.16 deg^2) photometric study by Durrell et al. (2001) in a location 20 kpc out along the minor axis. In addition to the main $\langle[\mathrm{M/H}]\rangle = -0.5$ component, Durrell et al. (2001) also discovered that 30%–40% of the stars at this location belong to a metal-poor population. The surface density of the metal-poor subsample falls off rapidly as $\Sigma(R) \propto R^{-5.25\pm0.63}$, but slower than the $\Sigma(R) \propto R^{-6.54\pm0.59}$ relation for the metal-rich subsample. These results were later complemented by the same authors with a minor-axis field at $R = 30$ kpc (Durrell et al. 2004), which showed essentially identical abundance properties to their 20 kpc field, leading them to conclude that the outer halo shows little or no radial metallicity gradient.

As an alternative to the above "wide-field" approach, Bellazzini et al. (2003) analyzed a set of 16 *Hubble Space Telescope* (*HST*) WFPC2 fields with much deeper photometry, mostly in and around the M31 disk, but with some fields extending out to a distance of 35 kpc. Throughout this area they detect the previously discussed dominant metal-rich component with $[\mathrm{Fe/H}] \sim -0.6$, but also an additional high-metallicity component with $[\mathrm{Fe/H}] \sim -0.2$. Interestingly, they found that the fraction of metal-poor stars is constant from field to field, although metal-rich stars are enhanced in regions containing substructure, especially along the extended path of the giant stream (Ibata et al. 2001a).

The inclusion of kinematic information has been extremely useful but has also added another dimension of complexity to the puzzle. Reitzel & Guhathakurta (2002) analyzed a sample of 29 stars in a field at $R = 19$ kpc on the minor axis and found the mean metallicity to be in the range $\langle[\mathrm{M/H}]\rangle = -1.9$ to -1.1, dependent on calibration and sample selection issues, but significantly lower than the results deduced from the above photometric analyses.

A wider field view was obtained by Chapman et al. (2006), who sampled the halo at 54 locations between 10 and 70 kpc, isolating 827 out of a sample of $\sim 10^4$ stars as having kinematics consistent with being halo members. The population was found to have $\langle[\mathrm{Fe/H}]\rangle \sim -1.4$ with a dispersion of 0.2 dex, indicating that kinematic selection reveals a halo similar to that of the Milky Way underneath the "halo" substructures, which in many cases are metal-rich and in general cannot have halo-like kinematics. The (central) velocity dispersion of 152 km s^{-1} deduced from the sample is also comparable to that of the Milky Way.

In an impressive effort of finding needles in a haystack, Kalirai et al. (2006b) and Gilbert et al. (2006) extended the kinematic coverage out to 165 kpc and claim a detection of the halo at $R > 100$ kpc based on a sample of three stars. To minimize contamination, they implemented a complex nonlinear algorithm to assign likelihoods to the observed stars, and as the algorithm was trained on the inner region of M31, the biases for the outer halo population are not well known.

1.3. *The Triangulum Galaxy*

If Andromeda is the twin of the Milky Way, the Triangulum galaxy (M33), with a mass $\sim$10 times lower than either of these two giants, is their little sister. M33 is the third brightest galaxy in

the Local Group ($M_V = -18.9$) and probably a satellite of M31. The relatively undisturbed optical appearance of M33 places strong constraints on the past interaction of these two galaxies (Loeb et al. 2005), although it should be noted that the gaseous component is extremely warped (Rogstad et al. 1976).

The early CCD study of the halo of M33 by Mould & Kristian (1986) claimed an inner halo component with a more "normal" metallicity ($\langle[M/H]\rangle = -2.2$) than deduced for M31. In reality, however, this field lies within the disk of M33 and does not probe the halo, as shown by Tiede et al. (2004). Further progress in understanding the elusive halo component of this galaxy was only achieved recently. In their kinematic study of star clusters in M33, Chandar et al. (2002) find evidence for two subpopulations, with old clusters showing evidence for a large velocity dispersion, which they interpret as the sign of a halo population. Sarajedini et al. (2006) argued that the double peak in the distribution of periods of RR Lyrae variables in M33 is evidence for the existence of an old halo population. Further signs of this halo component were detected with Keck DEIMOS in the spectroscopic study of McConnachie et al. (2006), who distinguished halo field stars from stars in the disk via their kinematics and deduce a mean metallicity for the halo component of $\langle[Fe/H]\rangle = -1.5$, with a narrower spread of abundance than the disk stars.

1.4. *Halos of More Distant Disk Galaxies*

Due to their extremely faint nature, the halos of spiral galaxies beyond the Local Group have been extremely challenging to observe. A major advance in detecting extraplanar light in distant galaxies was made by stacking 1047 edge-on spiral galaxies observed in the SDSS (Zibetti et al. 2004). The resulting stack showed a flattened ($c/a \sim 0.6$) distribution with a power-law density profile $\rho(r) \propto r^{-3}$, similar to the properties of the halo of the Milky Way deduced from the studies reviewed above. This structure could be detected out to approximately 10 exponential scale lengths of the disk (i.e., equivalent to approximately 25 kpc in the Milky Way). An analogous structure was also detected directly from the surface brightness around a single isolated galaxy in an ultradeep *HST* survey (Zibetti & Ferguson 2004).

Extraplanar populations have also been detected via star counts of resolved red giant branch (RGB) populations in nearby (<10 Mpc) galaxies from deep *HST* imaging. Notable among these is the survey of Mouhcine et al. (2005a, 2005b), who employed WFPC2 to survey eight nearby spirals. Their fields probed the minor-axis halo out to $R = 13$ kpc. Interestingly, they find a correlation between galaxy luminosity and the metallicity of the extraplanar population, with low-luminosity galaxies containing metal-poor stars with a narrow abundance spread, while luminous galaxies contain metal-rich stars and a wide abundance spread. Their results for galaxies of similar luminosity to M31 are in good agreement with the metallicity distribution of minor-axis fields in Andromeda at 10–20 kpc.

However, as we show below, the minor-axis fields in M31, from which most of the information on the halo or "spheroid" is derived, do not directly probe that component. Furthermore, as we have reviewed above, kinematically selected halo stars in M31 display a similar metallicity to genuine halo stars in the Milky Way (Chapman et al. 2006). These considerations suggest that the Mouhcine relation is caused by small structures accreted into the inner regions of the halo, which are largely supported by rotation, rather than random motions. The correlation of the metallicity of the extraplanar stars with galaxy luminosity found by Mouhcine et al. (2005a, 2005b) may then simply reflect that more massive host galaxies are able to accrete larger dwarf galaxies, which themselves have a higher metallicity.

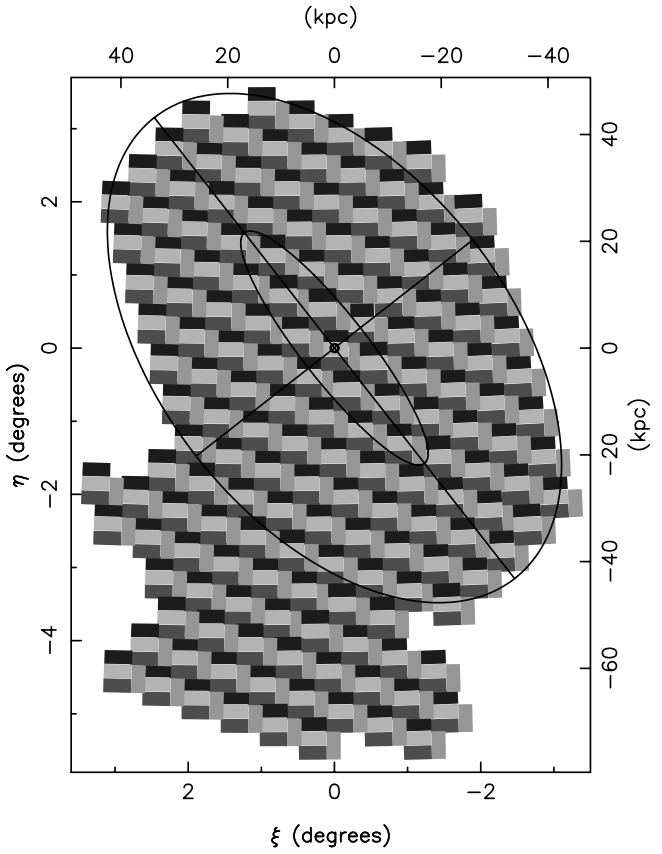

FIG. 1.—Coverage of our large panoramic survey of M31 with the INT camera, in standard coordinates (ξ, η). The inner ellipse represents a disk of inclination 77° and radius 2° (27 kpc), the approximate end of the regular H I disk. The outer ellipse shows a 55 kpc radius ellipse flattened to $c/a = 0.6$, and the major and minor axes are indicated with straight lines out to this ellipse. This map is constructed from a total of 164 INT WFC individual pointings. [*See the electronic edition of the Journal for a color version of this figure.*]

Nevertheless, we stress that all of these observations beyond the Local Group are derived from regions close to the center of the galaxy, and there is concern that contamination from other components, such as streams or a warped disk, could be affecting the observations. Extending further out in radius, as we do in this contribution, allows us to eliminate this uncertainty. But most importantly it allows us to examine a different region of the halo, one that is less dominated by the remnants of massive accretions.

1.5. *Purpose of the Present Study*

In this contribution we are building on an earlier wide-field survey of Andromeda with the Wide Field Camera (WFC) at the Isaac Newton Telescope (INT; Ibata et al. 2001a; Ferguson et al. 2002; Irwin et al. 2005). This panoramic survey covered the entirety of the disk and inner halo of the galaxy out to ~55 kpc (see Fig. 1), which, combined with follow-up kinematics from Keck DEIMOS (Ibata et al. 2004, 2005; Chapman et al. 2006) and deep *HST* Advanced Camera for Surveys (ACS) photometry in selected fields (Ferguson et al. 2005; Faria et al. 2007), opened up a new violent vision of an apparently normal disk galaxy. We found that M31 possesses of order half a dozen substructures, probably debris fragments from merging galaxies that have not yet lost all spatial coherence (Ferguson et al. 2002, 2005); that it is surrounded by a vast rotating disk–like structure, extending out to ~40 kpc (Ibata et al. 2005); that it contains a giant stellar stream of width greater than the diameter of the disk of the

Milky Way and >100 kpc long (Ibata et al. 2001a; McConnachie et al. 2003); and that underlying all of this substructure there is a kinematically hot, metal-poor halo (Chapman et al. 2006).

Thus, the inner halo region covered by the INT survey is completely contaminated by these various structures. Indeed, it was a surprising result of that survey that it is necessary to observe at much larger radius to obtain a clear measurement of the accretion rate, the incidence of substructures, the stellar mass of the accreted objects, and the global properties of the halo. We therefore embarked on the deep imaging campaign of the outer halo presented in this contribution, undertaken with MegaCam, a state-of-the-art wide-field camera at the CFHT.

One of the main aims of the present survey was to investigate the prediction of CDM cosmology that upward of 500 satellites reside in the halo of a galaxy like M31 (Klypin et al. 1999; Moore et al. 1999). The possibility remains that many dwarf galaxies are being missed in current surveys. However, we defer all discussion of this issue to a companion paper (N. Martin et al. 2008, in preparation).

The layout of this paper is as follows. In § 2 we first present the photometric data and data processing. The color-magnitude distribution (CMD) of detected sources is discussed in § 3, and their spatial distribution in § 4. The resulting maps of the stellar populations of interest are presented in § 5, continuing in § 6 with the detected streams and other spatial substructures, and in § 7 with the properties of the outer halo. The radial profiles of the stellar populations in M31 are analyzed in § 8. A short discussion of the properties of the halo of M33 is presented in § 9. Finally, in § 10 we discuss the implications of our findings and compare to previous studies, and we draw conclusions in § 11.

Throughout this work we assume a distance of 785 kpc to M31 (McConnachie et al. 2005). We also adopt the convention of using R to denote projected radius, s an elliptical projected radius, and r a three-dimensional distance or radius.

2. OBSERVATIONS

2.1. *INT Observations*

INT WFC was used in four observing runs between 1998 and 2003 to map the Andromeda galaxy over the area displayed in Figure 1. The observations were taken with the V and i filters, with exposures of 1200 and 900 s, respectively, in each of these two bandpasses. The data were obtained in dark skies, with typical seeing of 1″. A total of 164 individual fields were observed, each covering an L-shaped region of 0.33 deg^2. A small ∼5% overlap between adjacent fields was adopted to ensure a homogenous photometric survey.

The images were processed by the Cambridge Astronomical Survey Unit (CASU) pipeline (Irwin & Lewis 2001), in an identical manner to that described in Ségall et al. (2007). This includes corrections for bias, flat-fielding, and the fringing pattern. The software then proceeds to detect sources and measures their photometry, the image profile, and shape. Based on the information contained in the curve of growth, the algorithm classifies the objects into noise detections, galaxies, and probable stars. (For comparison to previous studies using this classification algorithm, throughout this paper we adopt as stars those objects that have classifications of either −1 or −2 in both colors; this corresponds to stars up to 2 σ from the stellar locus.)

2.2. *CFHT Observations*

The survey of the inner halo of M31 with the INT was complemented with a deeper survey with the CFHT MegaCam wide-field camera to probe the outer reaches of the halo of this galaxy.

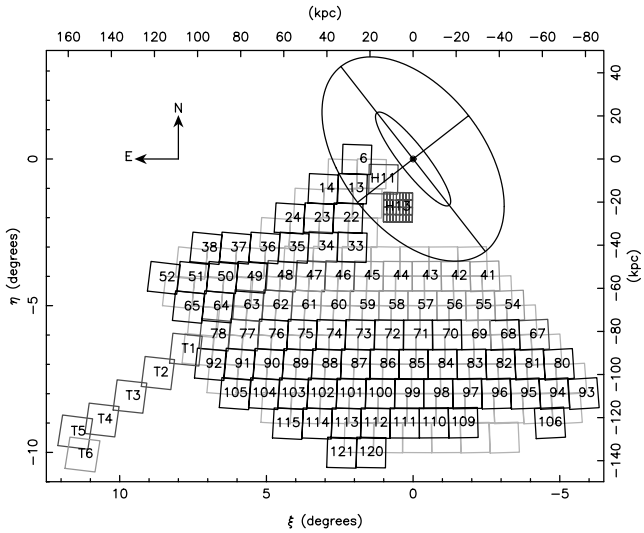

FIG. 2.—Main area surveyed with the CFHT MegaCam instrument. As we describe below, the image stability over the field of view of the camera varied slightly from one year to another. We therefore show the year that the field was observed in by a color code: red, green, and black (in the electronic edition) mark fields obtained in 2003, 2004, and 2005–2006, respectively. The field T6, centered on M33, was observed primarily in 2004, with some data in 2003. The offset fields colored turquoise (in the electronic edition) mark the positions of the short-exposure fields. In the case of field H13, we also display the layout of the 36 CCDs. The meaning of the ellipses centered on M31 is described in Fig. 1. [*See the electronic edition of the Journal for a color version of this figure.*]

MegaCam consists of a mosaic of 36 2048 × 4612 pixel CCDs, covering a 0.96° × 0.94° field, with a pixel scale of 0.187″ pixel^{-1}. The greater photometric depth and field of view achievable with this instrument make it particularly powerful in such regions of extremely low surface density of stars. The g- and i-band filters were used, totalling 5 × 290 s of exposure per field in each passband. Figure 2 displays the survey fields, while Figure 3 shows this area in relation to the environment around M31. The survey comprises 89 deep fields, observed in service mode over the 2003–2006 seasons. We chose a tiling pattern with no overlap between the deep fields, using instead short (45 s) exposures in g and i to establish a consistent photometric level over the survey. These short-exposure images were taken offset by half a field size in the right ascension and declination directions. The fields were observed in photometric conditions in good seeing conditions (typically better than 0.8″). In addition, the two inner halo fields marked H11 and H13 were retrieved from the CFHT archive. These g- and i-band images are somewhat deeper than the main survey fields with exposures of 3 × 1160 s in each passband. A further field centered on M33 (marked field T6 in Fig. 2) was obtained from the archive. After elimination of frames with poorer seeing (>1″) or CCD controller problems, 37 g-band frames and 32 i-band frames of M33 were combined, for a total of 18,306 s in the g band and 19,165 s in the i band (the detection and analysis of variable stars in this data set were presented in Beaulieu et al. 2006; Hartman et al. 2006).

The solid angle covered by the INT survey corresponds to a projected area of ∼9500 kpc^2 at the distance of M31 (∼7400 kpc^2 not overlapping with the MegaCam survey), while the MegaCam survey area subtends 1.6 × 10^4 kpc^2. This vast area encompasses several previously known structures, as we show in Figure 3. These are the dwarf galaxies M32, NGC 205, And I, And II (although we miss its center), And III, and And IX, as well as the new discoveries from this work: And XI, And XII, and And XIII, all discussed in Martin et al. (2006), and And XV and And XVI

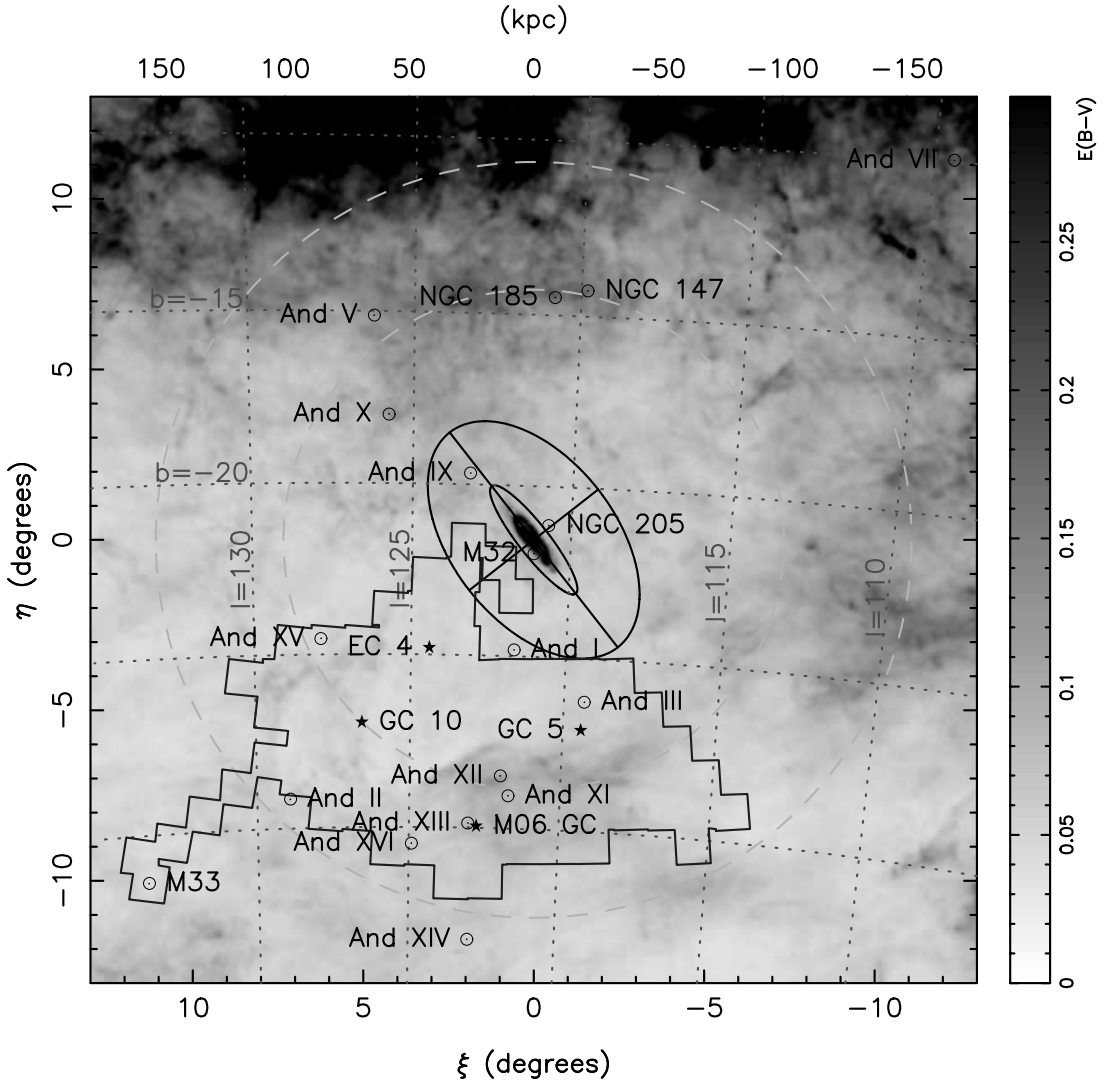

FIG. 3.— Survey region (*irregular polygon*) overlaid on a schematic diagram of M31 and surrounding Local Group structure. Note that the survey extension along the M31 minor axis reaches M33 and therefore probes the halos of both these disk galaxies. In addition to the ellipses reproduced from Fig. 1, the two concentric dashed circles show projected radii of 100 and 150 kpc. A grid in Galactic longitude and latitude has been marked. The extinction over the surveyed region, interpolated from the maps of Schlegel et al. (1998), is also shown. [*See the electronic edition of the Journal for a color version of this figure*.]

presented below. We also mark the positions of the known globular clusters in the MegaCam region: GC 5, GC 6, EC 4 (Mackey et al. 2006, 2007), and GC-M06 (Martin et al. 2006).

In addition to the INT fields and the 92 contiguous MegaCam fields, we consider below two additional fields, which are used to test the background model: a comparison field taken for a study of the Draco dwarf spheroidal (dSph) galaxy (field D7 of Ségall et al. [2007], located at $\ell = 81.5^\circ$, $b = 34.9^\circ$), and the field D3 of the Legacy Survey of the CFHT (CFHTLS). These fields were chosen from the CFHT archive as they were among the closest fields in the sky to M31 with deep exposures. The observations on the Draco dSph comparison field had slightly different exposure times to those taken for the M31 survey (950 s in g and 1700 s in i), although similar image quality. From the public release data of the CFHTLS field D3 (located at $\ell = 96.3^\circ$, $b = 59.7^\circ$), we selected a subset of the best seeing frames, totaling 2702 s in the g band and 4520 s in the i band.

The MegaCam data were preprocessed by CFHT staff using the "Elixir" pipeline, which accomplishes the usual bias, flat, and fringe corrections and also determines the photometric zero point of the observations. These images were then processed by the CASU photometry pipeline in an identical manner to that described above for the INT data. Using the multiple overlaps between deep and shallow fields, we correct the photometric solution provided by the Elixir algorithm (by up to $\sim$0.5 mag), finding a global solution over all 92 deep fields that has an rms scatter of 0.02 mag.

Using observations of the Draco dwarf spheroidal galaxy for which we had both INT WFC and CFHT MegaCam data in the (V, i) and (g, r, i) bandpasses, respectively, we determined color transformations to put the INT (Vega calibrated) photometry onto the MegaCam AB photometric system. The advantage of using the Draco field is that the region has also been covered by the SDSS, providing an external check to the photometry. Note that the MegaCam (g, i) bands are not identical to the SDSS (g', i'), although the conversions between these two systems have been determined by the CFHT staff. We refer the interested reader to Ségall et al. (2007) for further details. The conversion

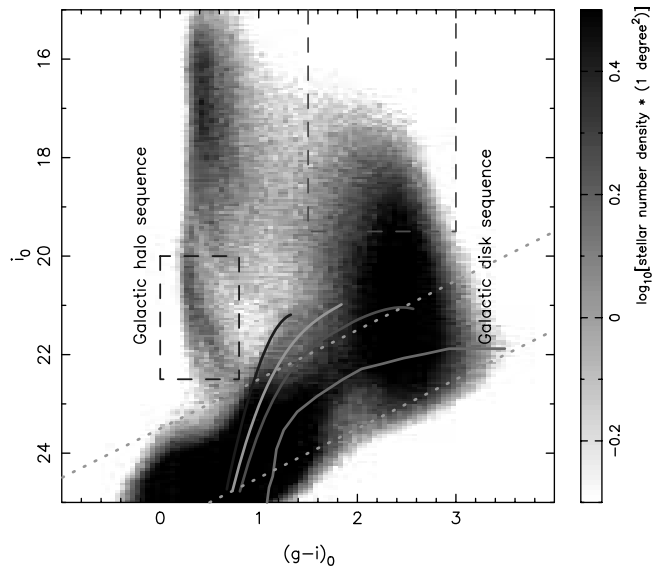

FIG. 4.—Combined CMD of the MegaCam survey fields of M31, except fields T5 and T6, which are excluded because they are dominated by stars from M33 (including young stars in the disk), and fields 6, H11, and H13, which are close to the M31 disk. The fiducial RGBs correspond to, from left to right, NGC 6397, NGC 1851, 47 Tuc, and NGC 6553, which have metallicities of [Fe/H] = −1.91, −1.29, −0.71, and −0.2, respectively. The sequences have been shifted to a distance modulus of $(m - M)_0 = 24.47$. The dashed rectangles show the regions selected to probe the foreground Galactic halo (*upper*) and Galactic disk (*lower*). The two dotted lines mark $g_0 = 23.5$, where incompleteness sets in (see Fig. 16), and $g_0 = 25.5$, which we consider the limiting magnitude of the survey. [*See the electronic edition of the Journal for a color version of this figure.*]

between INT Vega (V, i) and MegaCam AB (g, i) was found to be

$$i_{\rm MC} = i_{\rm INT} + 0.332,$$

$$g_{\rm MC} = \begin{cases} -0.419 + 1.400(V-i)_{\rm INT} + i_{\rm MC}, & (V-i)_{\rm INT} < 1.621, \\ 0.155 + 1.046(V-i)_{\rm INT} + i_{\rm MC}, & (V-i)_{\rm INT} > 1.621. \end{cases}$$

In order to enable the construction of maps over the combined area of the INT and CFHT surveys, we converted the INT photometry to (g, i) using these relations. The conversion appears to be adequately accurate, judging from the photometry of bright stars (with magnitudes in the range $18 < g < 20$ and $18 < i < 20$) in the large overlap region between the two surveys: the rms scatter around zero offset was found to be <0.02 mag in both bands.

Given the huge area of the survey, it is necessary to be aware of variations in the interstellar extinction that will affect the depth of the photometry. In Figure 3 the surveyed area is superimposed on a map of the extinction derived from Schlegel et al. (1998); the maximum i-band extinction over the halo region observed with MegaCam is $A_i = 0.27$ mag, with a mean of $A_i = 0.1$ mag. Thus, the extinction is neither very high nor very variable, although we nevertheless correct for it using the Schlegel et al. (1998) maps. In all the discussion below, g_0 and i_0 refer to extinction-corrected magnitudes.

3. COLOR-MAGNITUDE DISTRIBUTION OF SOURCES

As well as encompassing a large fraction of the halo of M31, the survey also intersects a substantial volume of the foreground Milky Way. This is clearly seen in Figure 4, where we show the combined CMD of all stars in the deep MegaCam fields of the main survey, except for fields T5 and T6, close to M33, and fields 6, H11, and H13 close to M31. Prominent at $(g - i)_0 > 1.5$ and $i_0 < 23$ is the sequence of Galactic disk dwarfs; the vertical sequence is the result of low-mass stars accumulating in a narrow color range, yet being seen over a large range in distance along the line of sight. In addition, on the blue side of this diagram, at $(g - i)_0 < 0.8$ and $i_0 < 23$, resides the Galactic halo sequence. Usually, this is seen as a smooth vertical structure, due to stars at or close to the main-sequence turnoff at increasing distance through the Galactic halo. Curiously, however, in these fields toward M31 the sequence bifurcates, indicating that the Galactic halo is not spatially smooth along this line of sight. This issue is explored in detail in a companion article (Martin et al. 2007).

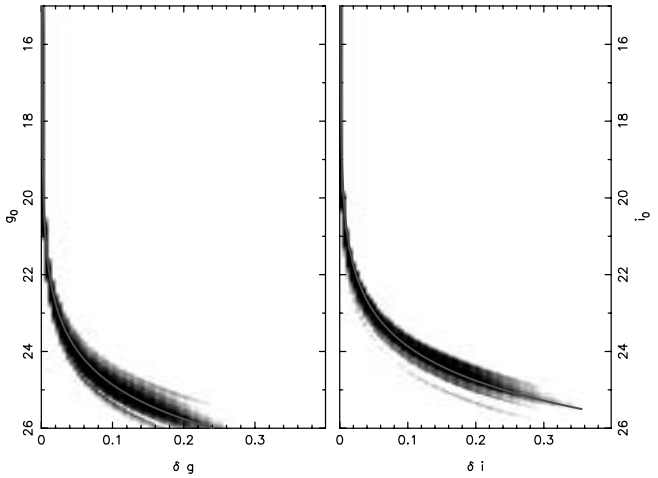

FIG. 5.—Distributions of photometric uncertainty in g_0 (*top*) and i_0 (*bottom*), together with simple exponential fits (*gray lines*). Some fields have slightly better photometry than others, giving rise to the inhomogeneous aspect at faint magnitudes. [*See the electronic edition of the Journal for a color version of this figure.*]

The stellar populations of immediate interest to this study are revealed by the RGB stars that span the globular cluster fiducial sequences that have been overlaid on the CMD. The bluemost and redmost sequences correspond to clusters of metallicity [Fe/H] = −1.91 and −0.2, respectively, so the survey is sensitive to stars of a wide range of abundance. At the limiting magnitude of $i_0 \sim 24.5$, the survey can in principle detect horizontal branch stars (see Martin et al. 2006), although of course the contamination at these magnitudes, mostly from unresolved background galaxies and noise artifacts, is very large. Nevertheless, down to $i_0 \sim 24.0$ the photometric quality remains excellent, as we show in Figure 5, with $\delta i < 0.1$ mag.

There are substantial variations of stellar populations between fields, as we demonstrate in Figure 6. Figure 6*a* displays the CMD of field 46, which lies in a dense area of the so-called giant stream (Ibata et al. 2001a), and clearly contains a numerous population of RGB sources with a wide spread of metallicity. Figure 6*b* shows the photometry of field 106 in the far outer halo; no obvious RGB is discernible visually in this diagram, although, as seen later in § 7, the combination of this with several other outer fields does allow a detection of the stellar halo of M31. For comparison, we also display the CMDs of the reference fields near the Draco dSph (Fig. 6*c*) and the CFHTLS field D3 (Fig. 6*d*). The photometric depth of the survey clearly varies slightly from field to field (note that the images from which the CMDs in Figs. 6*a* and 6*b* were constructed had identical exposure times). The data taken in the 2005 and 2006 runs (of which Fig. 6*b* is an example) were very homogenous in depth, whereas the earlier 2003 and 2004 runs were more patchy. It is likely that the improvement in the 2005 and 2006 seasons was a result of the correction of the

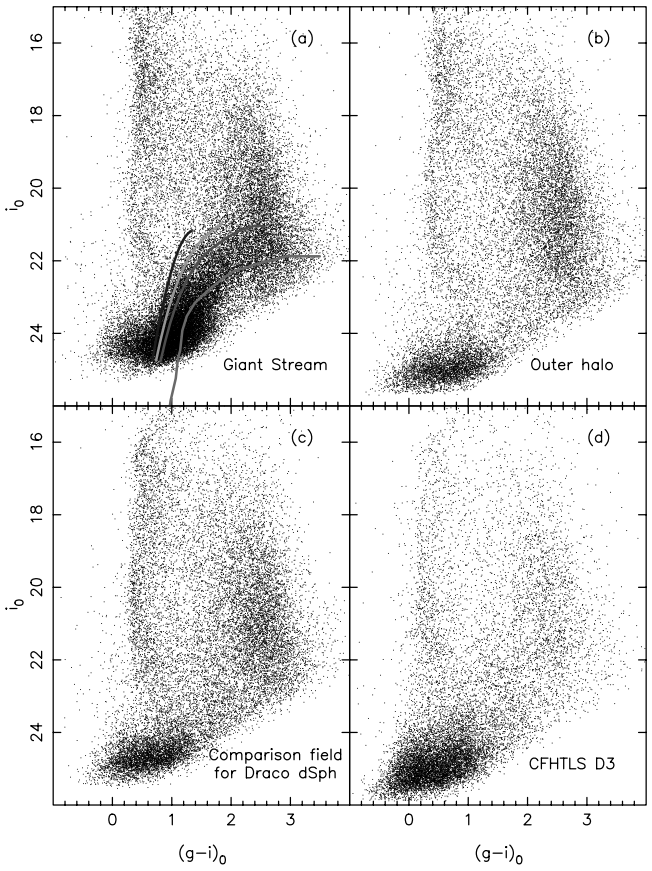

FIG. 6.—Top panels show sample CMDs of point sources in the MegaCam survey: (*a*) is for field 46, in a dense region within the giant stream, while (*b*) is for field 106, in the outer halo. The bottom panels correspond to the comparison fields: (*c*) lies near the Draco dSph, while (*d*) is constructed from the CFHTLS field D3. As in Fig. 4, the lines in (*a*) are the RGB ridgelines of globular clusters of metallicity (*left to right*) [Fe/H] = −1.91, −1.29, −0.71, and −0.2. The dense grouping of objects with $-0.5 < (g-i)_0 < 1.5$ is mostly due to misclassified compact galaxies. [*See the electronic edition of the Journal for a color version of this figure*.]

detector plane tilt,[8] allowing a uniform focus to be achieved over the $0.96^\circ \times 0.94^\circ$ field of view. (For comparison to Fig. 6, in Fig. 7 we show the CMD of sources classified as galaxies.)

Although the globular cluster RGB ridgelines shown in Figures 4 and 6 are useful to show the behavior of known stellar populations, the set of four templates is too sparse to allow accurate comparisons to be made with the distant M31 population. Instead, we chose to adopt the Padova isochrones (Girardi et al. 2004), which conveniently have been calculated in the Sloan passbands. Figure 8 shows the isochrones we used, converted into the MegaCam photometric system, which were chosen for a population age of 10 Gyr. For each star in the survey, a photometric metallicity was calculated by interpolating between the RGB curves. The assumption that the stellar populations have an age of 10 Gyr over the entirety of the survey is clearly incorrect (Brown et al. 2006a), but this is probably a reasonable estimate for the majority of the stars at large radius.

As we have shown in Figure 3, the region surveyed with MegaCam includes several known sources. For comparison to the populations encountered below, and as a check of the reliability of the photometry, we display their CMD structure in Figure 9.

[8] See http://www.cfht.hawaii.edu/News/Projects/MPIQ/.

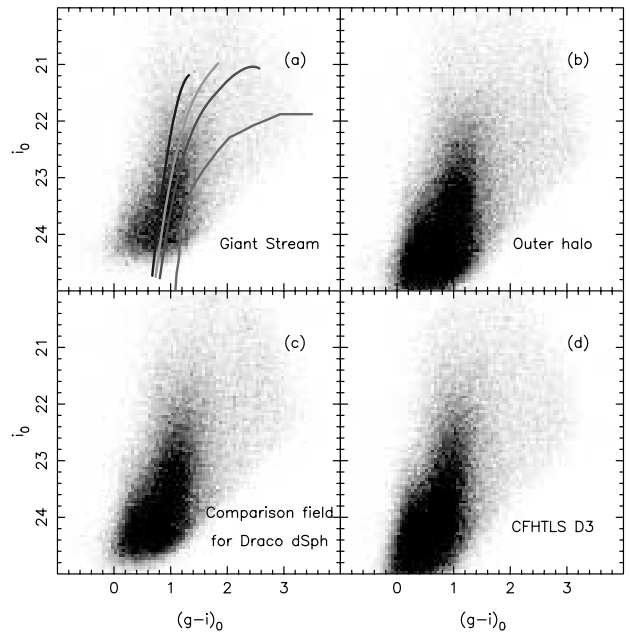

FIG. 7.—Same as Fig. 6, but for sources classified as galaxies by the image analysis algorithm. [*See the electronic edition of the Journal for a color version of this figure*.]

4. SPATIAL DISTRIBUTION OF SOURCES

Although the MegaCam camera covers a large area, there are large inter-CCD gaps in the mosaic that were not filled by our chosen dithering pattern with five subexposures. These gaps are partially filled by the short exposures but of course reach to a much shallower limiting depth. These inter-CCD gaps are seen in Figure 10, which shows the stellar density in one of the MegaCam fields. Another problem that is not limited to the MegaCam data are the halos of bright stars that effectively render useless certain regions of the detector mosaic. The effect of these halos is also illustrated in Figure 10. Both the gaps and bright star holes could

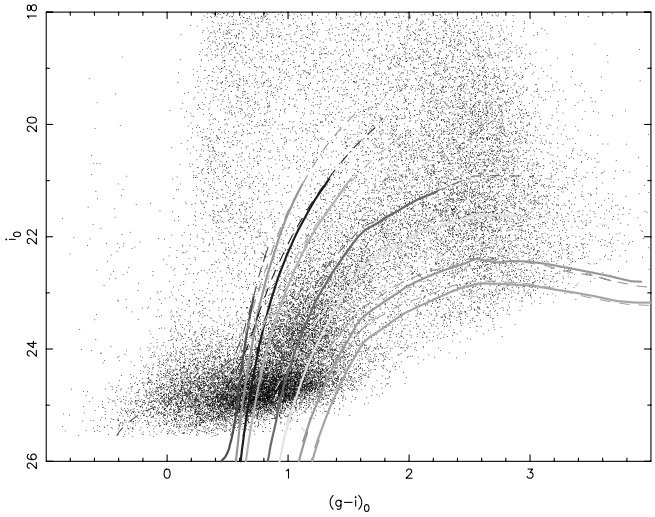

FIG. 8.—Padova isochrones superimposed on the CMD of field 47. The isochrone models are all for 10 Gyr and [Fe/H] metallicities (*left to right*) of −3 (actually $Z = 0$), −2.3, −1.7, −1.3, −0.7, −0.4, 0.0, and +0.2. The solid line part of each of these curves corresponds to the RGB, while the horizontal branch and AGB are indicated with dashed lines. [*See the electronic edition of the Journal for a color version of this figure*.]

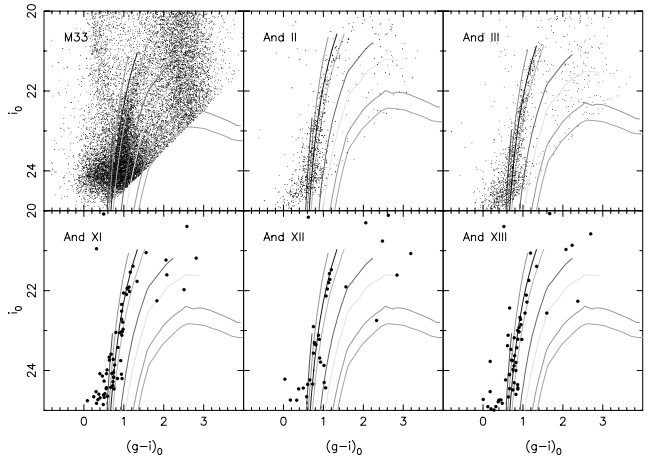

FIG. 9.—CMDs of known satellite galaxies in the MegaCam survey region. The Padova isochrones from Fig. 8 are reproduced here. For M33 we show the sources within an annulus between 1° and 2°, while for And II, And III, and the remaining dwarfs, we show the sources within a circular region of 12′, 6′, and 12′, respectively. For the purposes of overlaying the isochrones, we adopt the distance moduli 24.54 ± 0.06 for M33, 24.07 ± 0.06 for And II (both from McConnachie et al. 2004a), and 24.37 ± 0.07 for And III (McConnachie et al. 2005), while for And XI, And XII, and And XIII (Martin et al. 2006) we assume the distance modulus of M31: 24.47 ± 0.07 (McConnachie et al. 2005). [*See the electronic edition of the Journal for a color version of this figure*.]

easily be accounted for in the analysis of the surface density, by simply correcting for the missing area. However, we found this approach to be somewhat unsatisfactory when making maps of spatial resolution smaller than the area of the bright star halos. For purely cosmetic reasons we chose to replace the affected areas with nearby counts: the inter-CCD gaps were filled with the detections of the CCD immediately to the south, while the bright star halos were filled with detections either to the east or west of the hole (depending on the location of the field edge or other nearby bright stars). Figure 10 shows an example of the procedure adopted. A further problem was that in several fields observed in 2003 the data for CCD 4 of the MegaCam mosaic were absent due to a CCD controller malfunction. For these fields, which comprise fields 48, 63, 77, 92, H11, H13, T2, T3, T4, and T5, we copied the sources from CCD 3, adjacent on the mosaic. These cosmetic alterations only concerned 3% of the total surveyed area and so are unimportant for the analysis of large-scale features. However, since these procedures could give rise to small-scale artifacts, we flagged all the sources that were added artificially and checked carefully all of the detections of substructure presented below.

The final catalog contains a total of 19 million sources. However, many of these sources are foreground and background contaminants, so we must assess their numbers and distribution before being able to analyze the distribution of genuine M31 stars. In Figure 11 we show the spatial distribution of Galactic disk dwarf stars with $1.5 < (g-i)_0 < 3.0$ and $15.0 < i_0 < 19.5$; from an inspection of Figure 4 it can be seen that these stars are located at brighter magnitudes than the tip of the M31 RGB and should therefore be an almost pure Galactic sample. Figure 11 shows that this is not entirely correct, as a strong enhancement of sources is seen in the inner regions of M31 and M33, due to the presence of blue loop stars and asymptotic giant branch (AGB) stars in the disks of those galaxies. Ignoring these disk regions, we detect a smooth gradient toward the Galactic plane in the north, with no obvious structures.

In addition to the Galactic disk dwarfs, there is some contamination from distant bright main-sequence halo stars, as we

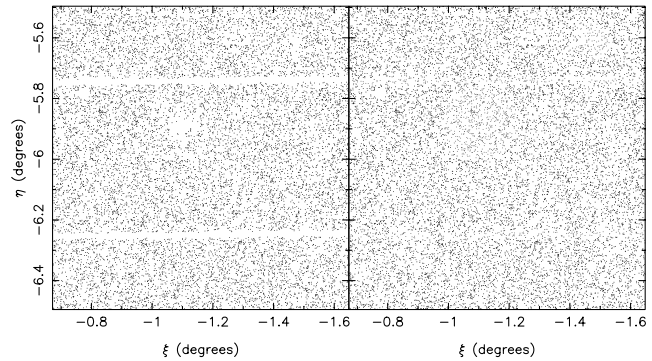

FIG. 10.—As an example of our correction technique for the effect of bright stars, we show in the left panel the distribution of stellar sources in field 70, a field containing several unusually bright stars. The two horizontal gaps are due to a physical gap between the first two and the last two rows of detectors on the mosaic camera. The lower source density at $\xi \sim -1.1°$, $\eta \sim -5.9°$ is due to a bright star halo. In the right panel, we show the corrected counts in this region, where the stars in the affected region have been deleted and replaced with artificial sources (*gray points*) that were copied from adjacent areas of the sky. [*See the electronic edition of the Journal for a color version of this figure*.]

showed in Figure 4. The distribution of these sources is discussed in detail in Martin et al. (2007), but to first approximation they populate the survey region uniformly.

A further source of contaminants are background galaxies. Most of these are readily identifiable from their image parameters, although there will be some distant compact galaxies that are unresolved with the typical depth and seeing achieved in this survey. The map of the sources classified as galaxies by the algorithm is displayed in Figure 12. Apart from the usual filamentary signature of large-scale structure there is no apparent correlation with either the Milky Way, Andromeda, or M33, beyond the disks of the latter two galaxies (where some sources are classified as being extended due to image crowding). The CMD of these contaminants is displayed in Figure 7 for four selected fields. These resolved galaxies are approximately as numerous as the point sources in the dense giant stream fields but become up to 6 times more numerous than point sources in the outer halo fields. Clearly a small error in image classification toward fainter

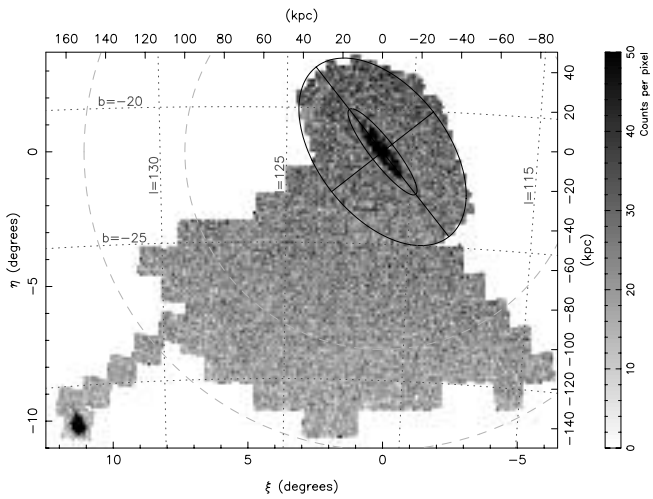

FIG. 11.—Distribution of stars within the color-magnitude selection box $1.5 < (g-i)_0 < 3.0$ and $15.0 < i_0 < 19.5$, which outside of the inner regions of M31 and M33, which contain blue loop and AGB stars, gives a clean sample of Milky Way disk dwarf stars. The map is a linear representation of the star counts, with pixels of size $0.1° \times 0.1°$. [*See the electronic edition of the Journal for a color version of this figure*.]

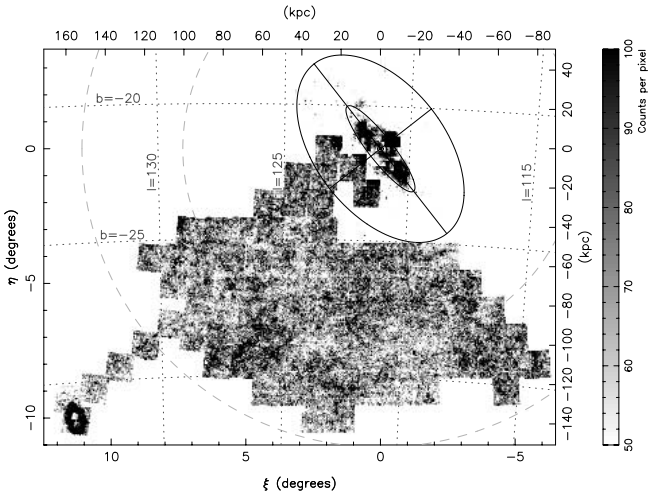

FIG. 12.— Same as Fig. 11, but showing the distribution of objects classified as extended sources over the survey region. Due to the high source density in the disks of M31 and M33, some point sources are blended and are classified as galaxies by the photometry software. A pixel size of $0.05^\circ \times 0.05^\circ$ has been used. [*See the electronic edition of the Journal for a color version of this figure.*]

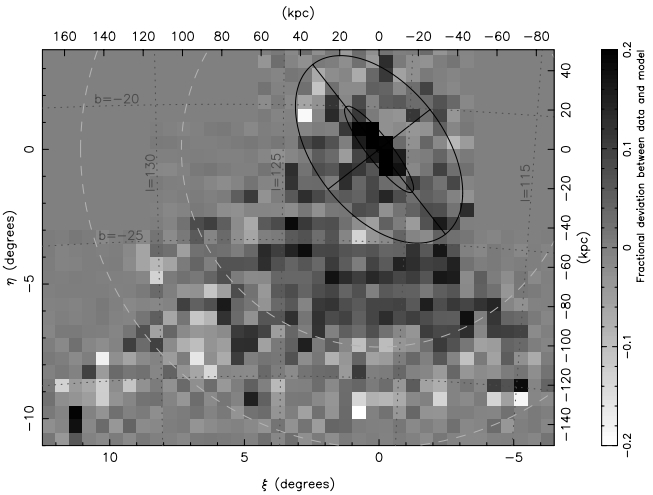

FIG. 13.— Map of the fractional residuals between the Galactic disk selection previously presented in Fig. 11 and the Besançon model predictions [calculated as (data − model)/model for each $0.5^\circ \times 0.5^\circ$ bin]. Ignoring a 2° circle around M31 and a 1° circle around M33, the average difference is less than 2%. A slight gradient is visible in this image, amounting to 0.002 ± 0.0006 deg^{-1} toward the Galactic plane (again ignoring the same regions around the two galaxies). [*See the electronic edition of the Journal for a color version of this figure.*]

magnitudes could have a significant repercussion in the measured density of point sources. We return to this issue in the following section.

4.1. *Foreground Subtraction*

We had originally envisaged using the MegaCam comparison fields presented in Figure 6 to subtract off the background counts; however, since the Galactic contamination varies substantially from these fields to our M31 fields of interest, and even varies significantly over the main area of this vast survey, we decided to investigate whether Galactic models could be used instead to predict the contamination more reliably. To this end, we tessellated the survey area with $0.5^\circ \times 0.5^\circ$ bins and generated simulated catalogs using the Besançon Galactic population model (Robin et al. 2003). All stellar populations in the model with *i*-band magnitudes between $15 < i_0 < 26$ were accepted. To reduce shot noise in the randomly generated catalogs, at each spatial bin we simulated a 10 times larger solid angle and later corrected the density maps for this factor. Finally, the artificial photometry was convolved with the observed magnitude-dependent uncertainty function (from Fig. 5).

We were impressed to discover the accuracy to which the Besançon model predicts the star counts toward our fields. For the Galactic disk sample selected with $1.5 < (g - i)_0 < 3.0$ and $15.0 < i_0 < 19.5$ (*lower dashed rectangle in* Fig. 4), whose observed spatial distribution was presented previously in Figure 11, the Besançon model correctly predicts the observed counts over the survey area to better than 2%. The fractional residuals between the observations and the model are shown in Figure 13. This distribution shows a slight gradient, increasing by a factor of 0.002 ± 0.0006 deg^{-1} toward the Galactic plane. This means, for instance, that if we renormalize the model to fit the data at the southern end of the survey, the model would underpredict the star counts at the northern end by ~2%.

Evidently the Besançon model has the correct ingredients to reproduce very accurately the Galactic disk star counts toward these fields around M31. However, we need to investigate the model further before we can use it with confidence. The color-magnitude region that is of particular interest to us is the region where the RGB of M31 has its greatest contrast over the contaminants. We return to this in more quantitative detail later, when we discuss the matched filter method, yet a visual inspection of Figure 4 shows that the color interval will be approximately in the range $0.8 < (g - i)_0 < 1.8$, where we avoid the bulk of the Galactic disk contamination, and also the faint blue contaminants, which are most likely unresolved background galaxies. In Figure 14 we display the observed luminosity function in this color interval (in black), as well as the corresponding Besançon model predictions (in gray) for the two representative fields and the two reference fields that we presented previously in Figures 6 and 7. The correspondence is excellent from $i_0 = 15$ down to $i_0 = 20.0$, with a Kolmogorov-Smirnov (K-S) test probability that the observations are drawn from the model of greater than 10% for all four fields. In Figure 14*a* the observations depart strongly from the model for $i > 21$; this is, however, completely expected, as the field contains the RGB of Andromeda at these magnitudes. Figure 14*b* is for field 106 in the outer halo, and Figure 14*c* is the Draco dSph comparison field; in both cases the model predictions are extremely close to what is observed: the K-S test over the range $15 < i_0 < 24$ gives 27% and 9% probability, respectively, that the observed and modeled distributions are identical, and the total counts agree to within better than 2 σ. However, for the CFHTLS field D3, shown in Figure 14*d*, the Besançon model predictions over the full range $15 < i_0 < 24$ do not accurately match the observations (K-S test probability <0.01%). This failure toward the direction ($\ell = 96.3^\circ$, $b = 59.7^\circ$) shows that one cannot adopt the Besançon model blindly; evidently the real Galaxy is more complex than that model allows for, although it is not clear whether the difference is due to an inaccuracy in the global model of the halo component or to a local deviation from a globally correct halo model (due perhaps to halo substructure in that direction). Despite this shortcoming, we consider these comparisons to have been very encouraging. The Besançon model predicts reasonably well the details of the star counts toward our two comparison fields, and it predicts perfectly well the star counts in the outer halo field (Fig. 14*b*). Very similar results were found on widening the color range to $0.5 < (g - i)_0 < 1.8$, to include the bluest RGB stars of interest. Given the variations in the luminosity function that are clearly visible in Figure 14, it is evidently

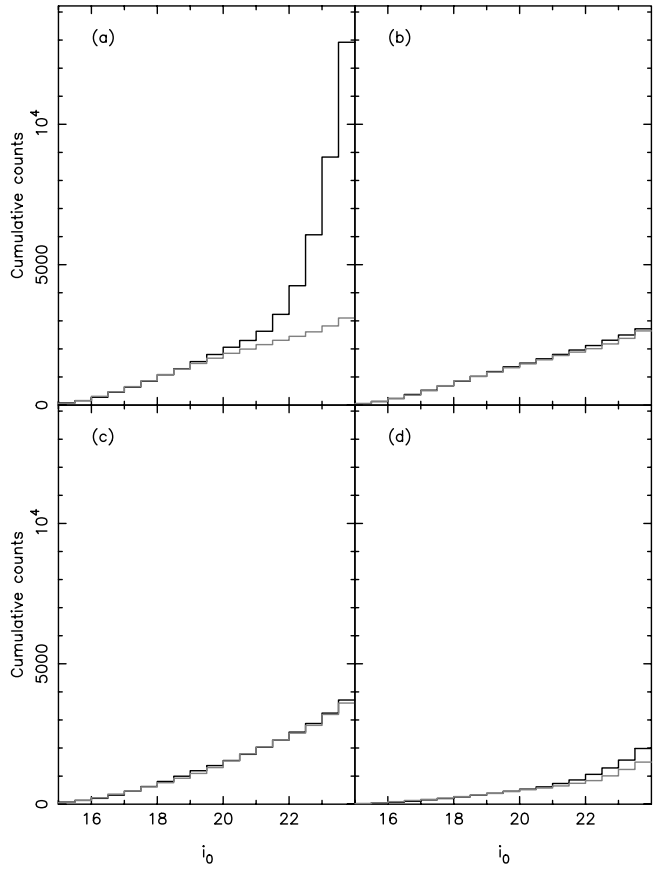

FIG. 14.—Luminosity function of point sources in the color range $0.8 < (g-i)_0 < 1.8$ for the sample fields shown previously in Figs. 6 and 7: (*a*) field 46, (*b*) field 106, (*c*) the Draco dSph comparison field, and (*d*) the CFHTLS field D3. The observed luminosity functions are shown in black, while the gray lines show the Besançon model predictions. In (*a*) the stellar populations of the giant stream cause the large increase in counts beyond $i_0 = 21$. The correspondence between observations and model in (*b*) and (*c*) is excellent, although there is a significant departure in (*d*). A limiting *g*-band magnitude of $g_0 < 25.5$ was imposed to data and models alike. [*See the electronic edition of the Journal for a color version of this figure*.]

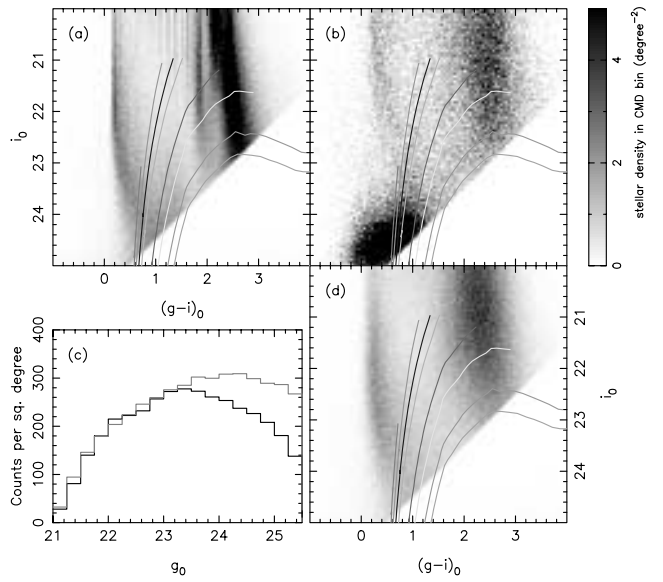

FIG. 15.—(*a*) CMD of sources from the Besançon model for the MegaCam comparison fields; the model predictions have been smoothed with the observational errors in Fig. 5. (*b*) Corresponding observed distribution. Clearly, in reality the stellar populations have a much wider color spread than the model predicts. To alleviate this problem, we have introduced an additional smoothing to the model, as detailed in the text. In (*c*) the ratio of the luminosity function in the color range $2.0 < (g-i)_0 < 3.0$ of the model (*gray*) and the data (*black*) is used to compute an empirical completeness correction, which applied to the color-magnitude data gives the distribution shown in (*d*). (A *g*-band limit of $g_0 = 25.5$ has been imposed throughout.) [*See the electronic edition of the Journal for a color version of this figure*.]

better to use the model to subtract off the expected contamination rather than use a comparison field located at a different Galactic latitude and longitude. This is true even for relatively nearby fields: the difference in the predicted luminosity function of foreground stars in Figures 14*a* and 14*b* is substantial.

The excellent agreement between the observations and the model predictions in Figures 14*b* and 14*c* is somewhat surprising given the fact that we did not apply any incompleteness corrections to the model and have not corrected for contaminating background unresolved galaxies. We chose not to perform artificial star completeness tests for this survey, as it would have been a prohibitively expensive undertaking, and refer instead to a previously computed comparison between MegaCam and *HST* photometry from the center of the Draco dSph. As we show in Figure 2 of Ségall et al. (2007), the completeness of MegaCam down to $i = 24$ from data of similar exposure time is greater than 80%. Note, however, that this completeness was calculated in a relatively crowded central field of the Draco dSph (not the Draco comparison field shown in Figures 6*c*, 7*c*, and 14*c*) and is therefore likely to be substantially worse than what we face in the almost empty fields in the outer halo of M31. In the MegaCam observations of M31, crowding is not at all important, and any incompleteness will be due mostly to faint stars being lost in the halos around bright stars and areas with strong scattered light.

Despite these successes of the Besançon model, it unfortunately fails to predict the correct CMD. The reason for this is apparent from a visual inspection of Figure 15*a*, in which we present the predicted CMD over the MegaCam fields 93, 105, 106, 115, 120, and 121, which are all located at the outer edge of the survey near a projected radius of 150 kpc (in the analysis below we refer to these fields as the "background" fields; for reference, the number of stars in the background fields as a function of metallicity and limiting magnitude is listed in Table 1). Comparing the distribution in Figure 15*a* to its observed counterpart in Figure 15*b*, we see that the model has features that are too sharp, despite the convolution with the photometric uncertainties. This is likely due to the model not containing a realistic spread of stellar population types, in particular the color-magnitude sequences are evidently not as varied in the model as in reality.

To alleviate this problem, we have introduced an additional smoothing to the model. From a Gaussian fit to the color distribution of Galactic halo and Galactic disk populations in the

TABLE 1

STAR COUNTS (PER SQUARE DEGREE) IN THE BACKGROUND FIELDS 93, 105, 106, 115, 120, AND 121 IN THREE SELECTED METALLICITY INTERVALS AS A FUNCTION OF LIMITING *i*-BAND MAGNITUDE

	[Fe/H] INTERVAL		
LIMIT	[−3.0, −1.3]	[−1.3, −0.7]	[−0.7, 0.0]
$i_0 < 22.0$	100.7	241.6	726.0
$i_0 < 22.5$	150.2	292.0	1262.3
$i_0 < 23.0$	208.3	346.5	1429.5
$i_0 < 23.5$	274.0	425.8	1538.1
$i_0 < 24.0$	386.5	568.0	1690.1

magnitude range $20 < i_0 < 21$ (where the sequences are almost vertical in the CMD), we measured the intrinsic FWHM of the observed distributions. By introducing a color-dependent additional Gaussian spread to the model of $\sigma = 0.05 + 0.075(g - i)_0$, we find a similar color spread in the halo and disk populations to the observations. (This spread is significantly larger than the 0.02 mag rms scatter in the zero-point calibration of the photometry between fields, which suggests that it is indeed the model that does not have a sufficient spread of stellar populations, rather than the photometric errors being underestimated.)

In Figure 15*c* we compare the luminosity function in the color range $2.0 < (g - i)_0 < 3.0$ in the resulting smoothed model (*gray*) with that of the data. We see an excellent match down to $g_0 = 23.25$, after which the model begins to diverge, due to the effects of incompleteness, as well as any errors in the model and the presence of contaminating background galaxies. We use the ratio of these distributions beyond $g_0 = 23.25$ to correct the model; the resulting final model for the background region is displayed in Figure 15*d*.

The excellent agreement of the Besançon model with our observations to $g_0 = 23.25$ indicates that the number of background galaxies masquerading as point sources cannot be a substantial fraction of the total counts down to these photometric limits. Beyond this limit, some background galaxy contamination may offset the incompleteness, in which case it will be hidden in the empirical completeness correction adopted for the background fields.

The Besançon model, smoothed and corrected for incompleteness, as discussed previously, can now be used to predict the expected foreground contamination, for stars of color and magnitude that will masquerade as M31 halo stars. In Figure 16 we show two such predictions over the area of the study. Figure 16*a* shows the equivalent surface brightness of the star count model for stars with metallicities $-3 < [\mathrm{Fe/H}] < +0.2$ interpolated from the Padova models shifted to the distance of M31. Figure 16*b* shows a similar map for $-3 < [\mathrm{Fe/H}] < -0.7$, which is substantially fainter than that of Figure 16*a* because this metallicity interval excludes most red stars from the Galactic disk sequence (as can be seen in Fig. 15).

To construct Figure 16, we have converted the predicted Galactic star counts to an "equivalent surface brightness" Σ_V in the V band, as if these contaminants were RGB stars in M31. The motivation for converting the measured star counts into surface brightness is of course to be able to compare our observations to previous studies and also to theoretical predictions. However, the procedure requires some further explanation. Both for the model and for the survey data, we convert the MegaCam g- and i-band photometry into the V band using the color equation above. The resulting V-band luminosities are summed for the stars in a spatial and/or color-magnitude bin, but we must still correct for the fact that we are only observing RGB stars that represent only a fraction of the total luminosity. By comparing the RGB star counts of And III down to a limiting magnitude of $i_0 = 23.5$ with the integrated magnitude of $m_V = 14.4 \pm 0.3$ of this dwarf galaxy (McConnachie & Irwin 2006), we measure an offset of 2.45 mag. This is consistent, and similar, to the value of 2.3 mag estimated in the same manner by Martin et al. (2006) for a limiting magnitude of $i_0 = 24$. Furthermore, as seen below in § 8, with this offset we obtain a good correspondence between the profile of metal-poor stars and the V-band surface brightness profile derived from integrated light (Irwin et al. 2005). Clearly the uncertainties in this simple correction are large: we are implicitly assuming that the underlying population has the same luminosity function as And III for all metallicities. The equivalent surface brightness measurements we present below must therefore be interpreted with caution, as they are likely to contain substantial systematic errors. However, the interested reader who may wish to convert these surface brightness profiles back to the reliable measure of luminosity-weighted star counts (to a limiting magnitude of $i_0 = 23.5$) can do so by simply subtracting 2.45 mag.

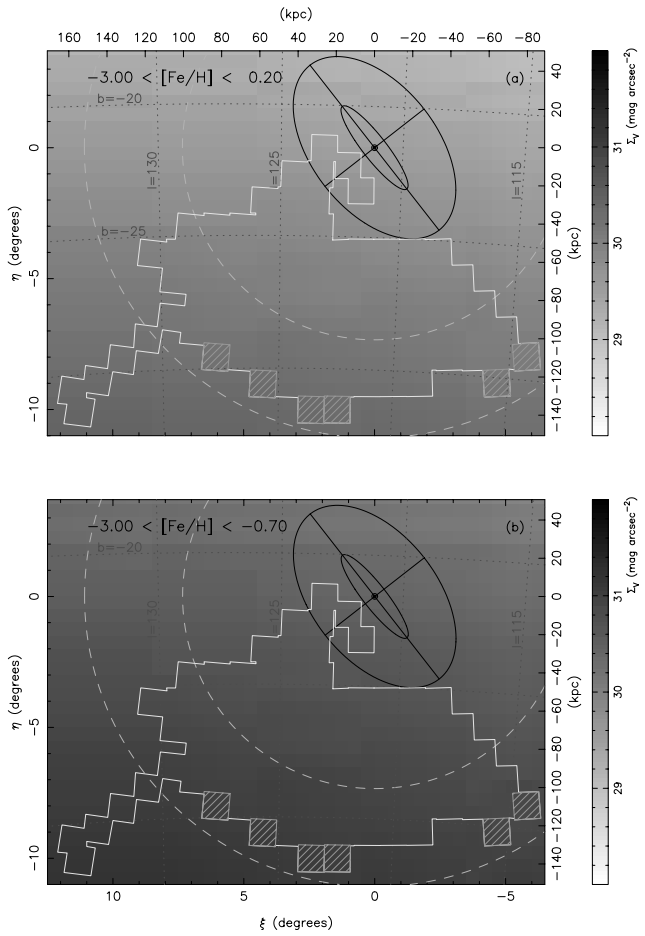

FIG. 16.—Spatial distribution of the Besançon model (calculated for each $0.5^\circ \times 0.5^\circ$ bin) over the survey region for two different color-magnitude selections: (*a*) is for Galactic stars that have color and magnitude in the region occupied by stars in M31 of metallicity in the range $-3.0 < [\mathrm{Fe/H}] < +0.2$ according to the 10 Gyr Padova models; (*b*) is for the more restricted range $-3.0 < [\mathrm{Fe/H}] < -0.7$. The hatched squares show the location of the "background" fields (93, 105, 106, 115, 120, and 121), which are used to normalize the model. [*See the electronic edition of the Journal for a color version of this figure.*]

The predicted distributions such as those shown in Figure 16 are the best means we have to subtract foreground contamination from the spatial maps. However, we found that we could improve on the foreground subtraction in color-magnitude (Hess) diagrams by using the observed CMD in the six background fields (93, 105, 106, 115, 120, and 121) appropriately scaled according to the model to account for the predicted density variations over the survey. A different scaling correction is adopted for each metallicity interval.

Figure 17*a* shows the CMD of the MegaCam fields shown previously in Figure 4, with the contamination removed statistically. The subtracted CMD displays a clear RGB-like population, with a broad range of metallicity, although the detection of the more metal-rich populations is clearly hampered by the observational g-band limit. In order to investigate the luminosity function along this RGB, we select stars with interpolated metallicities in the range $-2.3 < [\mathrm{Fe/H}] < -0.7$ (i.e., between the green and

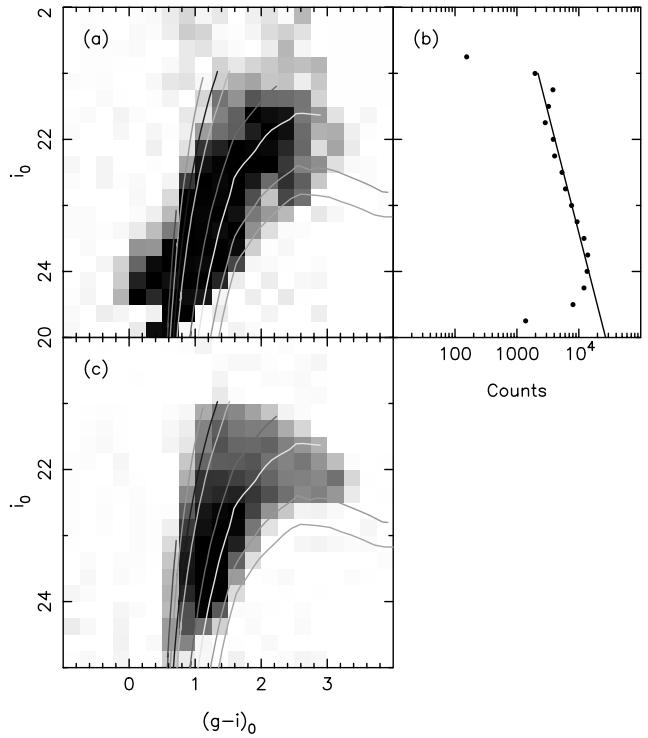

FIG. 17.—(*a*) Hess diagram of the MegaCam fields previously shown in Fig. 4, with foreground and background contamination subtracted by comparison to six background fields as detailed in the text. The Padova isochrone models from Fig. 8 are reproduced to help guide the eye. (*b*) Luminosity function of stars with $-2.3 > [\mathrm{Fe/H}] > -0.7$. (*c*) Matched filter weight map, trimmed to the color-magnitude region encompassing stars of metallicity $-3.0 < [\mathrm{Fe/H}] < +0.2$. (Both gray-scale maps are shown on a linear scale, with the photometry limited to $g_0 < 25.5$.) [*See the electronic edition of the Journal for a color version of this figure*.]

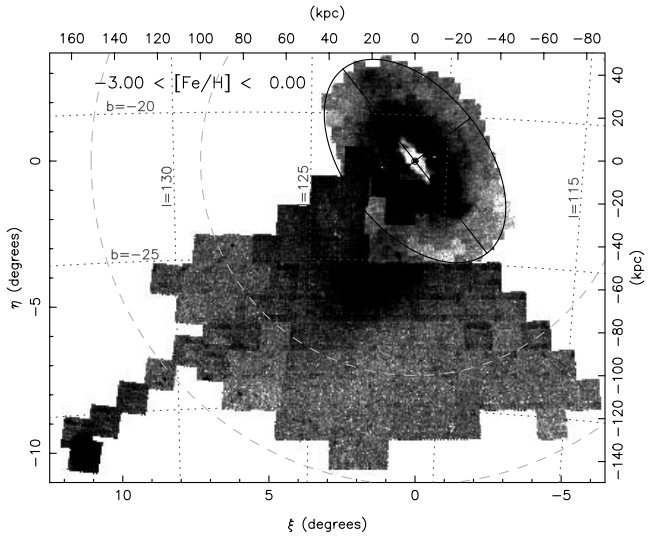

FIG. 18.—Matched filter map to $i_0 = 24.5$ ($i_0 = 22.8$ over the INT survey region). The artifacts of the MegaCam fields observed in the 2003 and 2004 seasons are clearly seen. A logarithmic scale is used for the representation. [*See the electronic edition of the Journal for a color version of this figure*.]

pink isochrones). The result is shown in Figure 17*b*, together with a simple fit. A linear fit in log (counts) is precisely what is expected for an RGB population (Bergbusch & Vandenberg 2001). If this statistical foreground subtraction is reliable, over 10^5 halo RGB stars belonging to M31 are detected over these MegaCam fields.

5. STELLAR POPULATION MAPS

Having shown that there is a relatively clean signal of the expected RGB of M31 in the combined data, we now proceed to mapping out these stellar populations. A very powerful technique for revealing a signal buried under heavy contamination is the so-called matched filter method, which is an optimal search strategy (in a least-squares sense) if one has a precise idea of the properties of the signal and the contamination. The properties could be, for instance, the spatial properties of the population of interest (a characteristic size or shape), as well as those of the contamination. Alternatively (or in addition), one may use the CMD, or whatever other physical properties of these populations that have been measured.

To apply the matched filter method, one simply weights each datum by the ratio of signal to contamination expected for that datum given its parameters. The resulting ensemble of weighted data can then be analyzed in the usual way. However, the advantage this effort has afforded us is that the distribution of weighted data will optimally suppress the contamination, revealing best whatever signal is present. In the particular situation confronting us here, we know the CMD of the signal of interest, as we have just presented in Figure 17*a*, and as discussed above, the MegaCam "background" fields (93, 105, 106, 115, 120, and 121) give us a reasonable model for the color-magnitude behavior of the contamination in the absence (or near absence) of that signal. The ratio of these two CMD distributions gives the weight matrix, which we show in Figure 17*c*. Here we have trimmed the weight matrix down to the maximum possible physical interval ($-3.0 < [\mathrm{Fe/H}] < +0.2$). Note that, as expected, the greatest weight arises at faint magnitudes in the color range $0.75 < (g-i)_0 < 1.5$, so of course stars with this photometric property will contribute most strongly in the following matched filter maps.

Figure 18 displays a matched filter map over the entire survey region, where we have chosen a limiting magnitude ($i_0 = 24.5$), a metallicity range ($-3.0 < [\mathrm{Fe/H}] < 0$), and a gray-scale representation to highlight the survey defects. The sky region surveyed by the INT is clearly not as deep as the outer MegaCam region, causing the sharp edge along the MegaCam survey boundary. However, the most important defects visible here are the long horizontal stripes, which are present on the top and bottom row of CCDs in the 2003 and 2004 data, but not after the camera refurbishment in 2005. The effect is due to a deterioration of the point-spread function (PSF) in those areas, causing stars to appear elliptical and similar to barely resolved galaxies. We spent a considerable amount of effort adapting our processing software to correct for this effect, but although substantial improvement was obtained compared to the star counts derived assuming a constant PSF, the problem could not be removed entirely, since some galaxies intrinsically have ellipticity and major-axis position angle similar to the deformed PSFs. We also attempted to correct the maps by calculating the equivalent of a flat field for star counts from the median of many fields. However, this was not implemented for the maps presented here, as the defects were found to be insufficiently stable, so that the computed corrections introduced other artifacts of almost the same amplitude as those they corrected for. Instead, the problem is largely removed by choosing a brighter limiting magnitude and virtually disappears if we adopt $i_0 = 22.8$ as in Figure 19, the limit of the INT photometry (Ibata et al. 2001a). Of the remaining artifacts, the most obvious remaining are the handful of shallow INT fields mainly clustered around ($\xi = 0^\circ, \eta = -3^\circ$), which were observed in conditions of poorer seeing than average, and of course the hole in the

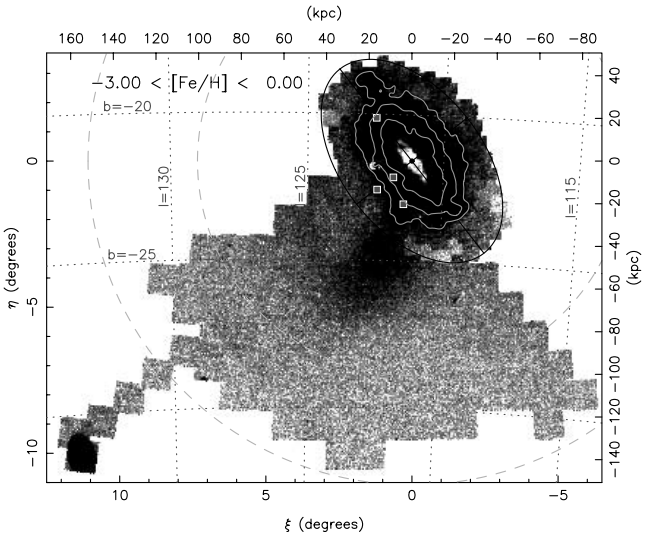

FIG. 19.—Same as Fig. 18, but to the limiting depth of the INT survey ($i_0 = 22.8$ for S/N ~ 10). The map is virtually free of obvious artifacts over the entire region observed with MegaCam. The contours show the approximate location of the surface brightness levels $\Sigma_V = 27$, 28, and 29 mag arcsec^{-2} (actually derived from the data in Fig. 50, but shown here to avoid duplication of that diagram). The locations of the *HST* ACS fields of Brown et al. (2003, 2006a, 2006b, 2007) discussed in § 10 are indicated with squares (the ACS field sizes have been exaggerated for display purposes). [*See the electronic edition of the Journal for a color version of this figure*.]

star counts at the center of M31, where the photometry of individual stars broke down due to very high crowding.

In Figure 20 we present the matched filter maps for six different ranges in metallicity. The limiting magnitude over the MegaCam region was chosen to be $i_0 = 23.5$; this is motivated by the location of the peak of the luminosity function in Figure 17*b* and is significantly brighter than the main bulk of contaminating compact background galaxies that become dominant at $i_0 \sim 24.5$. However, we keep a limit of $i_0 = 22.8$ (S/N ~ 10) for the INT survey, which gives rise to the obvious discontinuity around $\eta \sim -3^\circ$. These maps possess a bewildering amount of information on a large range of spatial scales and surface densities, so it is impossible to display all the information at a given pixel scale or with a given color representation. The diagrams in Figure 20 have been constructed to show the large-scale distribution of stellar populations in the MegaCam region of the survey, while retaining some sensitivity to small structures such as dwarf galaxies, which have scales of a few arcminutes; in each row the right panel shows a higher resolution version of the selection in the left panel; the lower resolution maps are useful for appreciating the large-scale behavior of the diffuse components. We start our discussion with Figure 20*b*, which displays the metal-rich selection ($-0.7 < [\mathrm{Fe/H}] < 0.0$). Although noisy, we can discern many features:

1. The elliptical but irregular distribution of stars with axis ratio $\sim$0.5 and major-axis diameter $\sim 5^\circ$ ($\sim$70 kpc), containing several previously reported substructures (Ferguson et al. 2002). As we have argued elsewhere (Ibata et al. 2005), this is a giant rotating component with mean metallicity of $[\mathrm{Fe/H}] = -0.9 \pm 0.2$, which is dominant beyond the end of the classical disk, and possibly the residue of a significant merger that occurred many gigayears ago (Peñarrubia et al. 2006).

2. The large ($\sim 1^\circ$ diameter) overdensity to the northeast ($\xi \sim 1.5^\circ$, $\eta \sim 3^\circ$), almost certainly unbound debris (Zucker et al. 2004; Ibata et al. 2005).

3. The "G1" clump at ($\xi \sim -1^\circ$, $\eta \sim -1.5^\circ$), a structure surrounding but unrelated to the luminous globular cluster G1 (Ferguson et al. 2002; Rich et al. 2004; Reitzel et al. 2004; Faria et al. 2007).

4. The giant stream (Ibata et al. 2001a, 2004), which in the INT data appears to be a linear structure stretching from very close to the center of M31 to ($\xi \sim 1.5^\circ$, $\eta \sim -3^\circ$), but which shows up as a substantially wider structure in the MegaCam survey extending to ($\xi \sim 3.5^\circ$, $\eta \sim 5.5^\circ$).

5. The streamlike "eastern shelf" (Ferguson et al. 2002), at ($\xi \sim 2^\circ$, $\eta \sim 0.5^\circ$).

6. A fainter stream on the western side of the galaxy, the "western shelf" at ($\xi \sim -1^\circ$, $\eta \sim 0.5^\circ$), and seen in the map of Irwin et al. (2005; $\xi \sim 3^\circ$, $\eta \sim -6^\circ$). Both these shelf structures have similar colors to the giant stream.

7. A previously unknown stream is seen extending between ($\xi \sim 4^\circ$, $\eta \sim -1.5^\circ$) and ($\xi \sim 3^\circ$, $\eta \sim -4^\circ$); we refer to this as stream C in the discussion below.

8. Vast expanses apparently devoid of stars over most of the southern half of the survey MegaCam.

9. A faint diffuse component is detected approximately 4° from M33.

In Figure 20*c* we show an intermediate-metallicity selection ($-1.7 < [\mathrm{Fe/H}] < -0.70$), somewhat "overexposed" to bring out better the fainter structures. In addition to the previously discussed features, we now notice the following:

1. The inner ellipse, attributed to the giant rotating component, has become larger and even more irregular. The more irregular aspect is of course consistent with the expected longer mixing times of debris at larger radius. An interesting point is that the distribution appears now to be less flattened, suggesting that this extreme color stretch may be revealing another rounder structure previously hidden beneath the flattened rotating component.

2. The dwarf galaxies And II and And III (cf. Fig. 3) become apparent.

3. Two strong localized structures, at ($\xi \sim 6.23^\circ$, $\eta \sim -2.89^\circ$) and ($\xi \sim 3.58^\circ$, $\eta \sim -8.89^\circ$), which, as we discuss below, are two new dwarf satellite galaxies.

4. A faint low surface brightness fuzz is detected on the extension of the major axis of M31, out to ($\xi \sim -5^\circ$, $\eta \sim -7^\circ$); we refer to this as the "major-axis diffuse structure."

5. A strong streamlike structure is detected between ($\xi \sim 3^\circ$, $\eta \sim -1.5^\circ$) and ($\xi \sim 2^\circ$, $\eta \sim -2.5^\circ$), which we call "stream D" below.

6. A further faint low surface brightness streamlike structure is detected toward ($\xi \sim 6^\circ$, $\eta \sim -6^\circ$), which we refer to as "stream A."

7. The extended structure near M33 is stronger.

8. The region ($\xi < 4^\circ$, $\eta < -9^\circ$) remains devoid of stars.

The more metal-poor selection in Figure 20*d* ($-2.3 < [\mathrm{Fe/H}] < -1.1$) displays essentially the same properties as in Figure 20*c*, except that a considerable amount of localized density spikes are detected, covering one to a few contiguous pixels. Among these are the newly discovered dwarf galaxies And XI, And XII, and And XIII (Martin et al. 2006). Figure 20*e* shows the most metal-poor sample ($-3 < [\mathrm{Fe/H}] < -1.70$). Now the giant stream has almost disappeared, and only And II and And III are still clearly visible as substructures, yet one also discerns a radial gradient from M31 over the MegaCam survey region. For completeness, in Figure 20*a* we show the most metal-rich selection considered here ($0.0 < [\mathrm{Fe/H}] < +0.2$), in which only the inner disk of M33 and a small portion of the giant stream are discernible, while

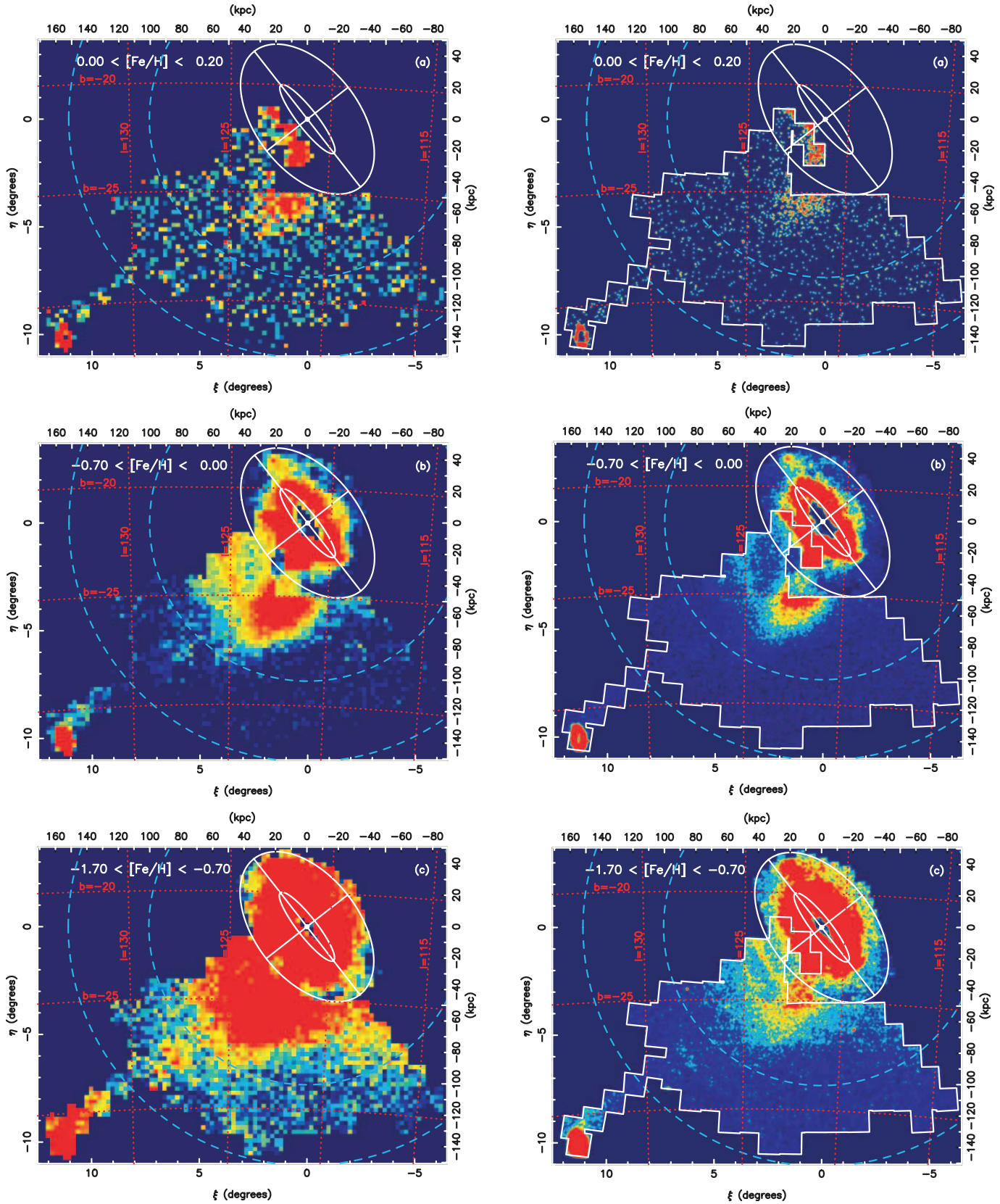

FIG. 20.— Matched filter maps to a limiting magnitude of $i_0 = 23.5$, $g_0 = 25.5$. Low-resolution images ($0.2^\circ \times 0.2^\circ$ pixels) are shown on the left in a logarithmic scale, while high-resolution versions ($0.01^\circ \times 0.01^\circ$ pixels, smoothed with a Gaussian kernel over 3 pixels) are presented on the right in linear scale.

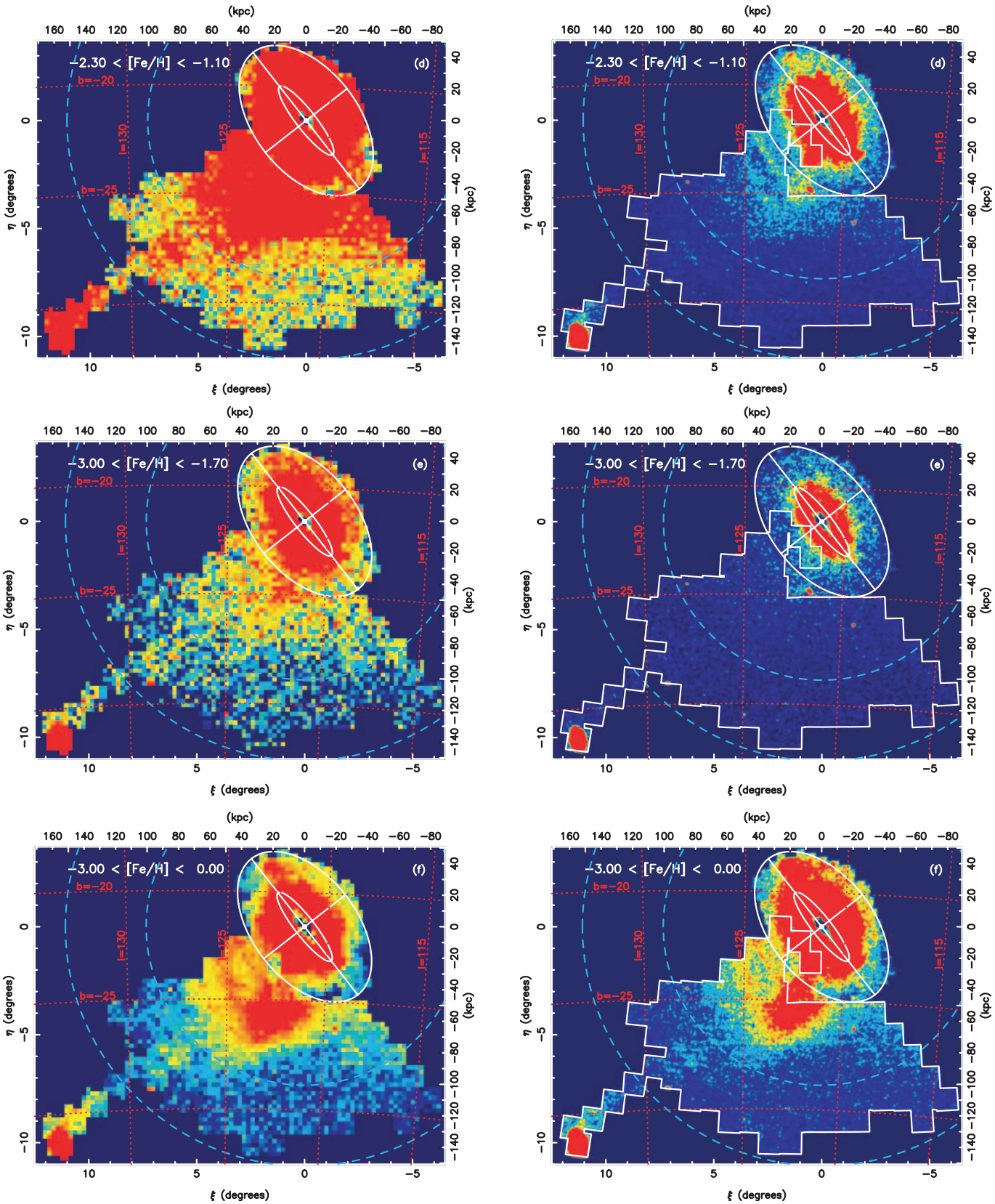

FIG. 20—*Continued*

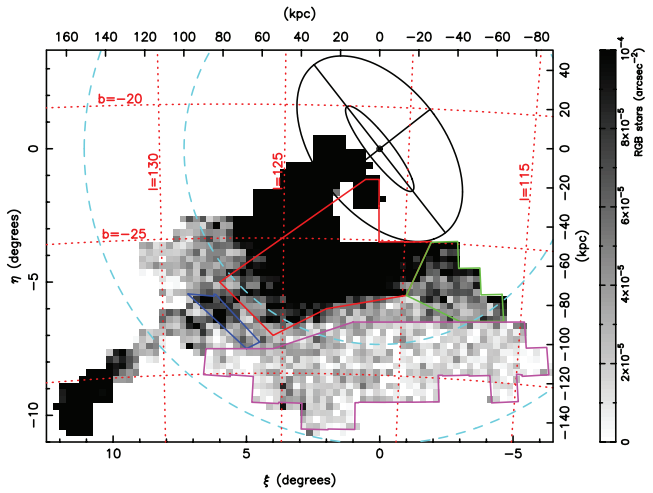

FIG. 21.—Star count map of the MegaCam region, with the foreground contamination subtracted using the Besançon model. A limiting magnitude of $i_0 = 23.5$ has been adopted. The red, green, blue, and pink polygons delineate the regions chosen to sample, respectively, the giant stream, the major-axis structure, the minor-axis stream, and the empty outer halo region.

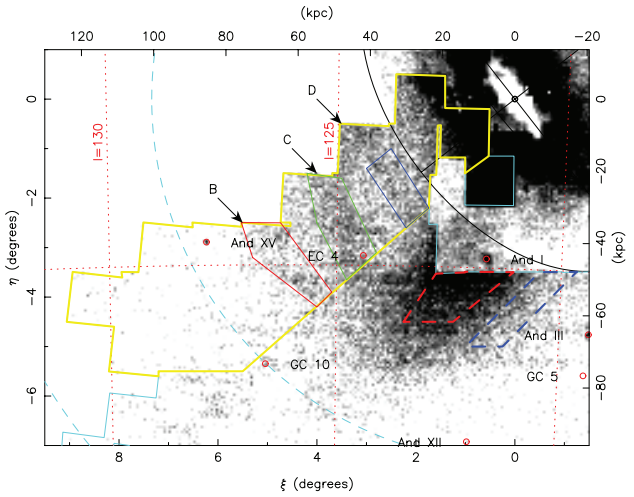

FIG. 22.—Matched filter map of the minor-axis populations with metallicity in the range $-3.0 < [\mathrm{Fe/H}] < 0.0$. The map is, again, a superposition of MegaCam and INT photometry, the differences in depth of which account for the discontinuous density distribution. The region surrounded by the yellow polygon encloses the MegaCam area used to investigate the minor-axis density profile in § 8. The red, green, and blue solid polygons enclose the streamlike structures labeled, respectively, B, C, and D. The red and blue dashed polygons enclose regions that probe the core and envelope of the giant stream.

Figure 20*f* shows the map over the full metallicity range. The increased sensitivity with the full metallicity range reveals a further feature on the minor axis with a streamlike structure between ($\xi \sim 5^\circ, \eta \sim -2.5^\circ$) and ($\xi \sim 3^\circ, \eta \sim -5^\circ$), which we refer to as "stream B."

The maps displayed in Figure 20 show the distribution of the matched filter statistic, so the resulting counts are therefore somewhat difficult to interpret directly. The reason for this is primarily that the matched filter method relies on a model of the stellar population that one desires to detect, and the statistic we measure will depend on the assumed luminosity function and how we choose to weight populations of different metallicity. A secondary reason is that, as discussed above, the foreground Galaxy counts do vary over this vast survey, so the contamination model also varies. For these reasons we also present in Figure 21 a straightforward surface density map, where we have counted up stars in the color-magnitude interval $0.8 < (g-i)_0 < 1.8$ and $20.5 < i_0 < 23.5$ and have subtracted off the corresponding Besançon model counts over the same area of sky. The main structures previously seen in Figure 20 are nicely confirmed, which we highlight in Figure 21, namely, the very extended giant stream (*red polygon*), the diffuse major-axis structure (*green polygon*), the minor-axis streamlike structure (*blue polygon*), the extended outskirts of M33, and the voids elsewhere (*pink polygon*). The advantage of this map is that we can now interpret the physical meaning of the color scale, which is shown with the wedge at the right-hand edge of the diagram. Black corresponds to 10^{-4} RGB stars per square arcsecond down to $i_0 = 23.5$. Using the conversion of star counts to surface brightness discussed above, the saturated black level translates to $\Sigma_V = 30.3$ mag arcsec^{-2}.

In the next section we discuss in more detail the populations that are highlighted in Figure 21, as well as those visible in the lower contrast map of Figure 22. To ease interpretation, in Figure 23 we show a cartoon of the positions of these populations with respect to the various structures discussed above.

6. SPATIAL SUBSTRUCTURES

6.1. *Discovery of Two Bright Satellites*

A thorough analysis of these data regarding the incidence of low-mass satellites around M31 and its implications for galaxy formation theory and cosmology will be presented in a later publication in this series (N. Martin et al. 2008, in preparation). However, we discuss briefly here two new dwarf galaxies that were discovered immediately from simple visual inspection of the star count maps. Since the analysis is identical for both objects, we include the results for And XVI in brackets.

And XV (And XVI), located at $\alpha_0 = 01^{\mathrm{h}}14^{\mathrm{m}}18.7^{\mathrm{s}}$, $\delta_0 = 38^\circ 07' 03''$ ($\alpha_0 = 00^{\mathrm{h}}59^{\mathrm{m}}29.8^{\mathrm{s}}$, $\delta_0 = 32^\circ 22' 36''$), can be noticed as an obvious enhancement in the matched filter maps presented previously. In Figures 24*a* and 25*a* we show the distribution of all detected point sources in a $9' \times 9'$ region around the dwarf galaxy. The CMD of the sources within the $2'$ ($1.5'$) radius circle

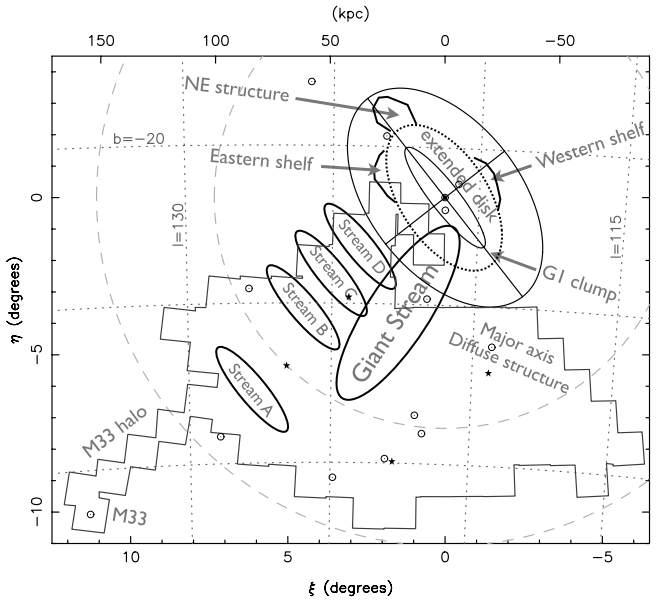

FIG. 23.—Cartoon of the main structures presented in § 5. The circled dots and star markers are reproduced from Fig. 3 and show the positions of dwarf galaxies and selected globular clusters, respectively. [*See the electronic edition of the Journal for a color version of this figure.*]

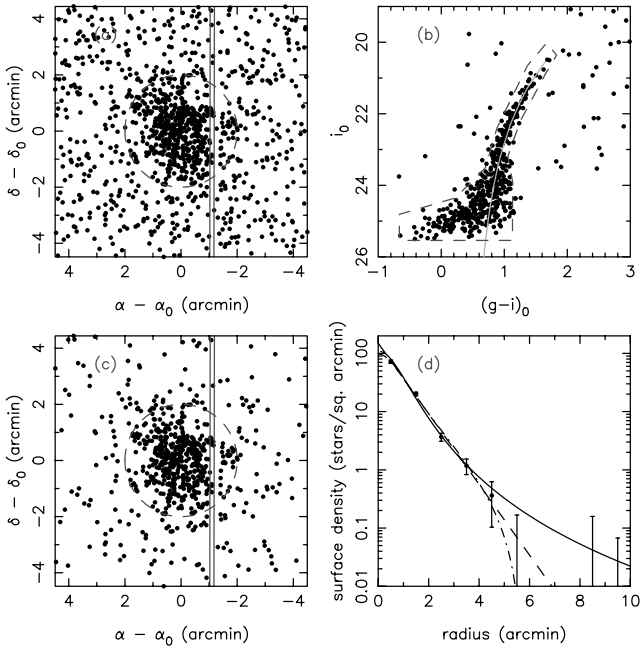

FIG. 24.—(*a*) Spatial distribution of point sources in a $9' \times 9'$ area in the vicinity of And XV. The parallel lines mark the CCD boundaries, although there is no gap at this location due to the adopted dithering pattern. The CMD of the stars within the $2'$ circular region is shown in (*b*). Selecting those stars with color and magnitude within the dashed polygon yields the spatial distribution shown in (*c*), whose radial profile is given in (*d*). The solid, dashed, and dot-dashed lines in (*d*) are, respectively, a Plummer model, an exponential model, and a King model fitted to the profile inside of $5'$. [*See the electronic edition of the Journal for a color version of this figure*.]

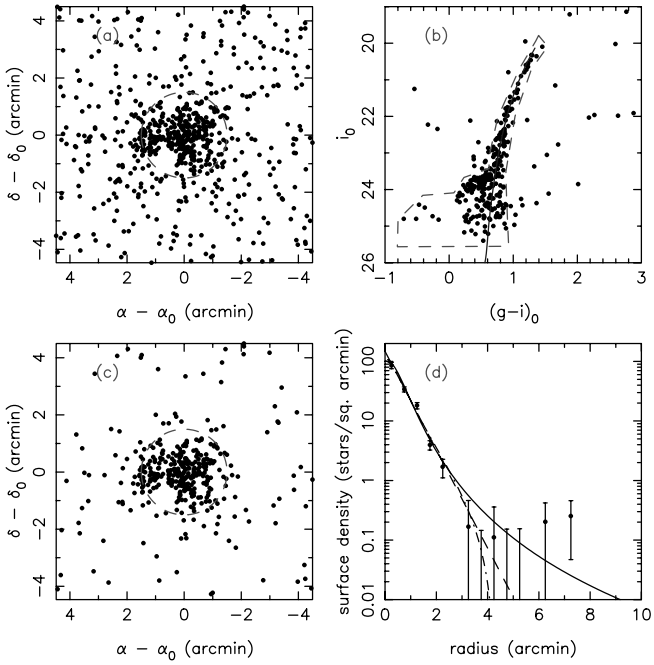

FIG. 25.—Same as Fig. 24, but for And XVI. The presence of several bright stars causes the irregular spatial distribution in the left panels. [*See the electronic edition of the Journal for a color version of this figure*.]

centered at the point of maximum density is shown in Figures 24*b* and 25*b*. A very clear and strong RGB is present. Assuming that the stars outside of the irregular polygon are contaminants, we proceed to estimate the distance of the structure using the tip of the RGB. We adopt $M_{\rm TRGB} = -4.04 \pm 0.12$ from Bellazzini et al. (2001) for the absolute *I*-band magnitude of the RGB tip and convert into the Landolt system using the color equations above and those given by McConnachie et al. (2004a); this yields a distance modulus of $m - M = 24.0 \pm 0.2$ ($m - M = 23.6 \pm 0.2$), or alternatively a distance of 630 ± 60 kpc (525 ± 50 kpc). With this distance modulus we find a reasonable visual fit to the RGB with a Padova isochrone of metallicity $[{\rm Fe/H}] = -1.1$ ($[{\rm Fe/H}] = -1.7$). Given the angular distance of 6.8° (9.5°) from M31, the object lies at an M31-centric distance of 170 kpc (270 kpc).

With the CMD selection polygon from Figures 24*b* and 25*b*, we filter out foreground contamination, which gives the distribution shown in Figures 24*c* and 25*c*. The corresponding density profile is given in Figures 24*d* and 25*d*, where we have subtracted off a background count determined from an annulus between $10'$ and $15'$. Fitting the distribution with an exponential profile (*dashed line*) yields a scale length of $0.72' \pm 0.03'$ ($0.53' \pm 0.03'$), although a Plummer model (*solid line*) of scale size $1.2'$ ($0.9'$) also fits acceptably well, as does a King (1962) model (*dot-dashed line*) with core radius of $0.91'$ ($0.64'$) and tidal radius of $5.7'$ ($4.3'$). By integrating the star counts up to the half-light radius and correcting by 2.45 mag (as above) to account for stars below $i_0 = 23.5$, we estimate a total absolute magnitude of $M_V = -9.4$ ($M_V = -9.2$).

And XVI will be a particularly interesting object for further study given its extreme distance from M31 and its location between M31 and the Milky Way, where it presumably has felt a nonnegligible perturbation from the potential of our Galaxy. It is also curious that And XV appears to be structurally disturbed and elongated, which is suggestive of the action of galactic tides. Yet how this very distant galaxy might have been affected by tides is hard to imagine. (The irregular morphology seen in the distribution of And XVI stars in Fig. 25 is an artifact of nearby bright star "holes.").

6.2. *Giant Stream*

The giant stream around M31 has been the subject of numerous studies, due to the fact that it is a nearby intermediate-mass merging event and that it can be used to measure the potential of M31. The initial discovery in the INT survey (Ibata et al. 2001a) showed the structure to be (in projection) an approximately linear and radial stream, with a metallicity slightly higher than that of 47 Tuc ($[{\rm Fe/H}] - 0.71$) and a total absolute magnitude of $M_V \approx -14$. We probed more fully its extent and the line-of-sight depth with the CFHT12K (McConnachie et al. 2003), a precursor wide-field camera to MegaCam at the CFHT. These photometric and positional data were then complemented by radial velocities obtained at four locations along the stream with DEIMOS at the Keck Observatory, which allowed a measurement of the mass of the halo of Andromeda out to 125 kpc (Ibata et al. 2004) and enabled us to develop a model of the orbital path of the stream progenitor. We found the orbit to be highly radial and predicted that the stream fans out toward the east after passing very close to the nucleus of M31, losing its streamlike spatial coherence. This analysis also posed an interesting puzzle, which is still unsolved: since the stream is on such a highly destructive radial orbit, how did the progenitor survive until so recently?

Subsequently, Guhathakurta et al. (2006) also used Keck DEIMOS to obtain spectra in one stream field, where they measured a mean metallicity of $\langle [{\rm Fe/H}] \rangle = -0.51$. The kinematic data sets were reanalyzed by Font et al. (2006), who undertook *N*-body

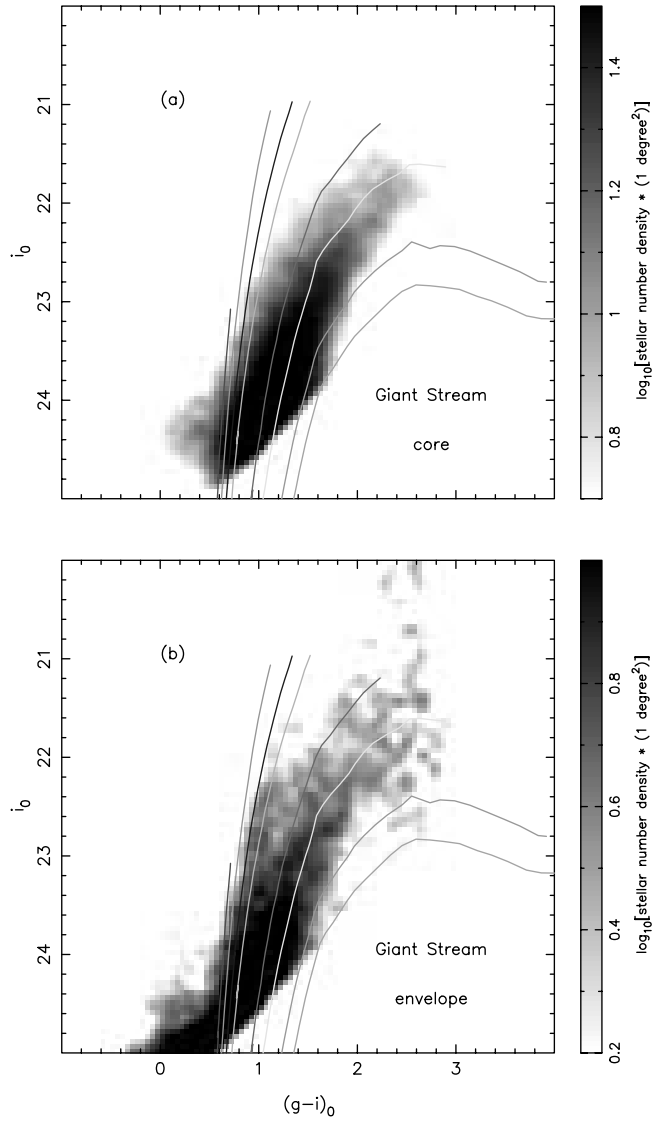

FIG. 26.—(*a*) Displays the stellar populations in the core of the giant stream (sampled in the spatial region shown with a red dashed polygon in Fig. 22), while (*b*) displays those on the periphery of this structure (dark blue dashed polygon in Fig. 22). The foreground contamination has been removed from the two Hess diagrams. [*See the electronic edition of the Journal for a color version of this figure.*]

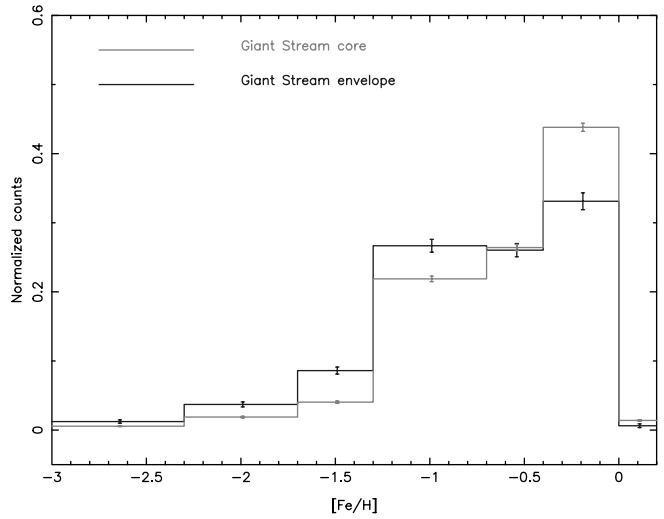

FIG. 27.—Metallicity distribution functions (with error bars denoting 1 σ uncertainties) for the giant stream core sample and the envelope sample, as interpolated from the chosen Padova isochrones. Photometric limits of $i_0 = 23.5$ and $g_0 = 25.5$ have been imposed. The background fields, normalized with the Besançon model, have been used to subtract off the expected foreground counts in each of the metallicity bins. The two distributions are completely inconsistent with each other to high confidence. [*See the electronic edition of the Journal for a color version of this figure.*]

simulations to attempt to reproduce the stream morphology. They found that the progenitor must have been more massive than $10^8\ M_\odot$ and that the time since its dissolution is a mere 0.25 Gyr. Recently, Fardal et al. (2007) have shown how the fanning out of the stream into shells to the east and west can be used to place constraints on the galaxy potential. We defer a full reanalysis of the giant stream to a subsequent contribution, focusing here on the salient new features that are revealed in the MegaCam survey.

An inspection of Figure 20 shows that the giant stream extends out to a projected radius of $\sim$100 kpc (*inner dashed circle*). With the maximum line-of-sight distance to the stream of 886 $\pm$ 20 kpc estimated by McConnachie et al. (2003) (at $\xi = 2^\circ$, $\eta = -4^\circ$), this corresponds to an apocenter distance of $\sim$140 kpc. Although this is further than it had been mapped out before, the possibility that the stream reaches this projected distance was anticipated by one of the orbit models presented in Ibata et al. (2004; cf. Fig. 4 of that paper). That particular orbit model, however, does not agree well with the measured line-of-sight distance gradient, although we note that debris does not exactly follow the orbit of the progenitor. Further detailed modeling is clearly required to understand the dynamics of this stream.

The MegaCam data also show that there are stellar population variations in the stream. We illustrate the evidence for this in Figure 26, where the CMD in the core of the giant stream (Fig. 26*a*) is compared to a region on the western periphery of the structure (Fig. 26*b*). The spatial location of these selections is shown with the dashed polygons in Figure 22, with red for the core and blue for the envelope population. Both of these spatial selections contain stars over a wide range of metallicities and peak at high mean metallicity, consistent with the mean photometric metallicity of $\langle [\mathrm{Fe/H}] = -0.51 \rangle$ measured from a kinematically selected sample of stars on the periphery of the giant stream (Guhathakurta et al. 2006). It is clear from an inspection of this diagram, however, that relative to the outer field the core is lacking the blue stellar populations (around the isochrone with $[\mathrm{Fe/H}] = -1.3$). The concentration of very "metal-rich" stars to the core of the stream can also be seen in Figure 20 (compare Fig. 20*a* to Fig. 20*c*). We note here that the metallicities inferred for these very red stars by comparison to ancient 10 Gyr isochrones are lower limits, due to the well-known age-metallicity degeneracy. While the majority of other halo populations studied in this contribution are very likely old, this is not the case for the giant stream. In the spectral sample of bright stream stars obtained by Ibata et al. (2004) many targets could be identified as AGB stars from their spectral features, which indicates that a fraction of these stars are of intermediate age. This is consistent also with the deep photometric survey in a giant stream field undertaken with the ACS instrument on board the *HST* by Brown et al. (2006a), who detected a dominant population of age $\sim$8 Gyr, as well as a younger $\sim$5 Gyr component.

The stellar population differences can be put on a more quantitative basis by constructing the metallicity distribution functions for the "stream core" and "outer stream" selections; this is displayed in Figure 27, which shows the striking difference very

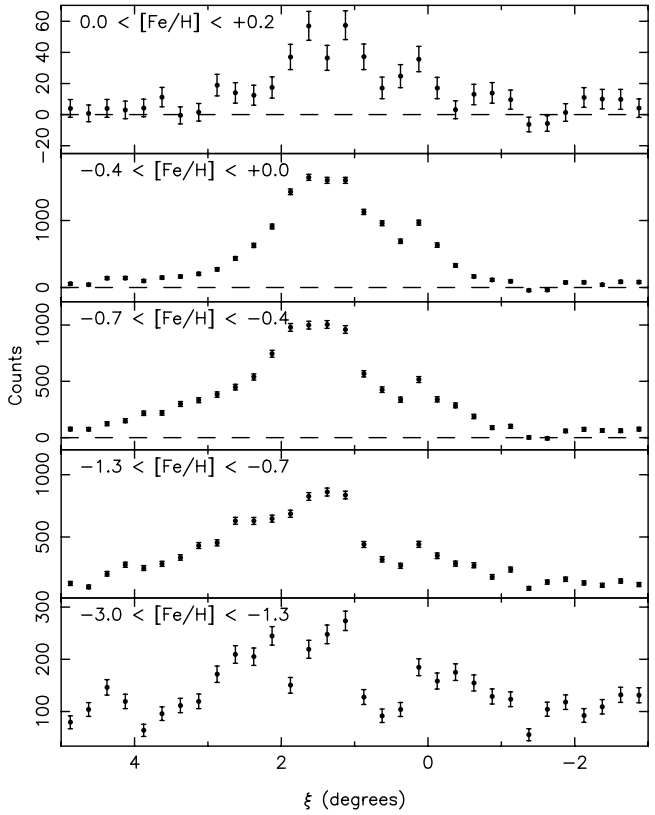

FIG. 28.—Counts in a 1° wide east-west band between $-4.5^\circ < \eta < -3.5^\circ$ for different metallicity intervals.

clearly. The core of the stream clearly has a very large fraction of red stars. Figure 28 shows the star counts in different metallicity intervals as a function of ξ in a 1° wide band between $-4.5^\circ < \eta < -3.5^\circ$. The distribution, which peaks near $\xi \sim 1.5^\circ$ for $[\mathrm{Fe/H}] > -0.4$, becomes broader for the metallicity intervals $-1.3 < [\mathrm{Fe/H}] < -0.4$.

6.3. *Major-Axis Structure*

The faint diffuse population detected on the major axis between a projected distance of 50 and 100 kpc (delineated with the green polygon in Fig. 21) is a conspicuous feature of the MegaCam survey. The average surface brightness in this region is ≈31 mag arcsec^2. The dwarf galaxy And III lies on the edge of this region, so to avoid contamination we remove the data from a 0.5° radius circle around And III for the subsequent analysis. The CMD of the area is displayed in Figure 29*a*, which clearly possesses a well-populated RGB with a dominant population of color similar to the Padova isochrones of metallicity $[\mathrm{Fe/H}] \sim -1.3$. The corresponding metallicity distribution function (MDF) in Figure 31 (*bottom line*) confirms this visual impression.

Thus, despite the visual impression that the "overexposed" density map of Figure 21 gives that the major-axis population merges with the giant stream, we find that these two stellar populations are very different and likely unrelated. This diffuse low-contrast feature has no clear spatial structure as one would expect of a stream. Indeed, it could be the inner regions of the halo, although it appears not to be a smooth roughly spherical structure since there is an obvious deficit of stars at ($\xi \sim -0.6^\circ$, $\eta \sim -6^\circ$) compared to ($\xi \sim -3^\circ$, $\eta \sim -5^\circ$). We refrain from estimating the total luminosity of the structure, since we have clearly only detected a fraction of the entire object. Additional photometry to the north and west and possibly even kinematics will be needed to understand this structure further.

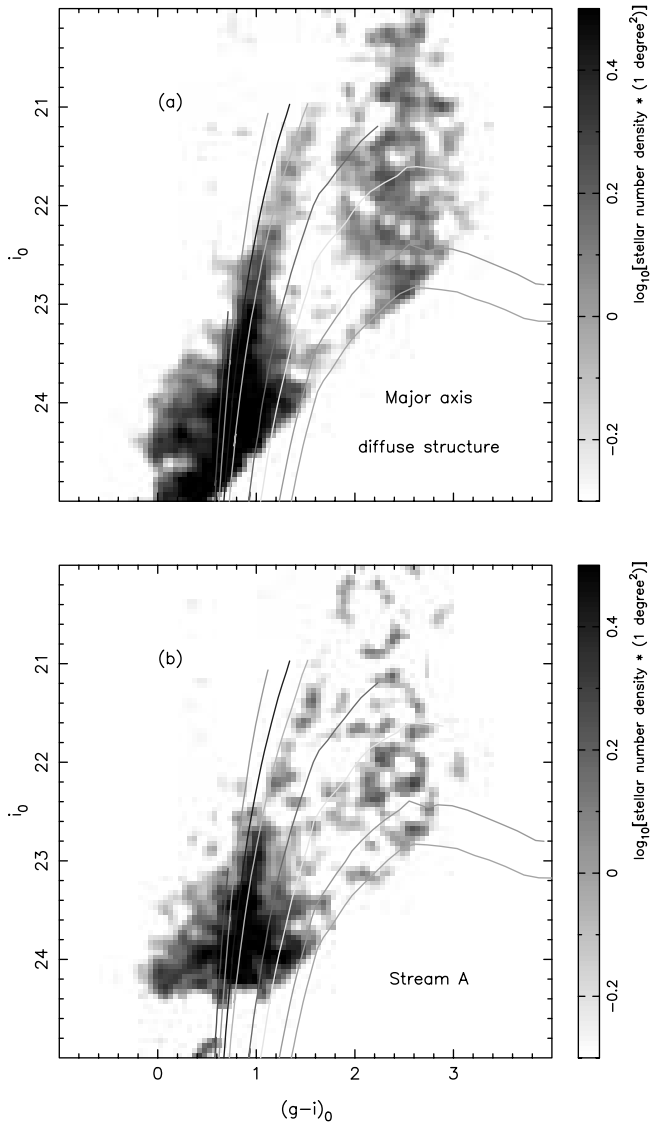

FIG. 29.—(*a*) Foreground-subtracted Hess diagram of the major-axis diffuse population over the region marked out with the green polygon in Fig. 21. (*b*) Foreground-subtracted Hess diagram of the minor-axis stream population over the region marked out with the blue polygon in Fig. 21. The gray-scale wedge on the right shows the count level per CMD bin of size 0.05 mag × 0.05 mag. [*See the electronic edition of the Journal for a color version of this figure.*]

6.4. *Distant Minor-Axis Stream "A"*

In contrast, the structure on the minor axis (delineated with the blue polygon in Figure 21, which covers 1.7 deg^2) at $R \sim 120$ kpc is much more confined spatially as can be perceived from an inspection of the matched filter maps in Figure 20. Curiously, this population (which we refer to as stream "A" in the discussion below) has a very similar CMD to that of the major-axis structure, with a dominant population again just slightly redward of the $[\mathrm{Fe/H}] = -1.3$ Padova isochrone, as can be seen in Figure 29*b*. The corresponding MDF is compared to that of the diffuse major-axis feature in Figure 30.

The structure is very faint, with an average surface brightness of $\Sigma_V \sim 31.7 \pm 0.2$ mag arcsec^{-2}. Integrating over the blue polygon in Figure 21 and subtracting the average counts at this radius calculated from the "outer halo" region (contained in the pink

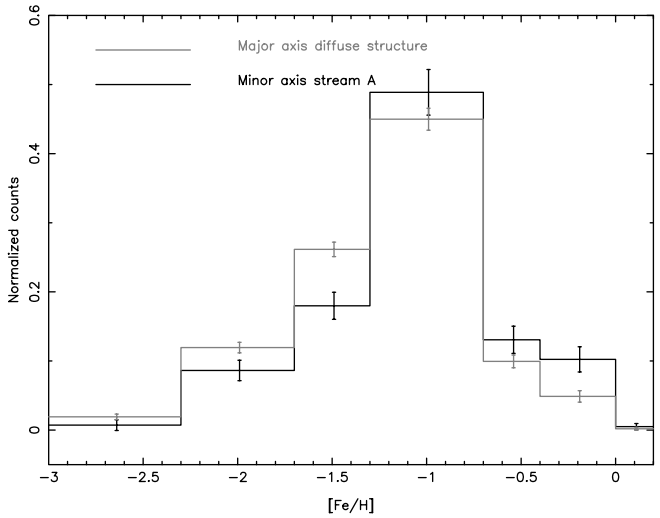

FIG. 30.—Metallicity distribution function of the major-axis diffuse structure and the minor-axis stream A population, as derived from the data in Fig. 29. [*See the electronic edition of the Journal for a color version of this figure*.]

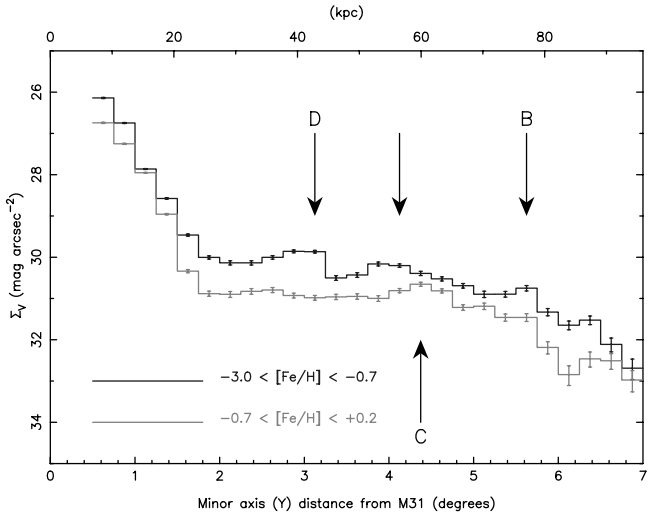

FIG. 31.—Surface density profile along the minor axis, selected from the region within the yellow polygon in Fig. 22. The arrows point out significant peaks in the profile. The positions of the labeled peaks correspond to the streams seen in Fig. 22. [*See the electronic edition of the Journal for a color version of this figure*.]

polygon) gives a total luminosity of $L_V \sim 2.3 \times 10^6\ L_\odot$ ($M_V \sim -11.1$). If we are detecting the entirety of the stars in the original structure, the progenitor must have been a galaxy similar to the Sculptor dwarf spheroidal ($M_V = -10.7 \pm 0.5$; Irwin & Hatzidimitriou 1995).

6.5. *Minor-Axis Streams at $R < 100$ kpc*

Figure 22 shows a close-up map of the minor-axis region in the proximity of M31 and the giant stream. Here we have used the matched filter technique to detect structures of metallicity in the range $-3.0 < [\mathrm{Fe/H}] < 0.0$ and have chosen a gray-scale representation that highlights the three linear structures that appear almost perpendicular to the minor axis and merge into the giant stream. Three arrows have been added to the diagram to indicate the approximate location of these streamlike features, which we denote "B," "C," and "D" in order of increasing declination.

The nature of these streams becomes more apparent if we investigate the color profile along the minor-axis region. We choose to remove the giant stream stars by selecting only those point sources within the yellow polygon in Figure 22, and we sum stars perpendicular to the minor axis (rather than taking radial bins) so as to enhance the density peaks. The corresponding foreground-subtracted surface brightness profiles are shown in Figure 31, where the top line shows the metal-poor populations with $-3.0 < [\mathrm{Fe/H}] < -0.7$ and the bottom line those with $-0.7 < [\mathrm{Fe/H}] < +0.2$. The foreground, as before, is estimated using the Besançon model. As expected, several strong peaks are detected; however, the locations of the peaks in the metal-poor subsample do not coincide with those of the metal-rich subsample, suggesting very strong stellar population differences between these streamlike features.

This deduction is borne out by the variations in the CMDs in adjacent spatial locations. In Figure 32 we display the Hess diagrams of the streamlike structures enclosed within the green, red, and blue polygons of Figure 22, and we also show the stellar population between streams B and C. The corresponding MDFs are given in Figure 33. These data show that stream D is a relatively metal-poor structure, while stream C is predominantly metal-rich. Curiously, the population contained within the gap between streams B and C has a narrow range of metallicity and is metal-rich.

These streamlike structures overlap along the line of sight (which is why we chose not to extend the stream D spatial selection polygon in Fig. 22 up to the northeastern end of the survey region). A spectacular example of this can be seen in Figure 34, which shows the CMD of MegaCam field 14, where streams C and D cohabit over essentially the entirety of the field.

Thus, although these streamlike structures appear to merge spatially with the giant stream, such that it is tempting at first sight to associate them with that huge structure, their stellar population properties are so different both from each other and from the giant stream that this proposition is untenable.

In the present survey these streams or streamlike structures are clearly truncated at the northeast edge of the data set, so it is impossible to determine their full extent or nature. Instead, we obtain a first and very rough estimate of their luminosities by integrating within the three stream polygons in Figure 22. In this way we estimate that stream B, which lies at $R \sim 80$ kpc, has a luminosity

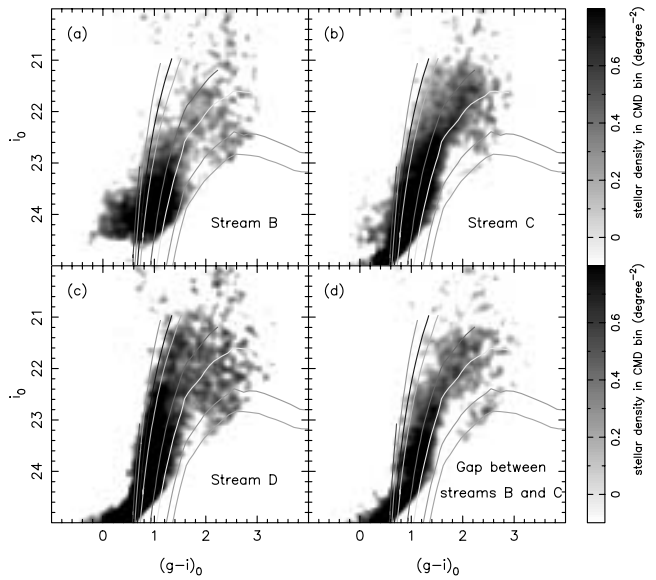

FIG. 32.—Background-subtracted Hess diagrams for four adjacent MegaCam fields near the minor axis. In (*a*)–(*d*) we display, respectively, the stellar populations present within streams B, C, and D, as well as for the gap between streams B and C. These regions are defined in Fig. 22. [*See the electronic edition of the Journal for a color version of this figure*.]

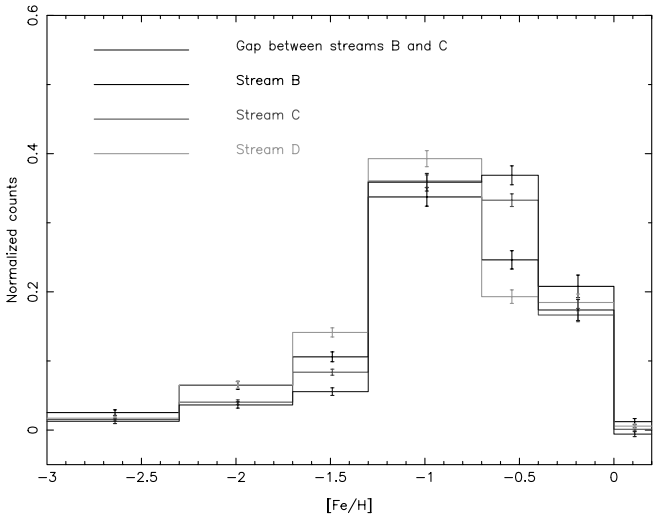

FIG. 33.—MDF determined from the four fields of Fig. 32. [*See the electronic edition of the Journal for a color version of this figure.*]

within the red polygon of $\sim 1.0 \times 10^7\ L_\odot$; stream C at $R \sim 60$ kpc has $\sim 1.4 \times 10^7\ L_\odot$ in the green polygon; while stream D at $R \sim 40$ kpc has $\sim 9.5 \times 10^6\ L_\odot$ in the blue polygon. In estimating these luminosities we have ignored the complex background in this region. Nevertheless, these estimates indicate that the progenitors of the streams were sizable dwarf galaxies, likely more luminous than the Fornax dSph. We note that the extended globular cluster (Huxor et al. 2005) EC 4 (Mackey et al. 2007) lies within or superimposed on stream C.

7. THE OUTER HALO

The primary reason for undertaking this survey was initially to investigate the large-scale structure of the halos of M31 and M33, and to some extent the substructures discussed above are a hindrance for this purpose. In particular, we had not expected the giant stream to be as extended and polluting of the inner halo as it

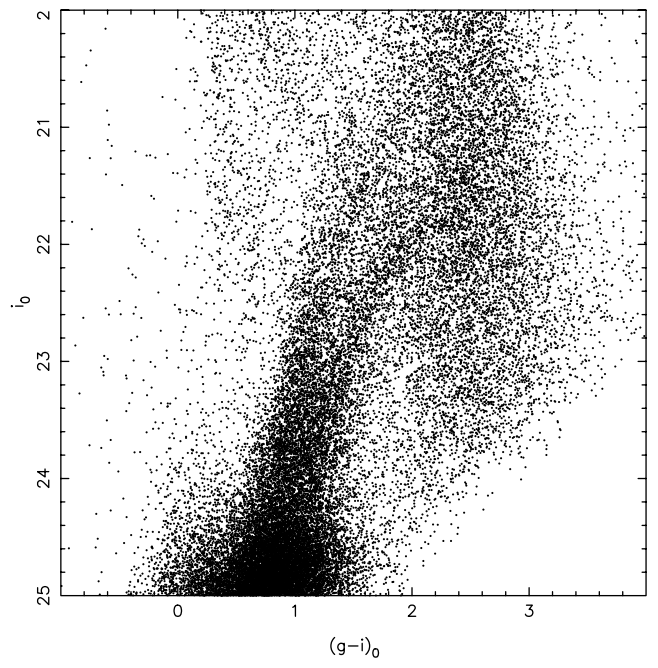

FIG. 34.—Color-magnitude diagram for field 14, showing the presence of two cospatial populations with very different RGB tracks.

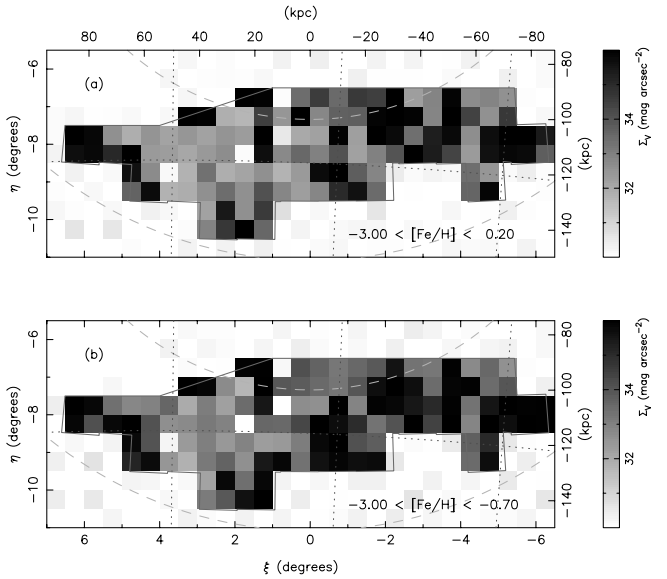

FIG. 35.—Background-subtracted maps of the equivalent surface brightness in the outer halo region. (*a*) Stars in the metallicity range $-3.0 < [Fe/H] < +0.2$; (*b*) stars restricted to $-3.0 < [Fe/H] < -0.7$, a range that suffers much less from uncertainties in the background correction. [*See the electronic edition of the Journal for a color version of this figure.*]

turned out to be, and the various "contaminating" streams along the minor axis were a surprise, as we had chosen those fields from the shallower INT survey to probe the surface density profile of the "clean" inner halo.

However, there is a relatively empty region of the survey free from obvious substructures toward the southwest. This ~ 30 deg^2 region, previously surrounded with a pink polygon in Figure 21, is reproduced in Figure 35, where we have converted the counts of stars in the various metallicity ranges shown into an equivalent surface brightness. The four white pixels within the polygon in the diagram are pixels discarded from the analysis as they contain the dwarf galaxies And XI, And XII, And XIII, and And XVI.

The equivalent mean surface brightness of the outer halo stars for the full [Fe/H] range given in Figure 35*a* is $\Sigma_V = 33.0 \pm 0.05$ mag arcsec^{-2}, where the uncertainty is calculated using Poisson statistics, assuming no uncertainty in the background subtraction. Note that a 2% error in the subtraction (the average difference of the residuals between the Galactic model and observed Galactic disk found in Fig. 14) will incur a 0.25 mag systematic error. However, the rms scatter in the pixel values in Figure 35 (calculated in counts and then converted into magnitudes) is 1.1 mag; for this calculation, we only took into account those (128) pixels in Figure 35 for which the surface area correction was less than 10%. The fact that this rms scatter is larger than the 0.2 mag random uncertainty expected from Poisson uncertainties in the total measured star counts could be due to an intrinsic lumpiness in the star distribution on the $0.5^\circ \times 0.5^\circ$ scale of the pixels in Figure 35, but we consider it likely that it is largely due to slight variations in observing conditions between fields and slight variations of image quality over the camera. Figure 35*b* gives the map for the metal-poor range $-3.0 < [Fe/H] < -0.7$, which has the advantage of reducing the amount of residual Galactic contamination. The equivalent mean surface brightness for this selection is $\Sigma_V = 33.7 \pm 0.08$ mag arcsec^{-2}. It is pertinent to point out here that the six fields chosen to probe the background all lie within this outer halo region; indeed, they are the fields closest to the outer dashed circle segment marking a projected radius of 150 kpc (see Fig. 16).

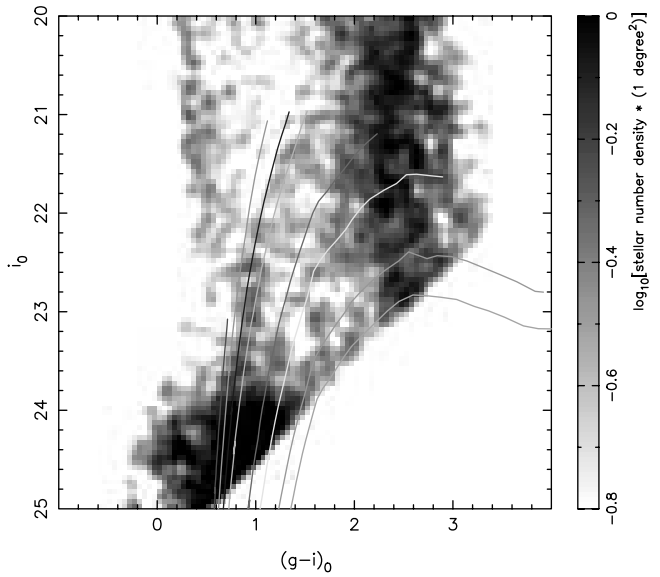

FIG. 36.—Foreground-subtracted Hess diagram of the outer halo region shown in Fig. 35. [*See the electronic edition of the Journal for a color version of this figure*.]

The Hess diagram for the outer halo region is shown in Figure 36, with the foreground subtracted as before. Although noisy, a low-contrast RGB population can be identified that is strongest between the $[\mathrm{Fe/H}] = -1.7$ and -0.7 isochrones. Clearly for $[\mathrm{Fe/H}] > -0.7$, residual foreground subtraction errors dominate the data.

8. HALO PROFILES

Before presenting the radial profiles of the stellar population present in the survey, we first investigate whether our conversion from star counts to equivalent surface brightness (first presented in § 4.1) yields consistent results with previous studies. To this end, we compare our measurements to those of Irwin et al. (2005), who analyzed the profile along the minor axis of M31. We attempted to reproduce as closely as possible the spatial selection chosen by Irwin et al. (2005), a band between $\pm 0.5^\circ$ of the minor axis (see their Fig. 1). The MegaCam survey covers most, but not all, of this area (there is a small gap near $\xi \sim 1.5^\circ$, $\eta \sim -1.5^\circ$, as can be seen in Fig. 22, for example). In Figure 37*a* the black dots mark the surface brightness measurements from integrated light by Irwin et al. (2005), while the upper (blue) histogram shows the MegaCam profile. Although the measurements from integrated light end at $R = 0.5^\circ$, just before the beginning of the MegaCam survey, there is good consistency between these two profiles.

In Figure 37*b* the black dots now show the star count profile of the blue RGB selection of Irwin et al. (2005) converted into an equivalent surface brightness. This *V*-band profile was determined from a color cut in the INT (V, i) system, designed to select metal-poor stars. Here we have chosen not to adopt that approach, relying on interpolation between Padova isochrones. This difference in stellar populations must account for some of the differences between the two profiles. However, the shape of the Irwin et al. (2005) profile at large radius drops rapidly, unlike the MegaCam profile derived from the same region. This effect is due to the foreground subtraction method chosen by Irwin et al. (2005), who selected fields within 4° of M31 to probe and remove the contaminating foreground populations. With hindsight this is clearly not appropriate given that the present MegaCam data show that

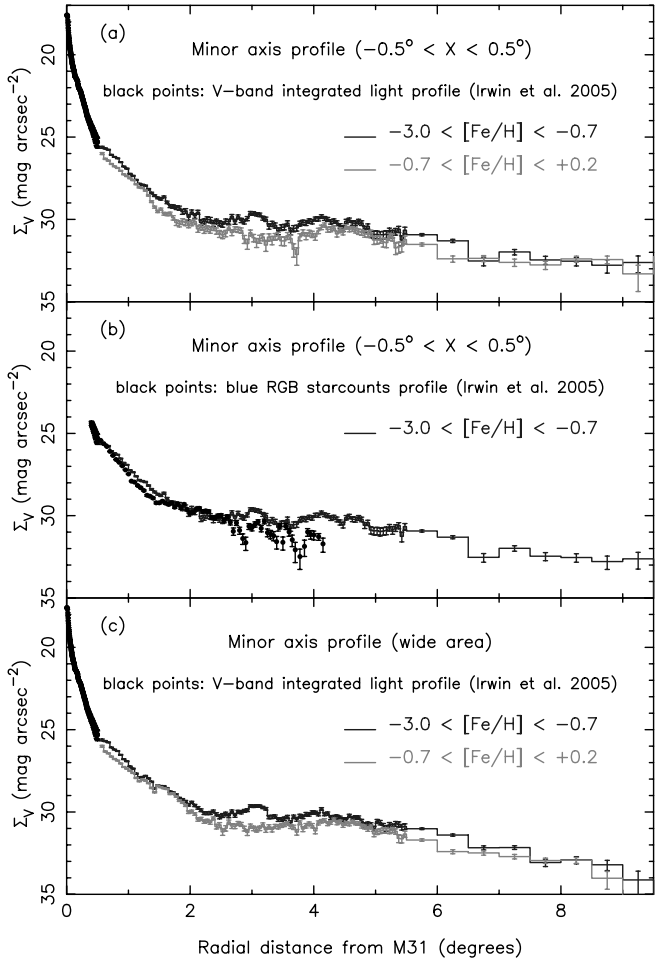

FIG. 37.—(*a*) Comparison of the surface brightness profile from integrated light (*black points*) deduced from the INT survey by Irwin et al. (2005) with the converted star counts derived from the present survey in a $\pm 0.5^\circ$ band around the minor axis of M31. The color variations as a function of radius are attributable to substructures with different stellar populations intersecting this area. The blue RGB star count profile of Irwin et al. (2005) is compared in (*b*) to the metal-poor MegaCam selection in the same spatial region. The differences between these curves at $r < 2.5^\circ$ are likely due to the fact that the two stellar selections, although similar, are not identical. For $r > 2.5^\circ$ the Irwin et al. (2005) profile decreases sharply due to oversubtraction of foreground contaminants in that analysis. (*c*) Similar to (*a*), but the profile is derived over a wider minor-axis area (contained within the yellow polygon of Fig. 22). [*See the electronic edition of the Journal for a color version of this figure*.]

the halo is very extended and has a rather flat profile. However, out to $R \sim 2.5^\circ$ the INT and MegaCam profiles agree very well.

To complement the profiles derived from the narrow 1° band shown in Figures 37*a* and 37*b*, we present in Figure 37*c* the surface brightness profile derived from data over the wider minor-axis area enclosed within the yellow polygon in Figure 22. This is of course less noisy at large radius. The various peaks in the profile correspond to the locations of the streamlike structures discussed above.

Having shown that the minor-axis profile is consistent with previous measurements in the inner regions (for $R < 2.5^\circ$), we now proceed to determine the radial trend of the halo populations over the full survey area. The large amount of substructure detected in the maps above means that the result we find will depend sensitively on what populations we decide to include or reject in the analysis. We therefore adopt a pragmatic approach, taking in turn various population selections, which may be helpful when comparing these data to cosmological simulations.

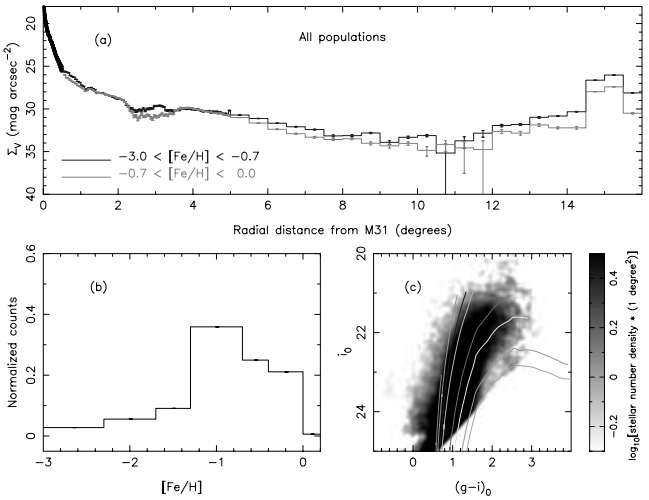

FIG. 38.—(*a*) Radial profile of all the stellar structures present in the MegaCam survey to a limiting magnitude of $i_0 = 23.5$. The points show the *V*-band surface brightness profile from integrated light, as derived by Irwin et al. (2005). The upper and lower (blue and red online) profiles show the MegaCam data for the metal-poor and metal-rich selections, respectively. (*b*) "Metallicity" distribution of this entire region (and down to $i_0 = 23.5$), derived from the stellar color by comparison to 10 Gyr old Padova isochrone models. The corresponding background-subtracted Hess diagram is shown in (*c*). [*See the electronic edition of the Journal for a color version of this figure*.]

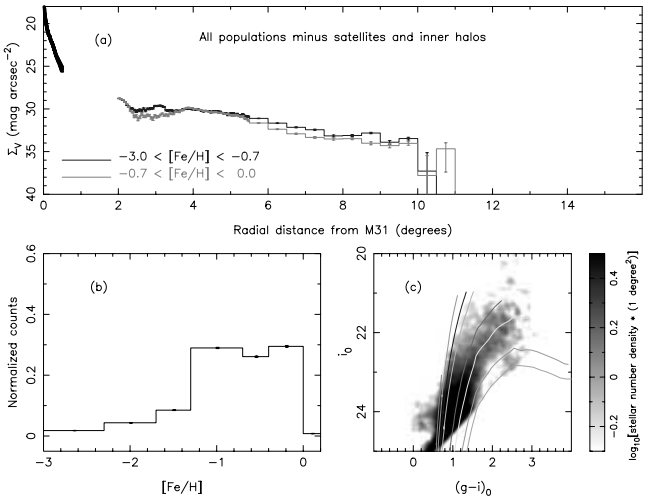

FIG. 39.—Same as Fig. 38, but removing the inner halo of M31 out to $r = 2^\circ$ and that of M33 out to $r = 5^\circ$, as well as all known satellites. For the satellites we excised data within 0.5° of And II and And III, and within 0.2° for the remaining satellites in the MegaCam region. [*See the electronic edition of the Journal for a color version of this figure*.]

We begin by showing the profile of all stellar populations present in the survey down to a limiting magnitude of $i_0 = 23.5$ (Fig. 38*a*). The counts in each radial bin are derived from averaging over the entire azimuthal coverage of the MegaCam survey, with the foreground subtracted using the Besançon model. The *V*-band surface brightness profile measured from the integrated light in the INT data (Irwin et al. 2005) is reproduced here with black dots. The upper profile corresponds to the selection for $-3.0 < [\mathrm{Fe/H}] < -0.7$, while the lower profile corresponds to $-0.7 < [\mathrm{Fe/H}] < 0.0$. As discussed above, we expect the metal-rich selection to be compromised by foreground correction uncertainties, although this is likely only to be an issue at low surface brightness levels where the signal is small.

This sample contains all populations, including satellites and streams, so the profile is not obvious to interpret. However, it transpires that the peak near 4° is due to the presence of the giant stream at that location. The metal-rich nature of that structure enhances the metal-rich profile in the region between $3.5^\circ < R < 6^\circ$, giving the impression that the halo becomes more metal-poor at large radius. This is, however, purely an artifact of the presence of that one stream.

A clear radial decrease is detected in the surface brightness of this combined population up to a distance of about $R \sim 10^\circ$, where it begins to rise again toward M33. Given that M31 and M33 lie at approximately the same heliocentric distance (McConnachie et al. 2005), this is a spectacular demonstration that the stellar halos of the two galaxies actually pass through each other like ghostly bodies.

Figures 38*b* and 38*c* show the MDF and background-subtracted Hess diagram of these stellar populations. In this situation the distributions are overwhelmingly dominated by stars close to M31 and in the disk of M33.

In Figure 39 we repeat this analysis, after removing large areas around the inner halos of the two main galaxies and their known satellites. Clearly the tiny bound satellites found within the MegaCam survey do not have a significant effect on the global surface brightness profile. However, the giant stream does have a large effect, and the MDF and Hess diagram in Figures 39*b* and 39*c* are dominated by that population (compare to Fig. 26a).

Removing the giant stream, in addition to the inner halo and bound satellites, reveals a fascinating profile (Fig. 40). We find a very flat decrease as a function of radius, visually resembling an exponential profile in the loglinear diagram of Figure 40*a*. Moving outward from 2° to 5.5°, the offset between the metal-poor and the metal-rich profile remains approximately constant. These data come primarily from the minor-axis area previously presented in Figure 22 (the region within the yellow polygon). At a radius of $R \sim 5.5^\circ$ the metal-rich population drops significantly and again appears to mimic the metal-poor profile out to $R \sim 7^\circ$. The fact that the metal-poor and metal-rich profiles track each other fairly well in each of these two radial ranges suggests that the mix of stellar populations present does not change considerably over each range. Whether the drop at $R \sim 5.5^\circ$ reflects a real change in stellar populations at this radius (75 kpc) remains to be confirmed.

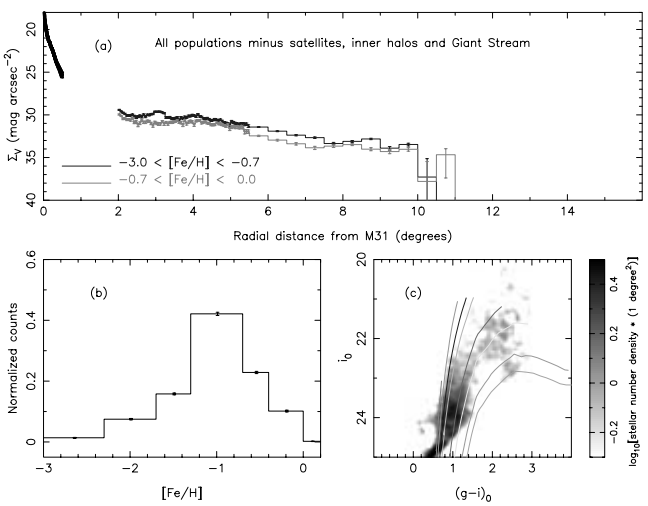

FIG. 40.—Same as Fig. 41, but with the additional removal of the giant stream, as contained within the polygon of Fig. 23. [*See the electronic edition of the Journal for a color version of this figure*.]

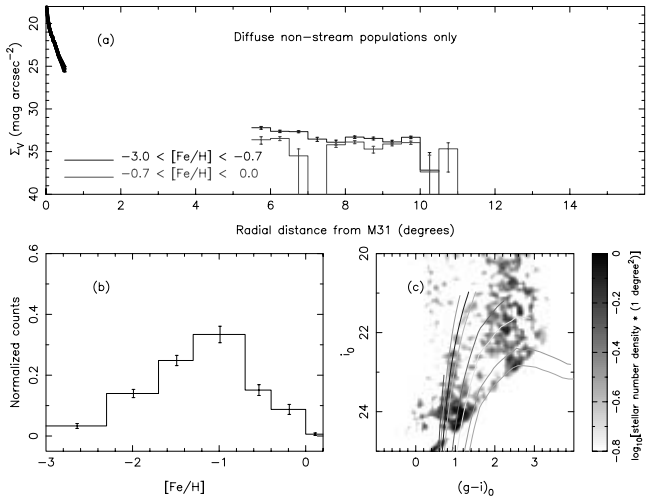

FIG. 41.—Same as Fig. 42, but containing only diffuse stellar populations not identified as streams. [*See the electronic edition of the Journal for a color version of this figure.*]

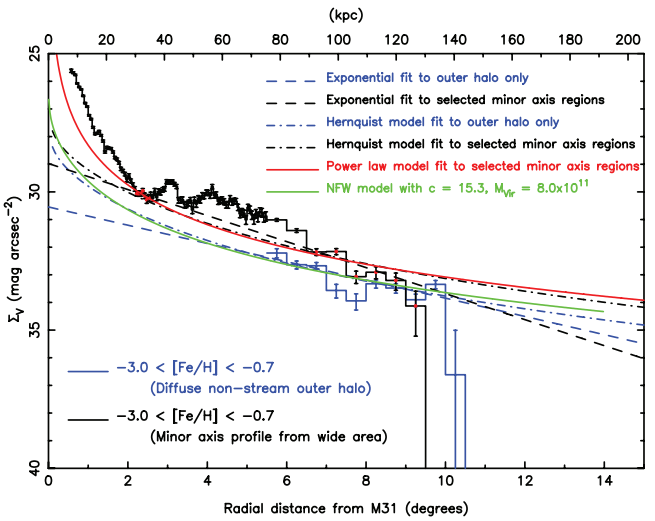

FIG. 42.—Radial profile from the metal-poor selection of the diffuse outer halo (*blue histogram*; previously shown in Fig. 41). The blue dashed line is an exponential fit to these data with $h_R = 45.1 \pm 6.0$ kpc, while the blue dot-dashed line is a Hernquist model with scale length of 53.1 ± 3.5 kpc. The black histogram reproduces the metal-poor minor-axis profile of Fig. 37*c*. We reject the data below $R = 30$ kpc, as the profile is dominated by the inner $R^{1/4}$ de Vaucouleurs profile in this region (Pritchet & van den Bergh 1994; Irwin et al. 2005). As we have shown, between 35 kpc $< R <$ 90 kpc there are copious streamlike substructures on the minor axis, so we reject these regions as well. The best exponential model fit to the remaining data (marked with red points) is shown with a black dashed line and has $h_R = 31.6 \pm 1.0$ kpc. The black dot-dashed line shows the best-fit Hernquist model, which has a scale length of 54.6 ± 1.3 kpc. The red line shows a power-law model fit to these data, which has an exponent of 1.91 ± 0.12. In addition, with the green line, we show the NFW model halo mass profile fitted by Ibata et al. (2004) to the kinematics of the giant stream, with an offset (arbitrarily) chosen to fit the outer halo data. The virial radius of this model is 191 kpc.

Finally, we show in Figure 41 the result of removing all of the identified structures from the survey, leaving only the widely distributed diffuse population behind. For this we have excised the inner halos of M31 and M33, as well as the satellites as detailed previously. We have also removed the areas within the red, green, and blue polygons in Figure 21 and the region contained within the yellow polygon in Figure 22. As can be appreciated from Figure 41*c*, we cannot have much confidence in the metal-rich selection, and correspondingly the metal-rich profile of Figure 41*a* is very uncertain. However, the metal-poor profile appears fairly smooth.

Indeed, the outer halo profile appears remarkably flat in log-linear representation, essentially an exponential function. We fit the data on the radial profile, assuming that, in addition to the Poisson errors in the star counts, there may be a 2% error in the Galactic model and a 2% error in the gradient of the model over the survey region, as suggested by the discussion in § 4.1. The blue dashed line in Figure 42 shows an exponential model fit to the outer halo data (*blue histogram*); we find an extremely long exponential scale length of $h_R = 46.8 \pm 5.6$ kpc. We also show a projected Hernquist model fit (*blue dot-dashed line*) to these data, a model choice motivated by the simulations of Bullock & Johnston (2005); the best model has a scale radius of 53.1 ± 3.5 kpc, more than a factor of 3 larger than predicted by Bullock & Johnston (2005). The black histogram in Figure 42 reproduces the metal-poor minor-axis profile from Figure 37*c*. Recall that this minor-axis selection contains the streamlike structures B, C, and D, so it does not represent the underlying halo. Nevertheless, beyond $R = 6.5^\circ$ there was no obvious substructure in that region of the halo, and we see that the profile from the minor axis agrees reasonably well with that deduced from the outer halo.

For $R > 6.5^\circ$ the minor-axis profile appears slightly higher than the outer halo profile. It is possible that this may reflect the real geometry of the halo; the difference would be consistent with the halo being a slightly prolate structure. We do not favor this interpretation, however. The copious substructures seen at $R < 80$ kpc testify to the dominance of stochastic accretion events in the halo. Given this, its seems more natural to postulate that the variation in the profile that we see here is another consequence of this messy merging process.

If such a thing as a smooth dynamically relaxed halo exists underneath all of the substructure, it cannot have a hole, so the interval 30 kpc $< R <$ 35 kpc is a good place to probe the upper limit to the radial profile in the inner region. We therefore fit models to the data in that region and also at $R > 90$ kpc (the data points used are marked red in Fig. 42). The best-fit exponential model to these minor-axis data (*black dashed line*) has $h_R = 31.6 \pm 1.0$ kpc, while the best-fit projected Hernquist model (*black dot-dashed line*) has a scale radius of 54.6 ± 1.3 kpc. We also fit a power-law model and find that an exponent of 1.91 ± 0.12 is preferred. Thus, we find again a similar slow decline and a long scale length.

This is a very important and rather unexpected result and therefore deserves to be checked carefully. In Figure 43 we have split the outer halo sample into three subsamples (contained within the regions $-7^\circ < \xi < -1^\circ$, $-1^\circ < \xi < 2^\circ$, and $2^\circ < \xi < 7^\circ$); the same slow decline with radius is seen in each subsample, and in the minor-axis sample shown in black, indicating that we are not simply detecting the effects of some localized substructure: approximately 150 kpc separate the red and black profiles! It is possible that the signal arises from an incorrect subtraction of the Galactic contamination. Since the density of stars decreases away from the Galactic plane, which also happens to be the direction away from the center of M31, an insufficient subtraction of the contaminants could leave a residual that decreases with R as observed. Furthermore, the Galactic disk has an exponential profile, which would naturally explain the observed decline. To examine this possibility, we recalculate the surface brightness profiles as before, selecting on metallicity, but this time in addition using a Draconian color-magnitude selection. We limit the data to $i_0 < 22.5$ and retain stars only in the color interval $0.8 < (g-i)_0 < 1.8$. An inspection of Figure 15*b* reveals

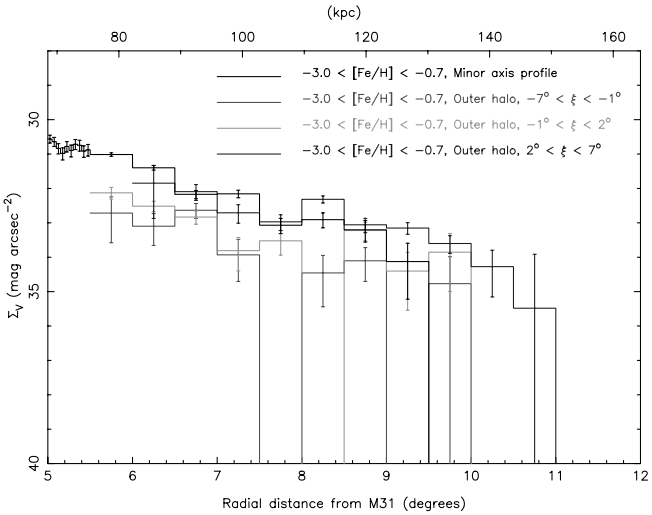

FIG. 43.—Radial surface brightness profile for stars with $-3.0 < [\mathrm{Fe/H}] < -0.7$ for the minor-axis data and for three subsamples of the outer halo region: $-7^\circ < \xi < -1^\circ$, $-1^\circ < \xi < 2^\circ$, and $2^\circ < \xi < 7^\circ$. The similar radial decease indicates that an underlying halo population is present in all these samples, which are separated by up to 150 kpc. [*See the electronic edition of the Journal for a color version of this figure.*]

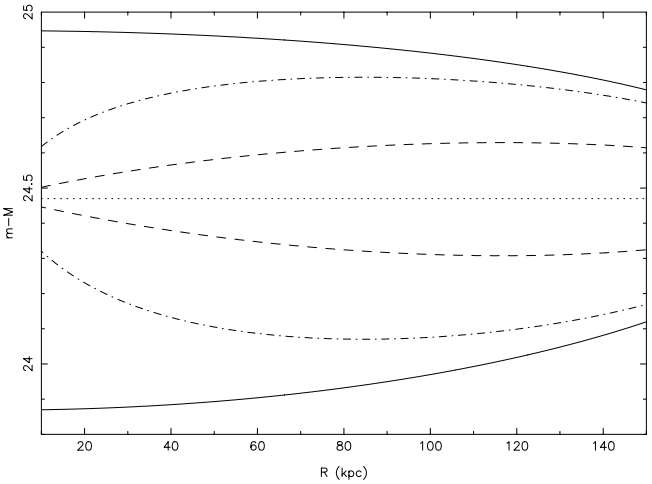

FIG. 45.—Expected spread in distance modulus as a function of projected radius if the underlying halo component falls off as $\rho(r) \propto r^{-2.91}$. The dashed line shows the distance modulus to M31, while the solid line shows the limit of $r = 191$ kpc (the virial radius estimated by Ibata et al. 2004). The dashed and dot-dashed lines mark the region enclosing 50% and 90% of the stars, respectively.

that this selection avoids the bulk of the Galactic disk and halo. The results are shown in Figure 44, and reassuringly they are qualitatively and quantitatively identical to the previous selection with deeper data and the full color interval. The predicted behavior of the Galactic foreground contamination (with this same color-magnitude selection) is also shown in Figure 44 (*turquoise line*). The profile of the contamination is nearly flat in this loglinear representation, so contamination cannot account for the observed profile. Thus, a slow decline with an exceeding long scale length for the outer halo population is a robust result of this survey.

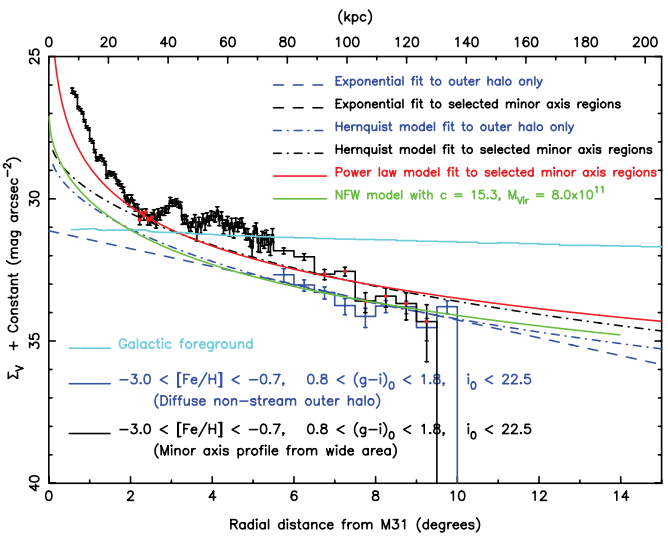

FIG. 44.—Same as Fig. 42, but for stars restricted to the small color-magnitude region $0.8 < (g - i)_0 < 1.8$ and $i_0 < 22.5$, to ensure a minimal contamination from the Galactic halo and disk. Since this selection is for the purpose of verification only, we make no attempt to calibrate the absolute surface brightness values; hence, the ordinate includes an unknown constant. The exponential fit to the outer halo (*blue dashed line*) has $h_R = 47.4 \pm 9.4$ kpc, while the Hernquist fit (*blue dot-dashed line*) has a scale radius of 52.3 ± 4.1 kpc. The black histogram is the metal-poor minor-axis selection, also constrained to the narrow color-magnitude region. The exponential fit to these data (*black dashed line*) has $h_R = 32.7 \pm 1.6$ kpc, while the Hernquist model has a scale radius of 55.6 ± 2.0 kpc. The power-law fit to these same data (*red line*) has an exponent of 1.84 ± 0.16. For comparison, we also show the profile of the Galactic foreground as predicted by the Besançon model (*turquoise line*). The same color-magnitude selection is used as for the observed profiles, although we show here the model prediction over the entire MegaCam survey area (not just the outer halo or minor-axis regions). The model predicts a decrease in the foreground contamination with radial distance over the survey region, but it is essentially flat compared to the observed decrease in the M31 populations.

We have mentioned before, the applicability of the isochrones to estimate metallicity is only justified in regions composed of old stars, so the "metallicity" profiles displayed in Figure 47 must be interpreted with extreme caution. Here we show the trends as a function of elliptical coordinate s for three different CMD bins, as shown. The data interior to $s = 0.5^\circ$ are severely affected by crowding, and we therefore neglect that region. In the region to $0.75^\circ < s < 1^\circ$, the blue selection becomes more pronounced

This slow decline has important consequences on the detectability of halo populations. In particular, one may worry about the distance spread in the halo, whether we are able to detect stars on the far side of M31, and the corresponding spread in the CMD. Assuming a $\rho(r) \propto r^{-2.91}$ profile, we display in Figure 45 the expected spread as a function of projected radius. We see that even with this extended profile, the distance spread should be relatively modest, ~0.5 mag.

9. M33

The southeastern corner of the survey extends out to the Triangulum galaxy, M33. The motivation for this part of the study was to attempt to investigate the interface region between the halos of M33 and M31. Four fields were positioned along the extension of the minor axis of M31, as shown in Figure 46, connecting to the archival data centered on the disk of M33. The map reveals clearly the very regular outer disk of M33, as well as the presence of an extended component out to ~3°, possibly the stellar halo of this galaxy. A more detailed discussion of the structural and stellar population properties of M33 based on a much wider survey conducted with the INT will be presented in a companion paper (A. Ferguson et al. 2008, in preparation).

We adopted the geometry of the model of McConnachie et al. (2006) for the disk of M33, namely, a position angle of 23° and an inclination of 53.8°. The outer dashed ellipse in Figure 46 shows the corresponding elliptical radius $s = 0.75^\circ$, approximately where the disk appears to truncate in this diagram.

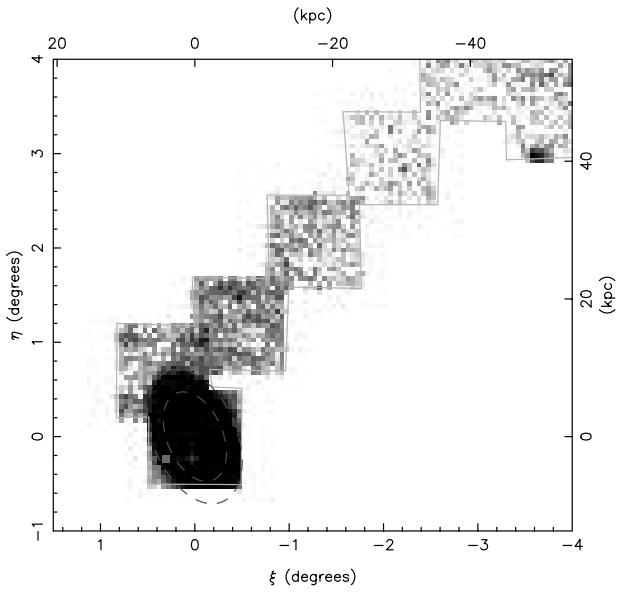

FIG. 46.—Matched filter map (logarithmic representation) to search for structures around M33 constituted of stars with metallicity in the range $-3.0 < [\mathrm{Fe/H}] < 0.0$. A limiting magnitude of $i_0 = 23.5$ was used. The two dashed ellipses mark elliptical radii of $s = 0.5^\circ$ and 0.75° around M33. [*See the electronic edition of the Journal for a color version of this figure.*]

with increasing radius relative to the other two selections, indicating strong radial variations in the stellar populations. The exponential profile of the inner disk ends changes abruptly at $s \sim 0.9^\circ$ into an apparently flat distribution for $1^\circ < s < 2.5^\circ$. Fitting the profiles in the interval $1^\circ < s < 2.5^\circ$ with an exponential function gives exceedingly long scale lengths, or even rising profiles.

The spatial extent of the MegaCam survey around M33 is very limited, so it is impossible to construct a global model for the extended outer component. Thus, it is not clear whether the appropriate geometry for calculating the profiles is spherical or ellipsoidal. If we adopt a spherical coordinate as in Figure 48,

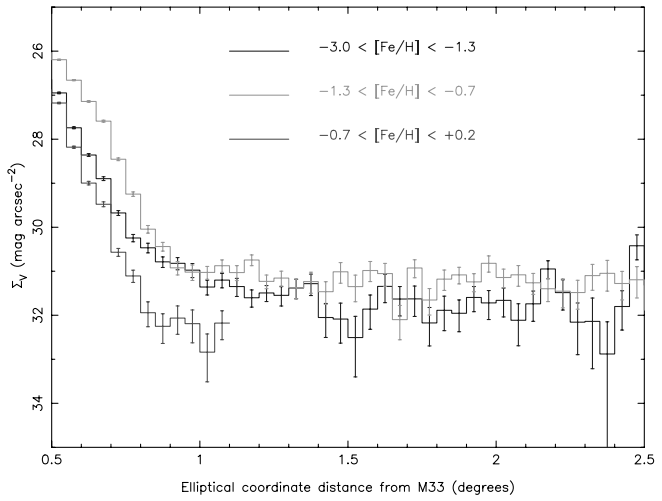

FIG. 47.—Radial profile as a function of elliptical coordinate distance from M33, in three color-magnitude selection regions corresponding to locations between Padova isochrones. We truncate the "metal-rich" profile (which is more heavily affected by Galactic foreground contamination), where the noise begins to dominate. [*See the electronic edition of the Journal for a color version of this figure.*]

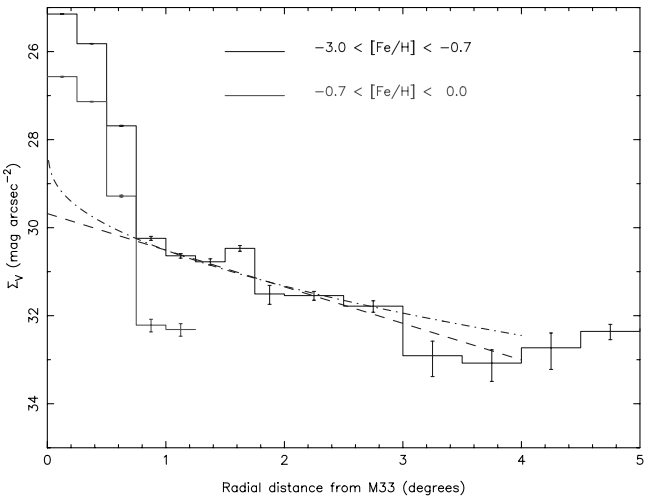

FIG. 48.—Radial light profile in M33 as a function of the radial coordinate r. We display a fitted exponential model with scale length 18 ± 1 kpc and a projected Hernquist model with scale radius 55 ± 2 kpc. [*See the electronic edition of the Journal for a color version of this figure.*]

the profile of the extended component for the selection $-3.0 < [\mathrm{Fe/H}] < -0.7$ seems more reasonable, as it descends monotonically apart from a bump at 1.6°.

Fitting the data between $1^\circ < R < 4^\circ$ (but rejecting the bin at 1.6°) yields a scale length of 18 ± 1 kpc for an exponential model, or alternatively a scale radius of 55 ± 2 kpc for a projected Hernquist model. These scale lengths are surprisingly large, reminiscent of the large values measured above for the outer halo of M31. Curiously, the central surface brightnesses of the extrapolated exponential models are rather similar too. In M33 the model has $\Sigma_V(0) = 29.7 \pm 0.1$, while in M31 the two exponentials fitted in Figure 42 bracket this value with $\Sigma_V(0) = 30.6 \pm 0.3$ and 29.0 ± 0.06 (taking the metallicity selection $-3.0 < [\mathrm{Fe/H}] < -0.7$ for both objects). We stress here that the detection of a halo component around M33 gives further confirmation that the M31 detection is not due to errors in the foreground subtraction, since the foreground contamination profile has the opposite slope as a function of galactic radial distance in the M33 survey fields compared to the M31 fields.

The bump in the surface brightness profile at 1.6° is (just) visible as a faint arc on the map in Figure 46, but we are unsure of the reality of the structure, since it is a very faint feature and only extends over one field. Further imaging is required to determine whether this is a substructure in the halo of M33 or not.

10. DISCUSSION

10.1. *The Underlying Halo*

The analysis presented above in § 8 indicates that underneath the many substructures that we have uncovered in M31 lurks an apparently smooth and extremely extended halo. A similar structure is also detected in M33. By "smooth" what we mean here is not necessarily that the component is perfectly spatially smooth, but instead that any substructures that may be present are below detectability with the current survey. The detectability threshold is a function of radius, but it corresponds to approximately 1 mag arcsec^{-2} brighter than the smooth background over spatial scales $\gtrsim 1$ deg^2.

The existence of a stellar halo component that appears smooth at these surface brightness levels is completely unexpected given recent numerical models that implement recipes for star formation in merging CDM subhalos (Bullock & Johnston 2005; Abadi et al.

2006). Those models predict that the light at large radius is confined to arcs, shells, and streams, with essentially no smoothly distributed stars beyond ~50 kpc in a Milky Way (or M31) analog. The reason for this is that dynamical times at large distances from the galaxy are extremely long, so material has not had anywhere near enough time to mix. The more recent the accretion, in general the more spatially confined the stars should be.

Given these considerations, one would expect a smooth component to be made in the early violent phases of galaxy formation, and since the disk is a fragile structure (Toth & Ostriker 1992), the formation of the structure would have had to have occurred before the formation of the thin disk. This scenario still poses problems, however, since the proto-Andromeda at $z \sim 2$ would have been much less massive than it is today, so the extreme distances of these halo stars, most likely beyond the virial radius of the galaxy at that redshift, are hard to explain.

Interestingly, the radial profile of this smooth halo component in M31 is similar to what is deduced for the Milky Way. As we have reviewed in § 1.2, in the case of the Milky Way, current data probe the halo well up to $r \sim 20$ kpc, we have reasonable constraints up to $r \sim 50$ kpc, but beyond that distance the information is very scanty indeed. However, at least up to $r = 50$ kpc, and given variations from study to study (which are probably due to halo substructures), the density can be approximated by $\rho(r) \propto r^{-3}$. For instance, the study of Siegel et al. (2002), which made use of good distance estimates to halo stars, found $\rho(r) \propto r^{-2.75\pm0.3}$. Similarly, analysis of the RR Lyrae sample of Vivas & Zinn (2006) yielded $\rho(r) \propto r^{-2.7\pm0.1}$ or $\rho(r) \propto r^{-3.1\pm0.1}$, depending on model assumptions of the shape of the halo. This is completely consistent with the present $\Sigma(R) \propto R^{-1.91\pm0.12}$ fit to the minor-axis selection in M31.

In modern galaxy formation simulations stars are formed only within the most massive subhalos that merge to form a galaxy. This is because star formation recipes used in the simulations impose a threshold in gas density below which stars cannot form, basing this condition on observed correlations between Hα emission and gas surface density in galaxy disks (Kennicutt 1989). Furthermore, those satellites that were not massive enough to accrete sufficient gas before the epoch of reionization are expected not to have been able to form stars subsequent to that epoch (Bullock et al. 2000). Dynamical friction acts more strongly on the most massive subhalos, making them fall rapidly into the potential well, where they become disrupted and their contents mixed into the evolving galaxy. Because of this, stars accreted from subhalos are expected to have a more rapidly falling profile than the dark matter, with the light profile falling as r^{-4} or steeper (Bullock & Johnston 2005; Diemand et al. 2005; Abadi et al. 2006). Nevertheless, this prediction does not appear to hold out. If dark matter is distributed according to the "universal" NFW profile (Navarro et al. 1997), the density profile in the outer regions of the halo will be $\rho(r) \propto r^{-3}$, consistent with what we have measured from the stars. This suggests that stars in these tenuous outer reaches of giant galaxies trace the dark matter.

We stress here that the present analysis of M31 is based on a data set that is much more spatially extensive than has been possible for the Milky Way. We have covered substantially more than one-quarter of the halo of M31. In comparison, even the SDSS studies of Yanny et al. (2000), Ivezic et al. (2000), or Chen et al. (2001) covered only 1% of the sky.

Another measure of the halos of these two galaxies that we may now compare is their total luminosity. Integrating the lower of the two exponential profiles shown in Figure 42 out to 140 kpc gives a conservative lower limit to the smooth halo of $L_V \sim 2.2 \times 10^8\ L_\odot$. We estimate an upper limit by integrating the power law up to the virial radius (which we take to be 191 kpc), assuming that the halo density inside 0.5 kpc is constant; this yields a value of $L_V \sim 1.3 \times 10^9\ L_\odot$. For the Milky Way, we estimate the total luminosity by assuming a solar neighborhood V-band luminosity of halo stars of 22,300 $L_\odot$ kpc^{-3} (Morrison 1993); for a density law $\rho(r) \propto r^{-3}$, integration out to 50 kpc gives $L_V \sim 7 \times 10^8\ L_\odot$, or alternatively $L_V \sim 1.2 \times 10^9\ L_\odot$ for $\rho(r) \propto r^{-3.5}$ (following Robin et al. [2003], we also assume that the density of the halo is constant in the inner 0.5 kpc). These estimates for both M31 and the Milky Way are very crude, but taken at face value they indicate that the stellar halo of M31 is very similar in total luminosity to that of the Milky Way. Thus, it appears that previous estimates (e.g., Reitzel et al. 1998) that reported that the halo in M31 is ~10 times denser than that of the Milky Way apply only to the inner regions of the galaxy, where contamination from the large bulge, extended disk, and intervening substructures is clearly a concern.

As reviewed above, Chapman et al. (2006) were able to detect the true inner halo of M31 by observing mostly major-axis fields where halo stars have a very different kinematic signature to other components. At radii between 10 and 70 kpc, the halo component was found to have a mean metallicity of $[\mathrm{Fe/H} \sim -1.4$. This is consistent with the photometric estimate derived for the outer halo component in Figure 41 over the radial range 75 kpc $< R <$ 140 kpc and suggests that the halo has a small or negligible metallicity gradient. This result provides further support for the case of a smooth monolithic halo formed in a single merging event. We note here in passing that H I emission has been detected in this quadrant of M31 (Braun & Thilker 2004), extending all the way to M33 and also possessing a slowly decreasing profile with distance. However, the relation, if any, of this gas to the stellar population discussed here is not clear.

10.2. *Comparison to Kalirai et al.* (*2006b*)

Our discovery of a smooth, very extended halo component covering the entire southern quadrant of Andromeda was anticipated by the kinematic study of Kalirai et al. (2006b). These authors used Keck DEIMOS to survey a number of fields in this region of the sky, targeting known dwarf galaxies, as well as "empty" halo fields. The positions of the fields presented in Kalirai et al. (2006b) are shown with red circles in Figure 49; green squares mark the positions of fields observed with this instrument by our own group (Ibata et al. 2004, 2005; Chapman et al. 2006).

The Kalirai et al. (2006b) fields marked "d2" and "d3," being located on the satellites And II and And III, are not of relevance to the current discussion. But for many of the remaining of their fields our present panoramic survey is invaluable, as it allows one to identify the stellar populations that study actually targeted. In particular, their field "m6" was placed on the edge of stream B, while their fields "a13" and "b15" lie on the extended cocoon of the giant stream. Likewise, in Chapman et al. (2006) we serendipitously targeted streams C and D.

Thus, we see that only fields "m8" and "a19" were targeted in regions where we can be sure that no substructure was present, while field "m11" lies outside of the current survey region. In these fields, Kalirai et al. (2006b) report one probable M31 halo star in m8, four stars in a19, and three stars in m11.

Are these counts consistent with our results? We normalize with respect to the Kalirai et al. (2006b) field "a0" at 30 kpc, where we deduce $\Sigma_V \sim 30$ mag arcsec^{-2}. In that field 67 halo stars were detected in observations over three spectroscopic masks (i.e., three subfields were observed). On the other hand, in their field m11 at 165 kpc, where a mild extrapolation from our survey region

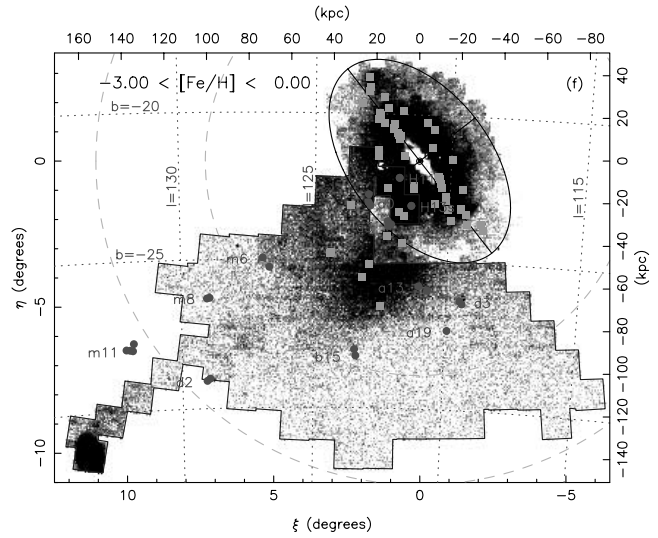

FIG. 49.—Spectroscopically observed fields. Kalirai et al. (2006b) fields are shown with circles, Chapman et al. (2006) fields with squares. Many of these pointings were chosen without knowledge of the underlying populations, so only now is it possible to properly interpret the spectroscopic results. [*See the electronic edition of the Journal for a color version of this figure.*]

gives $\Sigma_V \sim 34$–35 mag arcsec^{-2}, three halo stars were detected using four spectroscopic masks. We therefore expect 40–100 times lower stellar density in m11 compared to a0; that is, we expect zero to two stars to be detected in the four masks observed in field m11 (taking the best-case scenario that all available halo stars were observed and correctly classified). This is then consistent with the sample of three halo stars that were reported by Kalirai et al. (2006b) in field m11. We note, however, that their field lies $\sim 4^\circ$ from M33, where we have found that the halos of M31 and M33 overlap and are approximately of equal surface brightness. Although it is dangerous to draw conclusions from such a minuscule sample, one out of the three halo stars in m11 has a velocity of -150 km s^{-1}, and is highly unlikely to belong to M31, but could be perfectly consistent with being a member of the halo of M33. Likewise, in field m8 we expect 2.5 stars, while in field a19 we expect 2.2 stars, consistent with the number of stars detected spectroscopically.

In summary, despite the very small number of stars in their sample, and despite the probable contamination from M33 in their most distant (and interesting) field, we take the results of Kalirai et al. (2006b) as confirmation that a smooth extended stellar halo is present in M31 out to at least 150 kpc. We note in passing that Kalirai et al. (2006b) estimate the photometric metallicity of their outer halo sample ($R > 60$ kpc) to be $\langle [\mathrm{Fe/H}] \rangle = -1.26 \pm 0.1$. Although this is apparently consistent with the MDF shown in Figure 41, their sample is almost entirely dominated by "contamination" from substructure.

10.3. *Shape of the Smooth Stellar Halo*

As reviewed in § 1.2, most studies of the halo of the Milky Way find that this component is oblate interior to $r \sim 20$ kpc, with flattening $b/a \sim 0.6$. Studies of the halo component in external galaxies, be it from a medianed stack of edge-on spirals (Zibetti et al. 2004) or from an individual edge-on galaxy (Zibetti & Ferguson 2004), find an identical measurement of $b/a \sim 0.6$, within roughly the same radius. The data we have presented on M31 do not allow us to make any statement about the halo flattening in the same volume, and it is very hard to imagine that such a measurement will be possible in the foreseeable future given the difficulty of disentangling bulge, disk, and halo in the inner regions of M31. Previous measurements of the flattening of M31 in this region (e.g., $a/b = 0.55 \pm 0.05$ at 10 kpc; Pritchet & van den Bergh 1994) give an indication of the shape of the total light distribution but do not constrain the shape of the halo.

However, we believe that we have been able to identify the main substructures beyond a distance of $R = 6.5^\circ$, giving a relatively uncontaminated measurement of the density profile beyond that radius. We find, however, that the minor-axis profile is higher than the profile from the broad region we have termed "outer halo," which lies closer to the major axis. This allows us to firmly reject an oblate halo with $b/a \sim 0.6$ at these distances and suggests instead the possibility that the halo is prolate, with $c/a \gtrsim 1.3$. Further data in other quadrants are required to assess the reliability of this estimate. However, in any case, the shape of the outer halo of M31 is manifestly different from that of the inner halos of other galaxies observed to date.

10.4. *Substructures*

Every step we have taken in obtaining a wider view of Andromeda has awarded us with new discoveries in the form of previously unknown substructure. The large area surveyed with MegaCam in the present contribution has continued this trend, showing new dwarf galaxies and several diffuse stellar populations in the form of arcs, streams, or shell segments. These structures testify that accretion and therefore galaxy buildup are still continuing to the present time.

Of the substructures that are present in the survey region, the giant stream is by far the most significant. The data presented in § 6.2 show that the giant stream is a long cigar-shaped structure made up of metal-rich, or young, stars with a metal-poor envelope or cocoon, possibly $\sim 3^\circ$ wide. This lack of homogeneity of the stellar populations in the giant stream indicates that so far the system has not been fully mixed during the course of the tidal disruption process, so it is likely a dynamically very young stream. The requirement that the center and the cocoon remain spatially distinct will likely provide very useful additional constraints for the modeling of the system.

We count up the giant stream stars to $i_0 = 23.5$ and, as before, use And III to normalize the total luminosity. (We caution the reader again that using And III as a reference introduces a large uncertainty into the luminosity estimate.) Integrating within the red polygon shown in Figure 21 (and removing a 0.5° circle around both And I and And III) and subtracting off the expected foreground from the Besançon model, we find $L_V \sim 1.5 \times 10^8\ L_\odot$ ($M_V \sim -15.6$) over this region. This corresponds to approximately one-tenth of the luminosity of M33, and given that the MegaCam region only probes a fraction of the total stream, it is plausible that the progenitor of the giant stream was initially a galaxy of similar luminosity to M33. The width of the stream appears consistent with this possibility, although of course it must have been broadened in the merging process. The core and cocoon dichotomy supports further the analogy with a dwarf disk galaxy like M33. Indeed, the metal-poor cocoon may be the remnant of a vestigial halo. It will be interesting to conduct new simulations in which a small disk galaxy is accreted by M31.

This luminosity of the giant stream, measured from the southern quadrant, is between a factor of 1 and a factor of 10 less luminous than that of the total smooth halo component estimated above. This indicates that the giant stream is a very significant event, probably the largest merging event into the halo that has ever taken place in Andromeda. If merging dwarf galaxies are responsible for contributing globular clusters into halos, one should therefore expect to find a commensurate number of halo globular

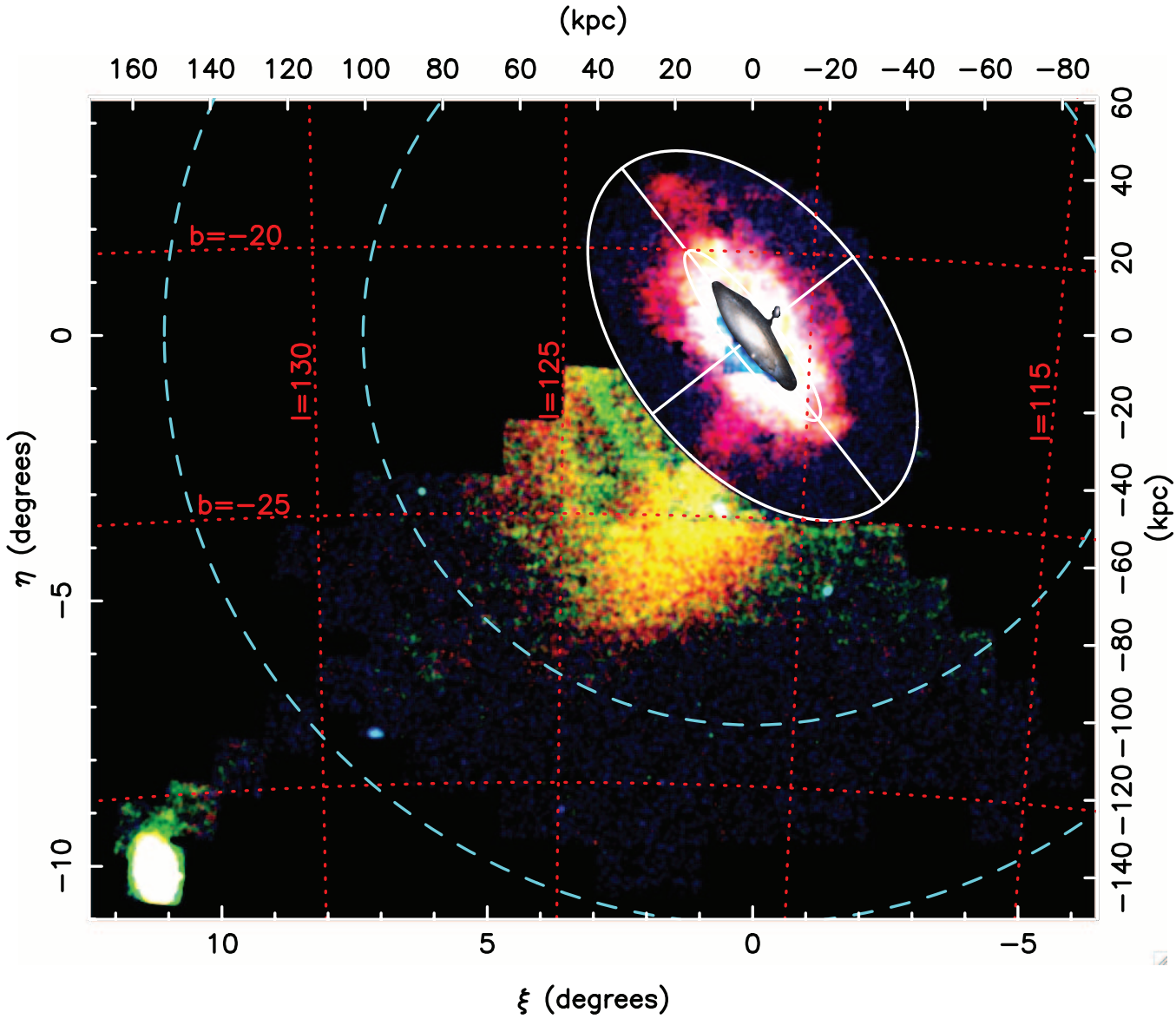

FIG. 50.—Color composite map, in which red, green, and blue show, respectively, stars with $-0.7 < [\mathrm{Fe/H}] < 0.0$, $-1.7 < [\mathrm{Fe/H}] < -0.7$, and $-3.0 < [\mathrm{Fe/H}] < -1.7$. The differences in stellar populations between the giant stream and the several minor-axis streams can be seen as striking differences in color. Within the 4° ellipse we use only the INT data (to render the map easier to interpret) and have chosen a different color representation. In this inner region we again see the presence of many streams and structures that have been discussed in earlier articles by our group. This RGB image, however, shows vividly the differences and similarities in the stellar populations of these structures. In particular, one notices that the color of the giant stream is similar to that of the two "shelves" (at $\xi \sim 2°$, $\eta \sim 0.5°$ and $\xi \sim -1.5°$, $\eta \sim 0.5°$) that appear on this map. Other structures, such as the diffuse northeast structure ($\xi \sim 1.5°$, $\eta \sim 2.5°$) and the G1 clump ($\xi \sim -1.5°$, $\eta \sim -1.7°$), possess a different distribution of stellar populations. At the center of the galaxy we have added to scale an image of the central regions of M31 constructed from Palomar sky survey plates.

clusters with kinematics compatible with the giant stream and its extension.

In Figure 50 we present an RGB image of the survey region, in which the red, green, and blue channels contain, respectively, the matched filter maps for metal-rich ($-0.7 < [\mathrm{Fe/H}] < 0.0$), intermediate ($-1.7 < [\mathrm{Fe/H}] < -0.7$), and metal-poor ($-3.0 < [\mathrm{Fe/H}] < -1.7$) stars. This image shows the striking differences in stellar populations of the halo substructures we have identified in this survey. Even though the giant stream remains the most significant accretion, many more smaller systems are being accreted. M31 is evidently still leading a colorful life assimilating its small neighbors.

We see also that halo formation is evidently a stochastic process. The halo profile and detailed properties of the halo can therefore be expected to differ from galaxy to galaxy depending on the amount of substructure and merging debris that is present. This makes it all the more surprising that the profile of the smooth halo discussed above resembles well that of the Milky Way, suggesting that the reason for this is an underlying similarity in the mass distributions, which is independent of the detailed assembly history.

10.5. *The Inner Minor Axis*

The several streams detected on the minor axis from ~6.5° all the way into the edge of the disk are particularly important in that they shed light on the numerous previous studies (reviewed in § 1) made in this region because it has been considered "clean halo" for many years. Indeed, it is not obvious that there exists a region of clean halo in the inner galaxy, as one can appreciate from an inspection of Figure 50. The variations in stellar populations are

apparent as color differences, and one can readily see that the G1 clump and northeast structure have a different distribution of stellar populations than the giant stream and the two "shelves" to the east and west (the figure caption states their location). The contours in Figure 19 show the isoluminosity surfaces derived from star counts for stars with $-3.0 < [\mathrm{Fe/H}] < 0.0$, with contour separation of 1 mag arcsec^{-2} (the levels correspond approximately to $\Sigma_V = 27$, 28, and 29 mag arcsec^{-2}). It is immediately apparent from this diagram that at a projected radius from $R \sim 10$ to $\sim$20 kpc on the minor axis, the dominant component is a large irregular ellipsoidal structure whose major-axis size extends out to $R \sim 40$ kpc. We have shown previously from kinematics in many fields around the galaxy that this is an extended rotating disk–like component (Ibata et al. 2005). Thus, although the surface brightness profile on the minor axis follows approximately an $R^{1/4}$ law out to 1.4°, or 19 kpc (Pritchet & van den Bergh 1994; Irwin et al. 2005), it is unlikely that the bulge itself extends out to those radii. Indeed, the bulge in near-infrared wavelengths is a relatively compact structure that dominates out to $\sim$2.6 kpc on the *major axis* (Beaton et al. 2007). It is therefore pertinent in the current context to review the evidence for the $R^{1/4}$ law profile. In Figure 51 we reproduce the *V*-band minor-axis profile from Irwin et al. (2005); in the interval 8 kpc $< R <$ 18 kpc the light profile is actually remarkably similar to an exponential function with a scale length of 3.22 kpc. We stress that this exponential behavior is not confined to the minor-axis data alone: it is present with the same density profile (and normalization) at all azimuth angles (see Fig. 3 of Ibata et al. 2005). In contrast, the de Vaucouleurs profile of Pritchet & van den Bergh (1994), shown in Figure 51*b*, overpredicts the counts in the radial range $1° < R < 1.5°$.

The "extended disk" component was found to have an intrinsic scale length of 6.6 ± 0.4 kpc (Ibata et al. 2005) and to follow an exponential profile out to $\sim$40 kpc (after which the profile flattens out). For the minor-axis scale length of 3.22 kpc to be consistent with that intrinsic scale length, the inclination of the outer disk would have to be 60.8°, very close to the value of 64.7° estimated by Ibata et al. (2005). Furthermore, the intrinsic break at 40 kpc (deprojected) would correspond to 1.4° on the minor axis, exactly where it is seen.

If one wishes to adhere to the previously held assumption that the minor axis is dominated out to $R \sim 20$ kpc by an immense $R^{1/4}$ law "bulge" or "spheroid," it requires a considerable stretch of credibility. It means that this spheroid has to be substantially flattened to be consistent with the contours of Figure 19; the spheroid must have an exponential-like profile between (deprojected) radii of 15 kpc $\lesssim R \lesssim$ 40 kpc at all azimuth angles; and it must be rotationally supported, but with a rotation rate almost as fast as that of the H I disk. We therefore judge that the extended disk picture is a far more likely and less contrived model. This confirms the visual impression of Figure 50: in the distance range 10 kpc $\lesssim R \lesssim$ 15 kpc the minor-axis profile is dominated by a disklike population, with only minor contribution from the bulge or spheroid.

Since we now understand the kinematic and chemical behavior of the extended disk from observations close to the major axis (where stars of different components may be more easily distinguished by their differences in kinematics), we can use these insights to interpret the radial variation in the properties of the stellar populations on the minor axis. Interior to $\sim$0.2° on the minor axis the dominant population will clearly be the bulge; farther out between $0.2° < R < 0.4°$, the normal disk contributes in a non-negligible fashion to the profile, as noted by Irwin et al. (2005); then from $0.5° < R < 1.3°$ the extended disk component becomes dominant; finally, beyond 1.5° the underlying smooth halo becomes important, although spatially confined streams dominate at various locations.

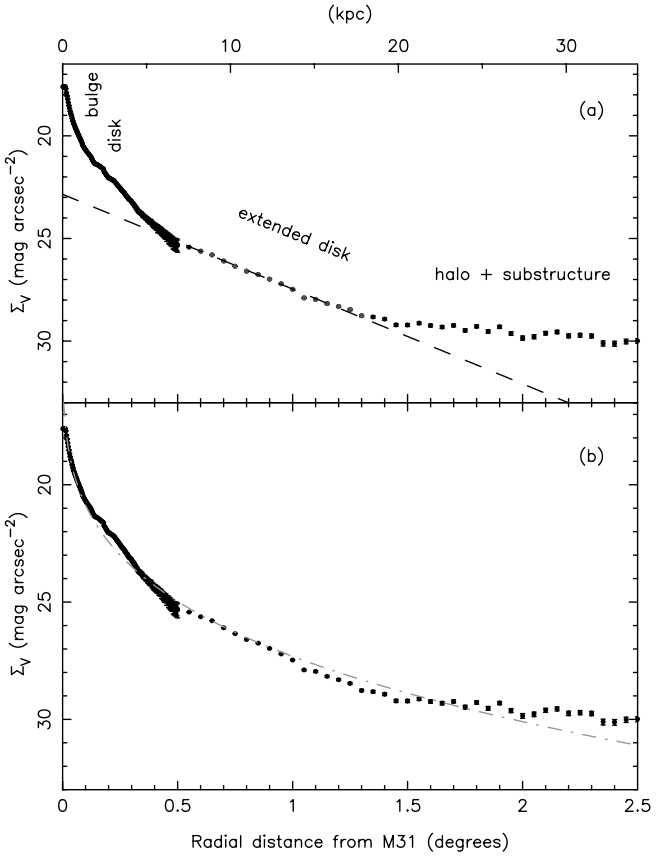

FIG. 51.—Black points in both panels reproduce the *V*-band minor-axis surface brightness profile from Irwin et al. (2005). The radial interval 8 kpc $< R <$ 18 kpc (marked with gray points in [*a*]) is clearly almost straight in this loglinear representation. Fitting the data in this region with an exponential function (*dashed line*) yields a scale length of 3.22 ± 0.02 kpc (where the uncertainty is the formal error on the fit). We also indicate the regions where the various components are dominant. Recent analysis of the 2MASS 6X imaging data of M31 shows a high-contrast bulge that dominates the near-infrared light out to $\sim$2.6 kpc on the major axis (Beaton et al. 2007). The bumps in the disk-dominated region (at projected radii between 2 kpc $\lesssim R \lesssim$ 6 kpc on the minor axis) are due to spiral arms and the star-forming ring. The dashed line in (*b*) shows a de Vaucouleurs model fit using an effective radius of $R_e = 0.1°$ as found by Pritchet & van den Bergh (1994) equivalent to 1.4 kpc (Irwin et al. 2005), which overestimates the star counts between $1° < R < 1.5°$. [*See the electronic edition of the Journal for a color version of this figure.*]

Consequently, one should also expect strong radial variations in metallicity and kinematics. The kinematics on the minor axis in particular will be complex and difficult to disentangle, since all populations have the same mean velocity and their velocity distributions overlap. Going out from the center one should therefore expect to find the bulge, with high metallicity and high velocity dispersion; then in the bulge plus disk region, a wide metallicity range, but a narrower velocity dispersion; then with the addition of the extended disk, the mean metallicity should decrease toward $[\mathrm{Fe/H}] \sim -0.9 \pm 0.2$, and the velocity distribution should contain a significant fraction of stars in a peak with dispersion in the range 20–50 km s^{-1} (Ibata et al. 2005); then the halo component should appear with $[\mathrm{Fe/H}] \sim -1.4$ and with a large velocity dispersion of $\sigma_v \sim 140$ km s^{-1} at $R = 20$ kpc, decreasing outward (Chapman et al. 2006). In addition to these smooth structures, one will find the multiple streams detected (and not yet detected!) in this area, which as we have shown can have quite different stellar populations, but which are likely to be dominated by the metal-rich giant stream. The velocity distribution

of these streams in a small field will in general be a narrow velocity spike of dispersion $\sim$10 km s^{-1}. However, we stress that the minor axis is a very complex region interior to $\sim$30 kpc, with a complex mix of many stellar populations, each component overlapping considerably with the others in terms of radial velocity, metallicity, spatial location, color-magnitude structure, etc.

This finding that the minor-axis region between 8 kpc $\lesssim R \lesssim$ 20 kpc is dominated by the extended disk, and not bulge, halo, or spheroid, as has been assumed in numerous earlier articles, goes a long way toward clarifying the diverse and confusing results that have been deduced from observations in this region. In particular, it helps interpret the findings of Brown et al. (2003, 2006a, 2006b, 2007). These authors obtained ultradeep *HST* ACS photometry in two minor-axis fields, a giant stream field, and a field at the edge of the northeast disk, in order to determine ages of the underlying populations via main-sequence turnoff fitting (field locations are shown with squares in Fig. 19). Their two minor-axis fields lie at projected radii of $R = 11$ and 21 kpc. Due to the reasons detailed above, their spheroid field at $R = 11$ kpc probes a location that is dominated by the extended disk population. From their photometry in this region they deduce a best-fitting stellar population model that has $\langle$[Fe/H]$\rangle = -0.6$ and $\langle$age$\rangle = 9.7$ Gyr. Brown et al. (2006a) dismiss the possibility that the field is related to the extended disk partly on the grounds that the field lies at a deprojected distance of 51 kpc, yet any small warping of the plane of the galaxy, such as we deduced in Ibata et al. (2004), invalidates this argument. The remaining argument is the velocity dispersion measurement of $\sim$80 km s^{-1}, which appears high for the extended disk ($\sigma_v \lesssim 50$ km s^{-1}), until one considers the mix of components that must be present at this location.

Farther out on the minor axis at $R \sim 20$ kpc one can discern a diffuse component that appears of the same red hue as the giant stream with this color representation. This is clearly a metal-rich region, and possibly related to the extension of the "northeast shelf" of Ferguson et al. (2002), itself the likely continuation of the orbit of the giant stream (Ibata et al. 2004). Indeed, Ferguson et al. (2005) showed that the giant stream and northeast shelf are connected on the basis of near identical stellar populations to 3 mag below the horizontal branch. With hindsight it is therefore not surprising that the $R = 21$ kpc field of Brown et al. (2006a) contains intermediate-age stars, although it should be noted that the mean age of the stars in this field is $\sim$2 Gyr older than in their giant stream field (which is itself on the outskirts of the extended disk region). Figure 50 also suggests that their northeast disk field is also a complex mixture of disk, extended disk, and possibly metal-rich debris from the giant stream.

We note also in passing that the geometry of the minor-axis populations has important consequences for microlensing studies in M31 (e.g., Calchi Novati et al. 2005). With most of the stellar populations previously assumed to lie in the spheroid, being confined primarily in a disk, we predict a much lower self-lensing rate.

10.6. *Kinematics of Substructures*

The above discussion also clarifies some previous claims for the existence of kinematic substructure around M31. In a field at $R = 19$ kpc, Reitzel & Guhathakurta (2002) find four metal-rich stars in their sample with similar radial velocity of approximately -340 km s^{-1}, which they interpreted as evidence for accretion debris. This position lies within the diffuse region that has stellar populations similar to the giant stream (Fig. 50), so the kinematic substructure in the Reitzel & Guhathakurta (2002) sample is likely related to that structure.

Further kinematic substructure in this region was found by Kalirai et al. (2006a), who in studying the kinematics of the giant stream find a secondary kinematic peak $R = 20$ kpc with $\overline{v} = -417$ km s^{-1} and $\sigma_v \approx 16$ km s^{-1}. The location of this field (H13s) lies at $\xi = 0.29^\circ$, $\eta = -1.53^\circ$, clearly within the ellipsoidal structure (Fig. 50), and furthermore the expected mean velocity of the extended disk model of Ibata et al. (2005) predicts $v = -381 \pm 22$ km s^{-1} in this field. The velocity dispersion of the cold component is also similar to what has been found in certain regions of the extended disk (e.g., 17 km s^{-1} in field F3 of Ibata et al. 2005). We speculate therefore that the cold kinematic structure in field H13s is clumpy structure of the edge of the extended disk.

Most recently Gilbert et al. (2007) have presented a kinematic survey of several fields along the minor axis of M31. They detect kinematic substructure in three fields, with dispersions of $55.5^{+15.6}_{-12.7}$ km s^{-1} ($R = 12$ kpc), $51.2^{+24.4}_{-15.0}$ km s^{-1} ($R = 13$ kpc), and $10.6^{+6.9}_{-5.0}$ km s^{-1} ($R = 18$ kpc). It is probable that the two structures of velocity dispersion $\sim$50 km s^{-1} are also related to the extended disk component. The large deprojected distances they deduce along the minor axis (51–83 kpc) are acutely dependent on the assumption of constant inclination of the disk, which as we have shown is not supported by the data (Ibata et al. 2005). In particular, the $R = 12$ and 13 kpc fields of Gilbert et al. (2007) lie in the distance regime where the extended disk is dominant in Figure 51. The cold kinematic component observed in their $R = 18$ kpc field is likely related to the giant stream for the same reason as is the cold kinematic structure in the Reitzel & Guhathakurta (2002) sample.

11. CONCLUSIONS

This article has presented a deep panoramic view of the Andromeda galaxy and part of the Triangulum galaxy. Although it is not the deepest external galaxy survey ever undertaken, nor the most extended, we have for the first time covered a substantial fraction of a galaxy out to a substantial fraction of the virial radius to sufficient depth to detect several magnitudes of the RGB and with sufficient photometric accuracy to estimate stellar metallicity. To our knowledge this is the first deep wide-field view of the outermost regions of galaxies.

The new CFHT data presented here are combined with an earlier survey of the inner regions of M31 ($s \lesssim 55$ kpc) taken with the INT (Ibata et al. 2001a; Ferguson et al. 2002; Irwin et al. 2005). We summarize below the main findings from these surveys:

1. A huge amount of confusion in the literature has arisen from assuming that the minor-axis region between projected radii of $0.5^\circ < R < 1.3^\circ$ (7 kpc $< R <$ 18 kpc) is representative of the spheroid. We have shown here that it is not. Instead, it is likely to be a complex mix of stellar populations, dominated over much of this radial range by the extended disk. Many of the previous claims that the spheroid or stellar halo of M31 is very different from that of the Milky Way were based on a comparison of the properties of genuine Milky Way halo stars to those of stars in M31 in quite different components.

2. Beyond the inner ($\sim$20 kpc) disk, Andromeda contains a multitude of streams, arcs, shells, and other irregular structures. Some of these structures appear to be related (they have a similar mix of stellar populations), while others are manifestly due to separate accretion events.

3. The largest of these structures, the giant stream, is very luminous, possessing $L_V \sim 1.5 \times 10^8\ L_\odot$ over the region surveyed with MegaCam. This body dominates the luminosity budget of the inner halo and, once it becomes fully mixed, may double the

luminosity of the smooth underlying halo. This ongoing accretion event must be among the most significant the halo has suffered since its initial formation.

4. Ignoring regions with obvious substructure, we find that the remaining area of the survey exhibits a smooth metal-poor stellar halo component. This structure need not be perfectly spatially smooth, but the intrinsic inhomogeneities are below the sensitivity of this study. The smooth halo is vast, extending out to the radial limit of the survey, at 150 kpc. The profile of this component can be modeled with a Hernquist profile as suggested by simulations, but the resulting scale radius of $\sim$55 kpc is almost a factor of 4 larger than modern halo formation simulations predict. A power-law profile with $\Sigma(R) \propto R^{-1.91\pm0.12}$ [i.e., $\rho(r) \propto r^{-2.91\pm0.12}$] can also be fitted to the data. Simulations predicted a sharp decline in the power-law exponent beyond the central regions of the galaxy to $\rho(r) \propto r^{-4}$ or $\rho(r) \propto r^{-5}$. This is not observed. Instead, and unexpectedly, the stellar profile mirrors closely the expected profile of the dark matter.

5. Since dynamically young accretion events give rise to arcs and streams, and because dynamical times are very long in the outer reaches of the halo, the smoothness of the component over huge areas of the outskirts of the galaxy suggests that the component is very old. It therefore seems plausible that the structure was formed in a cataclysmic merging event early in the history of the galaxy, probably before the formation of the fragile disk.

6. The outer halo of M31 ($R \gtrsim 80$ kpc) is not oblate. On the contrary, the stellar distribution appears to be slightly prolate with $c/a \gtrsim 1.3$, although we judge that a reliable measurement of this parameter will require further data in other quadrants.

7. Both the density profile of the smooth halo in M31 and its total luminosity ($\sim 10^9\ L_\odot$) are very similar to the Milky Way. Their metallicity and kinematic properties also resemble each other closely (Chapman et al. 2006; Kalirai et al. 2006a). This is somewhat surprising if halo formation is a stochastic process as suggested by simulations (see, e.g., the discussion in Renda et al. 2005).

8. Lumping all stellar populations together, we detect a stellar population gradient in the survey such that the more metal-rich populations are more centrally concentrated, consistent with the predictions of Bullock & Johnston (2005). However, this is almost entirely due to the presence of the metal-rich giant stream "contaminating" the inner halo.

9. An extended slowly decreasing halo is also detected around M33. Fitting this distribution with a Hernquist model gives a scale radius of $\sim$55 kpc, essentially identical to that of M31, although we caution that the poor azimuthal coverage of the survey around M33 makes this result sensitive to unidentified substructures and to assumptions about the geometry of the halo. Indeed, given the lack of a full panoramic study, it is not possible to rule out the possibility that the detected population is a halo substructure.

10. The stellar halos of M31 and M33 touch in projection and are probably passing through each other. The kinematics of stars in this overlap region will be fascinating to analyze, although large samples will probably be needed to disentangle the structures.

11. Two new dwarf satellite galaxies of M31, And XV, and And XVI are presented, which, together with those reported in a previous contribution (Martin et al. 2006), brings the number of new satellites detected in the MegaCam survey region up to five. Follow-up studies are currently underway to understand the nature of these objects and those of lower signal-to-noise ratio satellite candidates found in the survey.

Many questions remain open. What is the radial dependence of the metallicity and stellar populations in the smooth component? Is there a discontinuity in properties between the inner halo and the outer halo similar to the simulations of Abadi et al. (2003, 2006), reflecting native and immigrant stars?

It will be very interesting to extend the survey out to the virial radius of the Galaxy and verify whether the correlation between the observed stellar profile and the expected dark matter surface density continues to that radius. Further photometric coverage to the east of the minor axis will also be helpful to study fully the morphology and extent of the streamlike structures detected from $R = 30$ to $\sim$120 kpc and to determine whether these objects are indeed streams, and thus make plausible judgments about their origin and evolution and compare them to theoretical predictions of the formation of the outer halo.

This panorama of the outer fringes of Andromeda and Triangulum has shown that halos are truly misnamed: they are in reality dark galactic graveyards, full of the ghosts of galaxies dismembered in violent clashes long ago. Other, even more ancient remnants have lost all memory of their original form, and in filling these haunted halos with the faintest shadow of their former brilliance, they follow faithfully the dark forces to which they first succumbed. The true nature of this most somber of galactic recesses is finally beginning to be revealed.

This study would not have been possible without the excellent support of staff at the CFHT and the careful and meticulous observations performed in queue mode. R. I. wishes to thank Annie Robin for allowing us privileged access to the Besançon model via UNIX scripts, which greatly facilitated the construction of the foreground model, and also many thanks to Michele Bellazzini for helpful comments on this work. A. M. N. F. is supported by a Marie Curie Excellence Grant from the European Commission under contract MCEXT-CT-2005-025869.

REFERENCES

Abadi, M., Navarro, J., & Steinmetz, M. 2006, MNRAS, 365, 747
Abadi, M., Navarro, J., Steinmetz, M., & Eke, V. 2003, ApJ, 597, 21
Avila-Reese, V., Firmani, C., & Hernández, X. 2002, in New Quests in Stellar Astrophysics: The Link between Stars and Cosmology, ed. M. Chavez et al. (Dordrecht: Kluwer), 83
Beaton, R., et al. 2007, ApJ, 658, L91
Beaulieu, J.-P., Buchler, R., Marquette, J.-B., Hartman, J., & Schwarzenberg-Czerny, A. 2006, ApJ, 653, L101
Bellazzini, M., Cacciari, C., Fedeici, L., Fusi Pecci, F., & Rich, M. 2003, A&A, 405, 867
Bellazzini, M., Ferraro, F., & Pancino, E. 2001, ApJ, 556, 635
Belokurov, V., et al. 2007, ApJ, 654, 897
Bergbusch, P., & Vandenberg, D. 2001, ApJ, 556, 635
Braun, R., & Thilker, D. 2004, A&A, 417, 421
Brown, T., Ferguson, H., Smith, E., Kimble, R., Sweigart, A., Renzini, A., Rich, M., & VandenBerg, D. A. 2003, ApJ, 592, L17
Brown, T., Smith, E., Ferguson, H., Rich, R., Guhathakurta, P., Renzini, A., Sweigart, A., & Kimble, R. 2006a, ApJ, 652, 323
Brown, T., Smith, E., Guhathakurta, P., Rich, R., Ferguson, H., Renzini, A., Sweigart, A., & Kimble, R. 2006b, ApJ, 636, L89
Brown, T., et al. 2007, ApJ, 658, L95
Bullock, J., & Johnston, K. 2005, ApJ, 635, 931
Bullock, J., Kravtsov, A., & Weinberg, D. 2000, ApJ, 539, 517
———. 2001, ApJ, 548, 33
Calchi Novati, S., et al. 2005, A&A, 443, 911
Chandar, R., Bianchi, L., Ford, H., & Sarajedini, A. 2002, ApJ, 564, 712
Chapman, S., Ibata, R., Lewis, G., Ferguson, A., Irwin, M., McConnachie, A., & Tanvir, N. 2006, ApJ, 653, 255

Chen, B., et al. 2001, ApJ, 553, 184
Chiba, M., & Beers, T. 2000, AJ, 119, 2843
Clewley, L., Warren, S., Hewett, P., Norris, J., Wilkinson, M., & Evans, N. 2005, MNRAS, 362, 349
Diemand, J., Madau, P., & Moore, B. 2005, MNRAS, 364, 367
Durrell, P., Harris, W., & Pritchet, C. 2001, AJ, 121, 2557
———. 2004, AJ, 128, 260
Evans, N., Wilkinson, M., Guhathakurta, P., Grebel, E., & Vogt, S. 2000, ApJ, 540, L9
Fardal, M., Guhathakurta, P., Babul, A., & McConnachie, A. 2007, MNRAS, 380, 15
Faria, D., Johnson, R., Ferguson, A., Irwin, M., Ibata, R., Johnston, K., Lewis, G., & Tanvir, N. 2007, AJ, 133, 1275
Ferguson, A., Irwin, M., Ibata, R., Lewis, G., & Tanvir, N. 2002, AJ, 124, 1452
Ferguson, A., Johnson, R., Faria, D., Irwin, M., Ibata, R., Johnston, K., Lewis, G., & Tanvir, N. 2005, ApJ, 622, L109
Font, A., Johnston, K., Guhathakurta, P., Majewski, S., & Rich, M. 2006, AJ, 131, 1436
Freeman, K., & Bland-Hawthorn, J. 2002, ARA&A, 40, 487
Gilbert, K., et al. 2006, ApJ, 652, 1188
———. 2007, ApJ, in press (astro-ph/0703029)
Girardi, L., Grebel, E., Odenkirchen, M., & Chiosi, C. 2004, A&A, 422, 205
Guhathakurta, P., et al. 2006, AJ, 131, 2497
Hammer, F., Puech, M., Chemin, L., Flores, H., & Lehnert, M. 2007, ApJ, 662, 322
Hartman, J., Bersier, D., Stanek, K., Beaulieu, J.-P., Kaluzny, J., Marquette, J.-B., Stetson, P., & Schwarzenberg-Czerny, A. 2006, MNRAS, 371, 1405
Huxor, A. Tanvir, N., Irwin, M., Ibata, R., Collett, J., Ferguson, A., Bridges, T., & Lewis, G. 2005, MNRAS, 360, 1007
Ibata, R., Chapman, S., Ferguson, A., Irwin, M., & Lewis, G. 2004, MNRAS, 351, 117
Ibata, R., Chapman, S., Ferguson, A., Lewis, G., Irwin, M., & Tanvir, N. 2005, ApJ, 634, 287
Ibata, R., Irwin, M., Lewis, G., Ferguson, A., & Tanvir, N. 2001a, Nature, 412, 49
Ibata, R., Irwin, M., Lewis, G., & Stolte, A. 2001b, ApJ, 547, L133
Ibata, R., Lewis, G., Irwin, M., Totten, E., & Quinn, T. 2001c, ApJ, 551, 294
Irwin, M., Ferguson, A., Ibata, R., Lewis, G., & Tanvir, N. 2005, ApJ, 628, L105
Irwin, M., & Hatzidimitriou, D. 1995, MNRAS, 277, 1354
Irwin, M., & Lewis, J. 2001, NewA Rev., 45, 105
Ivezic, Z., et al. 2000, AJ, 120, 963
Johnston, K. V., Hernquist, L., & Bolte, M. 1996, ApJ, 465, 278
Kalirai, J., Guhathakurta, P., Gilbert, K., Reitzel, D., Majewski, S., Rich, M., & Cooper, M. 2006a, ApJ, 641, 268
Kalirai, J., et al. 2006b, ApJ, 648, 389
Kennicutt, R. 1989, ApJ, 344, 685
King, I. 1962, AJ, 67, 471
Klypin, A., Kravtsov, A., Valenzuela, O., & Prada, F. 1999, ApJ, 522, 82
Loeb, A., Reid, M., Brunthaler, A., & Falcke, H. 2005, ApJ, 633, 894
Mackey, A., et al. 2006, ApJ, 653, L105
———. 2007, ApJ, 655, L85
Martin, N., Ibata, R., & Irwin, M. 2007, ApJ, submitted (astro-ph/0703506)
Martin, N., Ibata, R., Irwin, M., Chapman, S., Lewis, G., Ferguson, A., Tanvir, N., & McConnachie, A. 2006, MNRAS, 371, 1983
McConnachie, A., Chapman, C., Ibata, R., Ferguson, A., Irwin, M., Lewis, G., Tanvir, N., & Martin, N. 2006, ApJ, 647, L25
McConnachie, A., & Irwin, M. 2006, MNRAS, 365, 1263
McConnachie, A., Irwin, M., Ferguson, A., Ibata, R., Lewis, G., & Tanvir, N. 2004a, MNRAS, 350, 243
———. 2005, MNRAS, 356, 979
McConnachie, A., Irwin, M., Ibata, R., Ferguson, A., Lewis, G., & Tanvir, N. 2003, MNRAS, 343, 1335
Moore, B., Ghigna, S., Governato, F., Lake, G., Quinn, T., Stadel, J., & Tozzi, P. 1999, ApJ, 524, L19
Morrison, H. 1993, AJ, 106, 578
Morrison, H., Mateo, M., Olszewski, E., Harding, P., Dohm-Palmer, R., Freeman, K., Norris, J., & Morita, M. 2000, AJ, 119, 2254
Mouhcine, M., Ferguson, H., Rich, M., Brown, T., & Smith, T. 2005a, ApJ, 633, 821
Mouhcine, M., Rich, M., Ferguson, H., Brown, T., & Smith, T. 2005b, ApJ, 633, 828
Mould, J., & Kristian, J. 1986, ApJ, 305, 591
Navarro, J., Frenk, C., & White, S. 1997, ApJ, 490, 493
Peñarrubia, J., McConnachie, A., & Babul, A. 2006, ApJ, 650, L33
Pritchet, C., & van den Bergh, S. 1994, AJ, 107, 1730
Reitzel, D., & Guhathakurta, P. 2002, AJ, 124, 234
Reitzel, D., Guhathakurta, P., & Gould, A. 1998, AJ, 116, 707
Reitzel, D., Guhathakurta, P., & Rich, M. 2004, AJ, 127, 2133
Renda, A., Gibson, B., Mouhcine, M., Ibata, R., Kawata, D., Flynn, C., & Brook, C. 2005, MNRAS, 363, L16
Rich, M., Reitzel, D., Guhathakurta, P., Gebhardt, K., & Ho, L. 2004, AJ, 127, 2139
Robin, A., Reylé, C., Derrière, S., & Picaud, S. 2003, A&A, 409, 523
Rogstad, D., Wright, M., & Lockhard, I. 1976, ApJ, 204, 703
Ruphy, S., Robin, A., Epchtein, N., Copet, E., Bertin, E., Fouque, P., & Guglielmo, F. 1996, A&A, 313, L21
Ryan, S., & Norris, J. 1991, AJ, 101, 1865
Sarajedini, A., Barker, M., Geisler, D., Harding, P., & Schommer, R. 2006, AJ, 132, 1361
Schlegel, D., Finkbeiner, D., & Davis, M. 1998, ApJ, 500, 525
Ségall, M., Ibata, R., Irwin, M., Martin, N., & Chapman, S. 2007, MNRAS, 375, 831
Siegel, M., Majewski, S., Reid, I., & Thompson, I. 2002, ApJ, 578, 151
Springel, V., Frenk, C., & White, S. 2006, Nature, 440, 1137
Tiede, G., Sarajedini, A., & Barker, M. 2004, AJ, 128, 224
Toth, G., & Ostriker, J. 1992, ApJ, 389, 5
Vivas, K., & Zinn, R. 2006, AJ, 132, 714
Walterbos, R., & Braun, R. 1994, ApJ, 431, 156
Walterbos, R., & Kennicutt, R. 1988, A&A, 198, 61
Wetterer, C., & McGraw, J. 1996, AJ, 112, 1046
Yanny, B., et al. 2000, ApJ, 540, 825
Zibetti, S., & Ferguson, A. 2004, MNRAS, 352, L6
Zibetti, S., White, S., & Brinkman, J. 2004, MNRAS, 347, 556
Zucker, D. B., et al. 2004, ApJ, 612, L117